Fall 10-30-2017

TIME-OF-FLIGHT AND ENERGY LOSS ANALYSIS ON THE UNM FISSION FRAGMENT SPECTROMETER

Shelby Fellows
University of New Mexico

Follow this and additional works at: https://digitalrepository.unm.edu/ne_etds

Part of the Nuclear Engineering Commons

Shelby Fellows

_____
Candidate

Nuclear Engineering

_____
Department

This thesis is approved, and it is acceptable in quality and form for publication:

Approved by the Thesis Committee:

Dr. Adam Hecht, Chairperson

_____

Dr. Gary Cooper

_____

Dr. Cassiano R. E. de Oliveira

_____

_____

_____

_____

_____

_____

**TIME-OF-FLIGHT AND ENERGY LOSS ANALYSIS ON THE
UNM FISSION FRAGMENT SPECTROMETER**

by

SHELBY FELLOWS

**B.S., MECHANICAL ENGINEERING, NEW MEXICO
INSTITUTE OF MINING AND TECHNOLOGY, 2015**

THESIS

Submitted in Partial Fulfillment of the
Requirements for the Degree of

Master of Science in Nuclear Engineering

The University of New Mexico
Albuquerque, New Mexico

December 2017

Acknowledgments

First, I would like to thank my parents, their support and guidance has made it possible for me to continue my education. I would also like to thank my siblings, and friends for their continual support in all areas of my life. As well as my significant other Dom, I could not have made it through without his love and determination to help me succeed.

In addition, I would like to thank my graduate advisor Dr. Adam Hecht for the opportunity to work on this project and the guidance and insight given throughout my studies. I would also like to thank my committee members Dr. Gary Cooper and Dr. Cassiano R. E. De Oliveira, both who have taught me valuable information over my academic career.

Specifically, I would also like to thank my fellow students that have been researching and teaching much about this project; Phoenix Baldez, Rick Blakeley, and James Cole. I would also like to thank all members of the Los Alamos National Laboratory SPIDER group for all their help and support in my tenure of this project.

TIME-OF-FLIGHT AND ENERGY LOSS ANALYSIS ON THE UNM FISSION FRAGMENT SPECTROMETER

By

Shelby Fellows

B.S., Mechanical Engineering, New Mexico Institute of Mining

and Technology, 2015

M.S., Nuclear Engineering, University of New Mexico, 2017

Abstract

The University of New Mexico spectrometer experimental work has been used to provide an event-by-event fission product measurement to aid in filling in the gaps in existing fission product yield data. This thesis examines the time-of-flight (TOF) component of the spectrometer towards improving the resolution of the system, including examining system behavior using different positions on the TOF detectors, different thickness TOF conversion foils, and examining the energy loss of alpha particles and fission fragments through various foils and windows in the system. Using a mask in front of the second TOF detector to examine position dependence of the TOF detectors, we found that the far edges of the TOF detectors have lower efficiency than the center and the longer flight

path to the edges was somewhat represented in the TOF. Different thicknesses of TOF

conversion foils were examined with alpha particles and fission fragments: 20, 55, and

100 µg/cm^2 carbon foils. The foils give different energy loss and energy broadening,

with the thicker foils giving the most energy loss and broadening. This translates to

longer TOF timing and increased TOF broadening. For the thinnest carbon foil studied, a

timing resolution of 160 ps FWHM over 32 ns, or 0.5 %, was extracted for ^{239}Pu alphas.

Experimental results and simulations were compared for energy loss of ^{252}Cf fission

fragments. SRIM underestimated what the energy loss from carbon foils the thinner the

foils with an Experiment/SRIM energy loss ratio of 1.8 for heavy fragments and 1.4 for

light fragments for a 21 µg/cm^2 carbon foil; and overestimated energy loss from 200 nm

silicon nitride window with a ratio of 0.9 for heavy fragments and 0.8 for light fragments.

MCNP gives numbers that more closely match experiment values with an

Experiment/MCNP ratio of 1 for heavy fragments and 0.9 for light fragments for a 21

µg/cm^2 carbon foil; and ratio of 0.85 for heavy fragments and 0.97 for light fragments for

a 200 nm silicon nitride window. The full system resolution was analyzed and

calculations suggest a mass resolution using 20 µg/cm^2 conversion foils of 0.92% for

light fission fragments and 0.73% for heavy fission fragments. This work was performed

by the author at UNM as part of the Los Alamos National Lab Spectrometer for Ion

Detection in Fission Research project (SPIDER) collaboration.

Table of Contents

List of Figures

List of Tables

1 Introduction

1.1 Overview

In fission, a nucleus breaks apart, typically into two fragments which is also called binary fission. Fission is a form of nuclear transmutations because the fragments produced are not the same element as the original atom. Despite almost 80 years of fission research, most work has been on average energies released and there is still a great need for data on fission products.

In binary fission, two large fragments are emitted nearly back to back, and typically several neutrons are emitted. At lower energies, these large fragments are usually produced with a mass ratio of 3:2, with the distribution becoming more symmetric at higher energies. Since the discovery of fission in the 1940s, many experiments have been done to quantify the resulting fission fragments. For example, the Cosi Fan Tutte spectrometer was used to measure correlated mass, charge, and energy for well resolved light group masses from Thorium fission (Boucheneb and Geltenbort 1989) and Uranium 235 fission (Oed, Geltenbort and Brissot, et al. 1984).

In pursuit of this fission fragment mass distribution data, our group at UNM has built and fielded a fission fragment spectrometer as part of the Los Alamos National Laboratory Spectrometer for Ion Detection in Fission Research project (SPIDER) collaboration. The UNM spectrometer is an event-by-event detector that uses a time-of-flight system and an energy detector to measure the correlated velocities and kinetic energy of fission fragments to

find fragment masses. Work has been performed on spontaneous fission of ^{252}Cf as well as neutron induced fission of ^{235}U and ^{239}Pu. The UNM design is based on previous v-E spectrometers (Boucheneb and Geltenbort 1989). In this scheme, particle velocity is determined by the time-of-flight (TOF) measurement and the particle kinetic energy is determined by a detector that follows. From Kinetic Energy (KE)=$^1/_2$ mv^2 and with both KE and v determined, the fragment masses may be extracted.

In this work, we characterize the time-of-flight system towards improving resolution, including TOF detector resolution, position effects, timing change, straggling from different TOF conversion foil thicknesses, and we explore the effect of the energy loss on the time-of-flight section of the fission fragment spectrometer.

1.2 Background and Prior Work

Many different groups and methods have been implemented to characterize the mass spectra of ^{252}Cf and ^{235}U. Oak Ridge National Laboratory (Schmitt, Kiker and Williams 1965) used a silicon surface barrier detector time-of-flight technique to correlate energies and velocities of ^{252}Cf and ^{235}U fission to obtain mass and energy distributions as shown in Figure 1 and Figure 2, respectively. This work also provides a "universal" energy calibration procedure for solid state detectors for fission fragments, based on the mass and pulse-height versus energy relation. The average energies of the light and heavy fragments found by Schmitt et al. (Figure 2) will be compared with those found in the current work, as Schmitt et al. results are accepted as the standard published values.
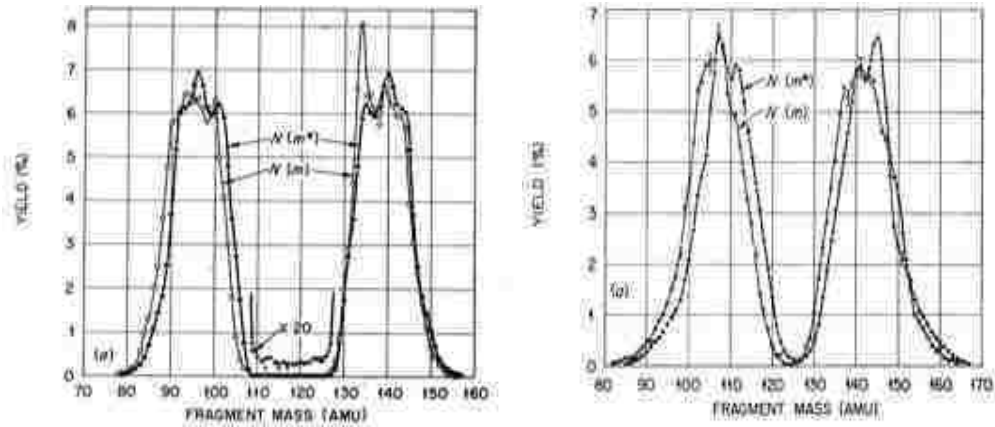
Figure 1: Mass Spectrum of ²³⁵U (left) and ²⁵²Cf (right) (Schmitt, Kiker and Williams 1965).
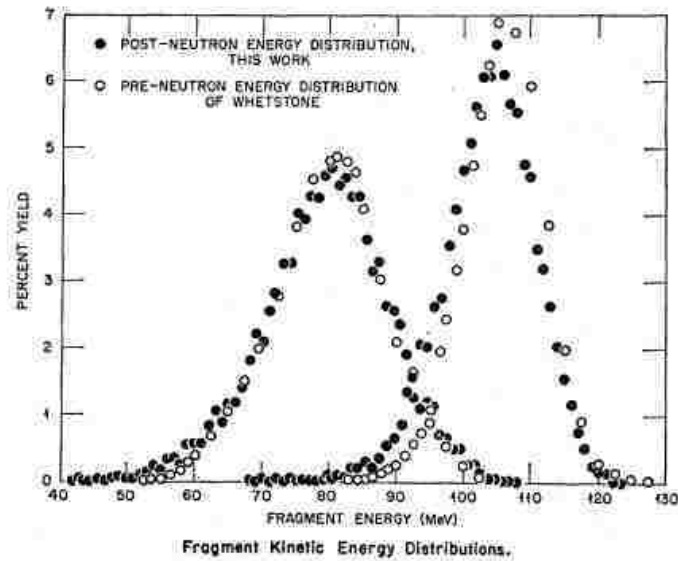
Figure 2: Energy distribution of Post –neutron-emission kinetic energy distributions for the light and heavy fragments of ²⁵²Cf (Schmitt, Kiker and Williams 1965).

In the paper by Schmitt et al. a method for calibrating the energy response of a silicon semiconductor detector for measuring fission fragments is also described. Many experimenters have used these methods first described by Schmitt et al. to measure the slowing down of fission fragments in different absorbers, this methodology is discussed in more detail in chapter 6.2.

The UNM fission fragment spectrometer has been used to take measurements of low energy neutron induced fission of ^{235}U in December of 2014 and 2016 as well as spontaneous fission ^{252}Cf. The goals of these experiments are to gather an independent data set for correlated Z determination work we have done with these masses, and to compare our results with prior published work. In this thesis only characterization of ^{252}Cf fission products, and alpha particles from several sources, will be evaluated.

In chapter 2, the theory of fission and the principles of the fission fragment spectrometer experiment will be presented. The electronics and experimental set-up will also be discussed. Chapter 3 will discuss the calibration method used for timing. Chapter 4 will describe the method developed to measure the change in the measured timing as a function of the incident location of the ions on the carbon timing foils. Chapter 5 describes the set-up and results for the use of different thickness of carbon conversion foils. Chapter 0 discusses the energy loss theory and mass dependent pulse height defect. Chapter 7 describes the method, background, and the results for both the alpha and fission fragment energy loss experiment. In chapter 8 the uncertainty of the plutonium source is analyzed, and what effect this brings to the full system uncertainty. Finally, chapter 9 presents conclusion and future work.

2 Background on Theory and Experimental Approach

2.1 General Background on Fission

Nuclear fission is when a nucleus splits into two smaller fragments. This may be induced by neutrons or may be spontaneous. For neutron induced fission, when some nuclei are fused with low energy neutrons they may have enough excitation energy to be above the fission barrier, which can lead to a large fission branch. At low parent nucleus excitation energies, the fission fragments are typically asymmetric in mass, leading to two mass peaks in the subsequent statistical distribution of fragments. Figure 3 shows the results of a thermal fission of ^{235}U. The number of protons and neutrons remains constant, and the total mass number, A, of the fragments is equal to the mass number of the fission parent, though some mass is lost to kinetic energy. Quickly after fission neutrons may be emitted from the fragments, reducing their mass and complicating subsequent measurements.
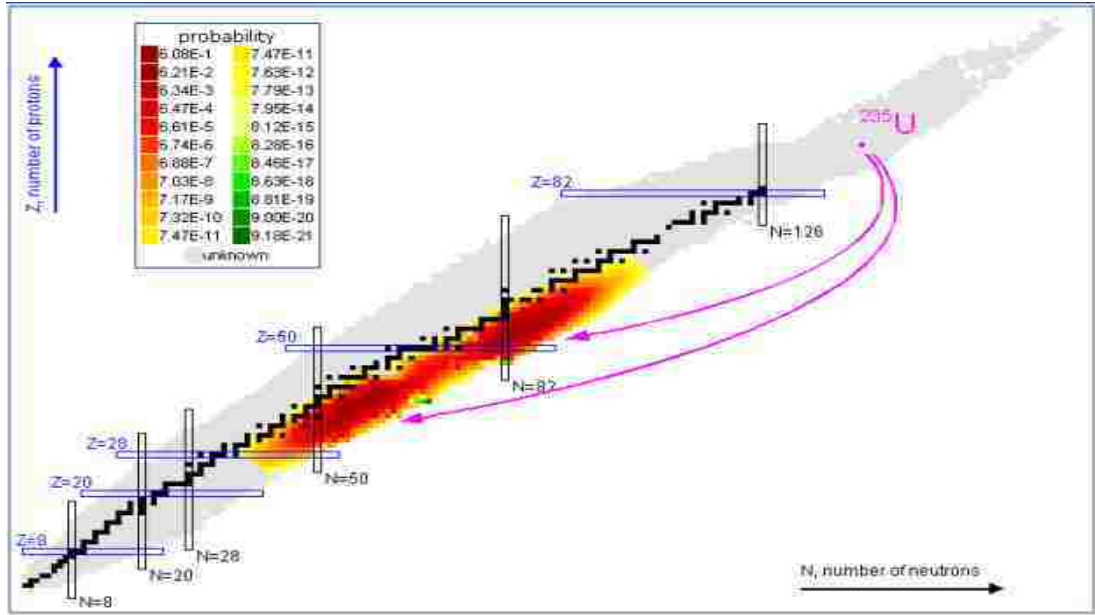
Figure 3: Asymmetric fission of ^{235}U (Magee 2011).

2.2 The v-E Method and the UNM Spectrometer

There are multiple experimental set-ups used to calculate mass information of fission events, and many approaches require information on timing and energy. The v-E method, based on velocity and kinetic energy, can be used to measure fission products on an event-by-event basis with timing and energy. A time-of-flight (TOF) detector determines the velocity of the particle, v, and another detector measures the energy, E. This information is used to determine the mass of the particle of interest (Boucheneb, Geltenbort, & al., 1989) following the classical equation $E = \frac{1}{2}mv^2$. Figure 4 shows a rough schematic of the experimental set-up of the UNM spectrometer, which uses an ionization chamber for the energy detector and two MCP based timing modules for the TOF detector. Both the TOF and energy detectors, as built for the UNM fission fragment spectrometer, will be discussed.

Figure 4: 1v-1E detector used in UNM spectrometer.

2.2.1   Time-of-flight

The time-of-flight detector measures the time-of-flight of particles between two foils at a set distance using signals from the two-timing modules. Each timing module consists of a thin carbon conversion foil, an electrostatic mirror, and a microchannel plate (MCP) detector. As an incident charged particle passes through the thin carbon foil, energy is lost to electron interactions and electrons are ejected. With the use of an electrostatic mirror the electrons are reflected to the Micro Channel Plate (MCP), as shown in Figure 5. The mirrors are thin wires under bias and present only a small cross-sectional area, and the incident particles with much higher mass-to-charge ratios than electrons can pass through with high efficiency. The MCP is off to the side to not impede the travel of the incident particle and detects the ejected and reflected electrons. The MCP then amplifies the electron signal incident on it into an easily observable pulse while retaining the timing of the initial signal to within 100 ps. The MCP is described more fully in chapter 2.2.1.1.
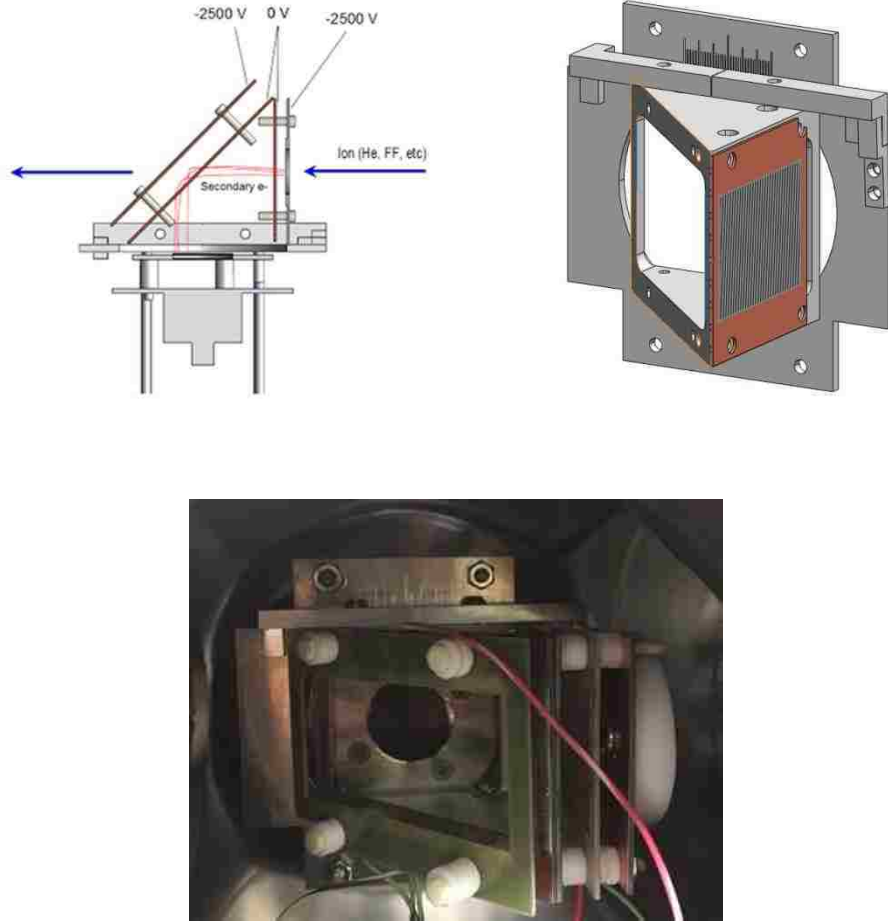
Figure 5: TOF timing module SolidWorks models (Top) and a photo (Bottom).

Coupling the known distance between the timing module foils, ΔL, with the flight time Δt, as measured with the two-timing modules, the velocity, v, of the particle is readily determined from the relationship: $v = \frac{\Delta L}{\Delta t}$.

A diagram of the full UNM Spectrometer is shown in Figure 6. A is the target location for the experimental runs at LANL, where a neutron beam is used. B(start) and C(stop) are the two-timing modules. D is the silicon nitride (SiN) entrance window to E, the ionization chamber.
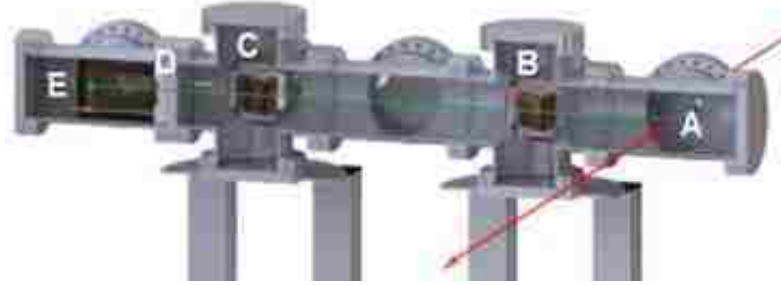
Figure 6: UNM Spectrometer labeled as: A-Source position, B-Timing start module, C-Timing stop module, D-IC entrance window, and E-Ionization chamber.

Figure 7 shows an expanded view of the time-of-flight section of the spectrometer. In Figure 7, a radioactive source, A, is shown mounted next to the first timing module, which is the configuration used in experiments at UNM.
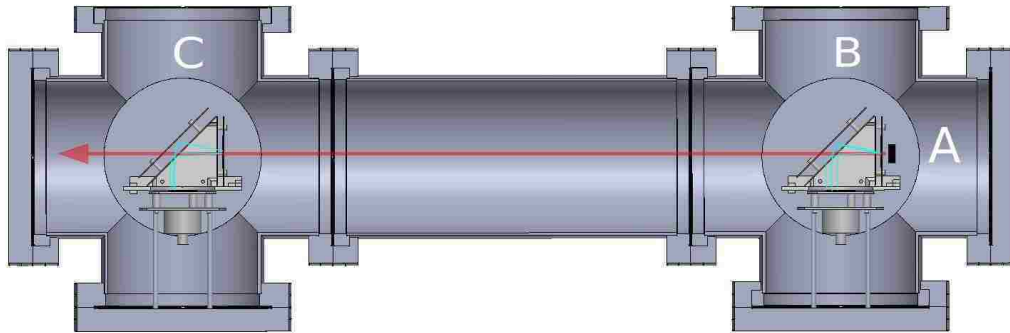
Figure 7: Time-of-flight section of UNM spectrometer with source A mounted on timing module B.

The carbon foils used in this thesis had an areal density of 20 to 100 µg/cm^2, which minimized the interactions of the passing particles and, hence, minimized their energy loss and the broadening of the subsequent energy distribution. The electrostatic mirrors and carbon foils are made up of FR4 plastic frames with gold plated tungsten wire as grid and line patterns shown in Figure 5 (Cole 2016).

9

2.2.1.1 Microchannel Plate Detectors (MCP)

Microchannel Plate Detectors MCPs are used in the timing modules to read out small

current events such as the electrons that are ejected from the carbon foils by the fission

fragments. A microchannel plate detector uses thin plates with many microscopic pores,

with the plates under bias relative to one another and to external electrodes, and the

system behaves similar to a photomultiplier tube. The electrons are accelerated towards

the plate and when they strike the pores, secondary electrons are emitted. Within the

pores several collisions may occur, releasing several generations of secondary electrons

and greatly increasing the signal while preserving the sharp timing of the pulse.

The specific MCP used in the experiment set-up is the F9890-11 made by Hamamatsu,

which has an effective diameter of 27 mm and a two-stage chevron channel design

(Heffern 2015).

 Figure 8 shows the chevron configuration of the MCPs used. The channels are typically

biased at an angle of 5°-15° from the normal of the plate face to limit ion feedback as

well as increasing sensitivity to the incident radiation normal to the MCP surface

(Hamamatsu 2001).
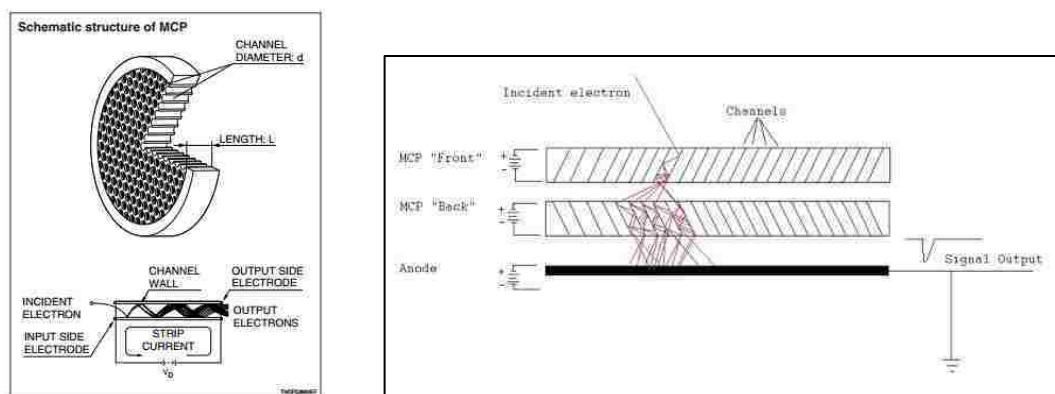
Figure 8: MCP channel structure (left) and Chevron configuration of two MCPs placed in series (Wiza 1979) (right).

2.2.1.2   Previous TOF Resolution Measurements

Previous time-of-flight tests were performed with these MCP's with a TOF distance of 1 meter between the timing modules. Figure 9 shows the result of the timing test using foils with a thickness of 80-100 μg/cm^2. The time difference between the MCP signals was extracted for a ^{239}Pu alpha source and a histogram developed. The full width at half max (FWHM) was found to be 371.8 ps for the entire pulse width. Analysis making note of individual alpha branches, as detailed in chapter 5, gives a FWHM of 329 ps for each alpha particle energy. The fractional timing resolution using the FWHM, $\delta t/t$ was found to be 0.59%. The system has since been modified to reduce the TOF length from 1 m to 50 cm to increase geometric efficiency, though this influences the fractional resolution as will be seen. The source broadening contributions to resolution will also be discussed. That broadening indicates the TOF detector resolution is much better.
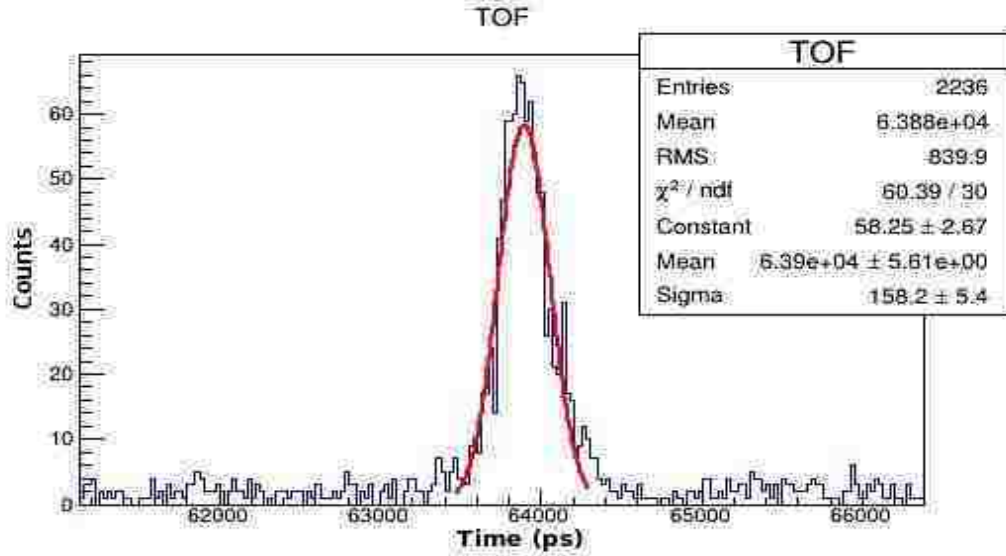
Figure 9: ²³⁹Pu alpha particle TOF Results for a 1 m flight path and 80-100 μg/cm² thick carbon foil (R. Blakeley 2017).

2.2.2 Time-of-flight Electronics

The physical layout of the TOF system has been discussed, but the electronics and signal processing must also be mentioned. The voltage was supplied to the MCP by an ORTEC 456 power supply. A simple circuit divided this applied voltage to provide the correct bias to each MCP stage. Each MCP signal was collected through an ORTEC VT120 fast preamp and then sent through the Model 715 discriminator. The output signals of the discriminator are square pulses that are sent to the time-to-pulse-height converter (TPHC) which converts the time difference between the start and stop signals (the first and second MCP signals) to a square pulse with the height proportional to the time difference. The TPHC output is then sent to the CAEN digitizer which determines the pulse height, and this information is sent to the computer. The raw data file is then analyzed in MATLAB. A diagram of the electronics is shown in Figure 10.

12
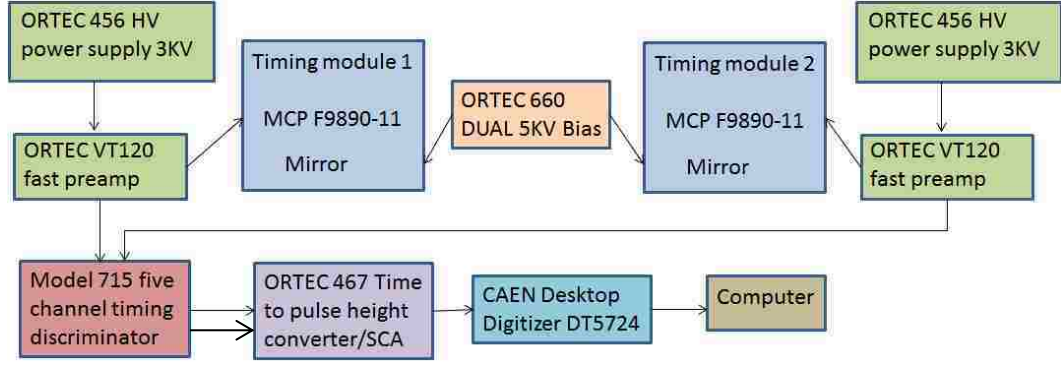
2.2.3 Ionization Chamber and Ionization Chamber Entrance Window

For a v-E measurement, both the velocity and kinetic energy of each particle must be correlated. The TOF system is used to extract the velocity. The kinetic energy of the particle in the fission fragment spectrometer is read out by an ionization chamber (IC). The ionization chamber is a cylinder which consists of a cathode on one end, a series of guard rings, a Frisch grid, and an anode on the other end. A cross section of the IC is shown in Figure 11. The guard rings act to keep the electric field lines parallel in the active region of the detector. This is in a chamber filled with an inert gas, in our case isobutane. As a particle travels into and stops in the ionization chamber it will interact with gas particles, ionizing them along the way as it slows down and stops. As the gas is ionized between the anode and cathode, the electric field acts on the free electrons in the gas and the resulting free electrons drift towards the anode and the ions drift towards the Frisch grid and the cathode. The moving electrons induce a pulse on the cathode as soon as they begin moving, and induce a pulse on the anode as soon as they pass the Frisch grid. The size of the pulse on the anode is proportional (with corrections) to the kinetic

13

energy. The timing difference between the cathode and anode pulses gives the position

along the length of the chamber that the particle stopped, which gives charge information

through the stopping power of the particle.
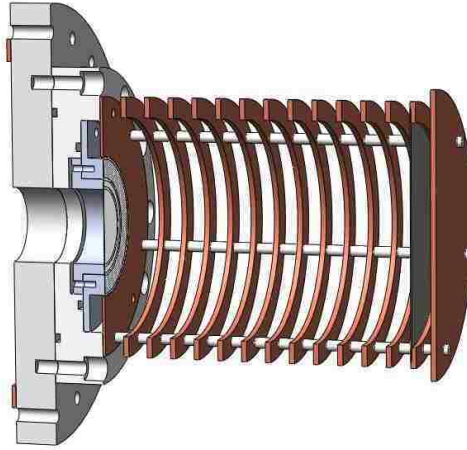
Figure 11: Ionization chamber design.

The ionization chamber is filled with 70 torr of isobutane the typical voltages used on the

cathode and anode are 2400 V and 500 V respectively. The window that separates the

time-of-flight vacuum and ionization chamber gas must be able to withstand a differential

pressure of high vacuum on one side and 1/3 atmosphere on the other. The window must

also be thin to reduce the energy loss of the particles as they pass through since more

energy loss translates to a larger broadening in the resulting energy distribution. In the

past Mylar has been used for this project, which appeared to seep gas for thicknesses

lower than 2.5 microns, then a single 1 cm by 1 cm 200 nm thick window of silicon

nitride which is much less porous to isobutane. Shown in Figure 12, a seven-window

design, each 200 nm, is now in place to increase the efficiency. The windows are glued to

the aluminum frame by NuSil Silicone adhesive which we had tested to withstand the differential of 130 torr (Reltek 2014).
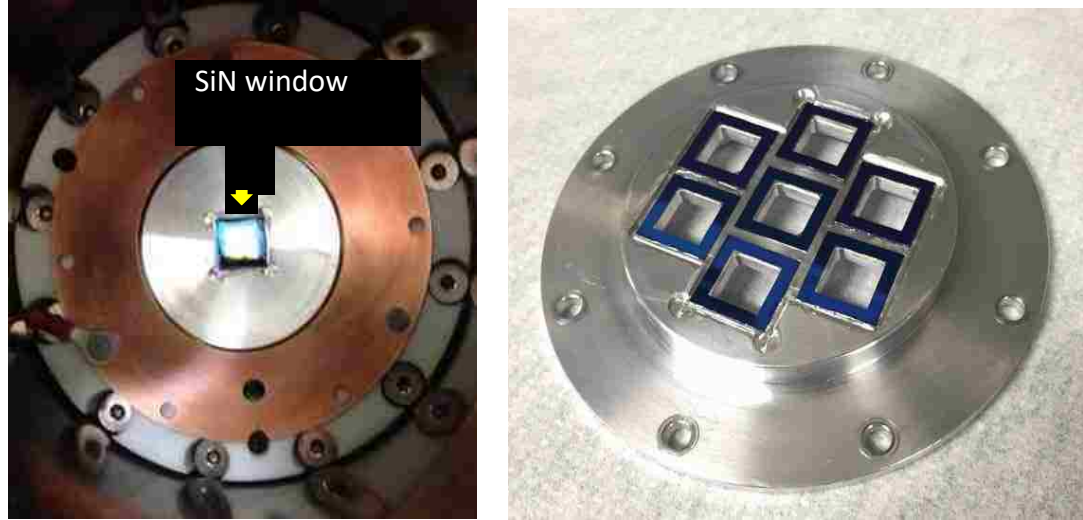
Figure 12: Previous single SiN window (Cole 2016) (left) Current 7 window design (right).

2.3   Uncertainty Accounting

The goal of characterization of the system is, of course to improve the system, which in this case means improving the mass resolution while maintaining reasonable efficiency. With measurements of time (t), length (L), and energy (E); the mass (m) of the particle can be determined by rearranging the classical kinetic energy expression $E = \frac{1}{2}mv^2$ to $m = 2E \left(\frac{\Delta t}{\Delta L}\right)^2$ The uncertainty is calculated as

Equation 1

$$\frac{\partial m}{m} = \sqrt{\left(\frac{\partial E}{E}\right)^2 + \left(\frac{2\partial L}{L}\right)^2 + \left(\frac{2\partial t}{t}\right)^2}$$

15

We will return to this equation as we assess different sources of time and energy

broadening. To resolve the different mass peaks, the uncertainties indicated, such as ∂m,

must be FWHM. Previous best mass resolution resolving powers using the v-E method

from other groups are ~1 amu for light products and ~2-3 amu for heavy products (Oed,

Geltenbort and Brissot, et al. 1984), again indicating FWHM.

2.4   Energy Loss Corrections

The kinetic energy expression used to extract mass requires the velocity to relate directly

to the particle's energy. Complicating things, the energy that is collected by the ionization

chamber is different from the energy of the particle in the time-of-flight region, as the

particle must pass through the second TOF detector foil and the entrance window to the

ionization chamber before the energy may be measured in the ionization chamber. In

addition, the particle entering the TOF region loses energy in the first foil as well and so

the energy in the TOF region is not the same as the energy from the particle source. To

find the mass from the energy and TOF both should be measured in the same region. As

this is impossible, the energy measured in the ionization chamber must be corrected to

the TOF region, the energy loss in the carbon foil on the second timing module and in the

SiN window is considered. Figure 13 depicts the different kinetic energies.
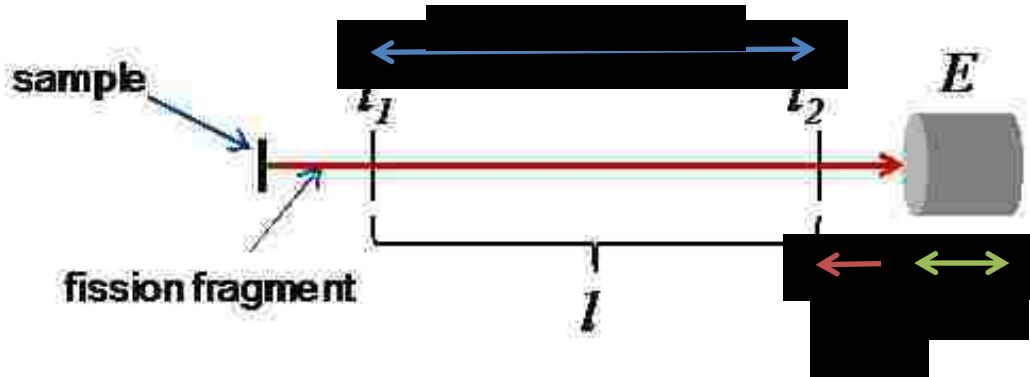
Figure 13: Kinetic energy divisions (Cole 2016).

In this figure, KE_{IC} is the energy deposited in the ionization chamber, KE_{Add} is the energy that is lost to the 2nd carbon foil and the SiN window that must be added back to obtain KE_m, the kinetic energy we wish to obtain to make mass calculations. Using the Stopping and Range of Ions in Matter (SRIM) (Ziegler 1999) code and the method described in OED, (Oed, Geltenbort and Brissot, et al. 1984), the KE_m can be estimated.

Table 1 gives an example of the values used and the amount of energy loss calculated with SRIM for ^{252}Cf isotopes passing through a carbon foil and 200 nm SiN. While energy loss calculations with SRIM are assumed to be accurate for alpha particles, this is thought to be poor for fission fragments. This loss should be measured explicitly, which is the motivation for chapter 7 of this thesis.

Table 1: Energy add-back values (R. Blakeley 2017).

Element	Z	A	KE Initial [keV]	Ef1[keV]	TOF average	Ef2 [keV]	Eloss [keV]
Cr	24	66	131066.94	127737.80	2.589E-08	123082.80	4655.00
Co	27	70	128058.87	124114.07	2.70494E-08	118588.13	5525.94
Ga	31	79	121290.73	116830.44	2.9618E-08	110571.31	6259.13
Br	35	88	114522.58	109558.94	3.22803E-08	102603.68	6955.26
Y	39	99	106250.40	101138.07	3.56352E-08	93966.06	7172.01
Zr	40	101	104746.37	99850.92	3.62246E-08	92994.00	6856.92
Nb	41	103	103242.34	98125.57	3.69018E-08	90917.24	7208.33
Mo	42	106	100986.29	95640.66	3.79185E-08	88136.33	7504.33
Tc	43	107	100234.27	94835.68	3.82583E-08	87256.18	7579.49
Ru	44	110	97978.23	92598.94	3.92566E-08	85048.51	7550.43
Rh	45	111	97226.21	91807.04	3.96044E-08	84192.27	7614.77
Pd	46	113	95722.18	90286.90	4.02946E-08	82667.00	7619.90
Ag	47	114	94970.16	89102.23	4.07406E-08	80860.72	8241.51
Cd	48	118	91962.10	86595.69	4.20448E-08	79073.43	7522.26
In	49	119	91210.08	85850.74	4.24054E-08	78325.19	7525.56
Sn	50	130	82937.90	77919.91	4.65229E-08	70850.82	7069.09
Sb	51	133	80681.85	75722.47	4.77346E-08	68738.80	6983.67
Te	52	134	79929.84	74990.80	4.81469E-08	68002.44	6988.37
I	53	135	79177.82	73753.98	4.87297E-08	66144.57	7609.41
Xe	54	138	76921.77	72354.23	4.97424E-08	64135.86	8218.37
Cs	55	141	74665.73	71406.88	5.06126E-08	65466.24	5940.64
Ba	56	143	73161.69	70537.91	5.12833E-08	63763.21	6774.71
La	57	145	71657.66	69687.78	5.19547E-08	62934.05	6753.73
Ce	58	148	69401.61	68722.71	5.28567E-08	62038.46	6684.26
Pr	59	150	67897.58	63331.32	5.54314E-08	56851.78	6479.54
Eu	63	160	60377.42	55570.14	6.11165E-08	48849.83	6720.31
Dy	66	166	55865.32	51121.57	6.4904E-08	44548.02	6573.55
Tm	69	172	51353.23	51180.82	6.60283E-08	44694.03	6486.80
avg light	42	106	103770.00	98384.73	3.7386E-08	90818.12	7566.61
avg hvy	52	141	79370.00	74533.22	4.95398E-08	67689.99	6843.24
alpha239	2	4	5156.00	5077.41	3.1969E-08	4964.78	112.63
alpha252	2	4	6118	6047.59	2.92926E-08	5948.01	99.58

2.5   Post Processing

2.5.1   Fission Product Yield Calibration

The raw data of the TOF, converted to a pulse height in the TPHC, and the ionization chamber energy pulse height are acquired by a CAEN digitizer and the pulses recorded as channel numbers, with time stamps that are later used to correlate TOF and IC signals. The timing between the cathode and anode are also recorded in a Time to Analog convertor, which is not addressed in detail in this work. To calibrate the channels in the IC data stream to their appropriate energy a simple two-point linear calibration is used. The pulse height is proportional to the energy deposited by the incident radiation. Most of the yield is made up of the heavy and light fission fragment peaks as seen in the Figure 14. The light peak is made up of elements from Y to Ag and the heavy peak is made up of elements from Sn to Pr. The average mass and energy value is used as calibration points, in the Table 2.

Table 2: Average light and heavy values for ^{252}Cf calibration values (Schmitt, Kiker and Williams 1965).

Calibration Values for ^{252}Cf		
Variable	Value	σ
E_l *[MeV]*	103.77	5.48
E_h *[MeV]*	79.37	8.23
m_l *[amu]*	106	6.53
m_h *[amu]*	141.9	6.53

Figure 14 is a fission product yield of ^{252}Cf; UNM results, shown in blue were taken with 1.5 micron thick Mylar IC entrance window. The peak location was surprisingly accurate considering the lack of absolute calibration; however, the valley and tails of the peaks suffer heavily from statistical error (R. Blakeley 2017).
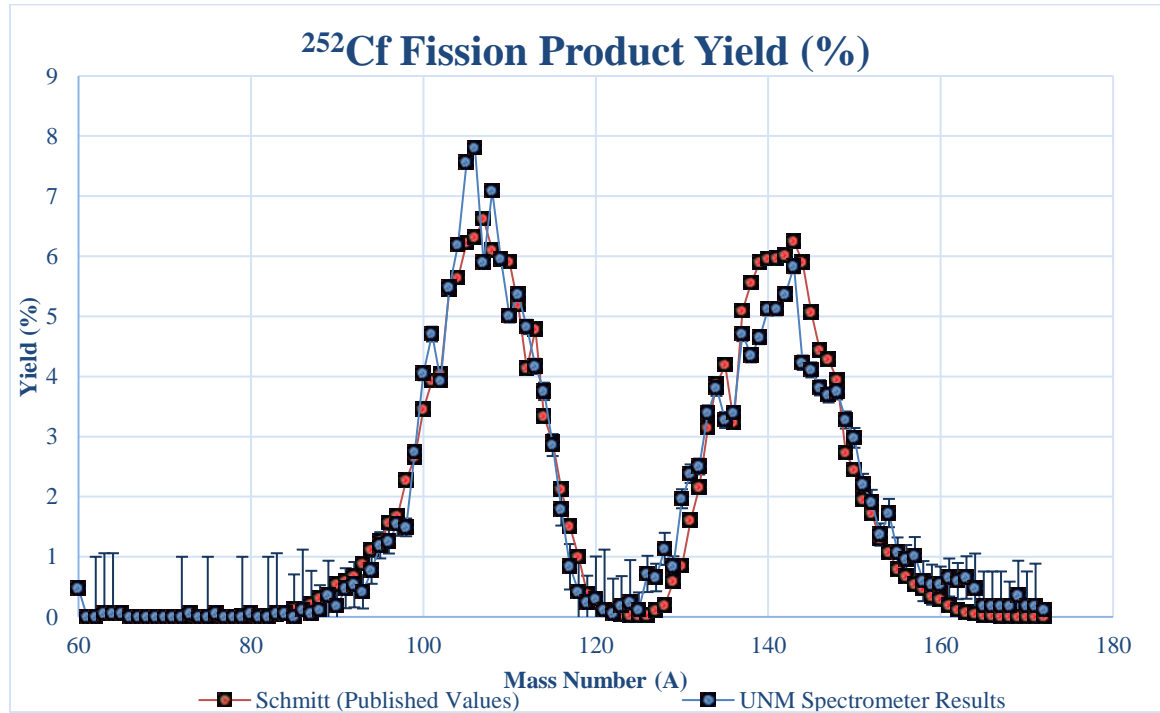
Figure 14: Isotope fission product yield for ^{252}Cf (R. Blakeley 2017).

In the following chapters, we work to characterize and optimize the time-of-flight detector to help reduce some of the broadening and statistical errors. This is done with a characterization of geometrical and foil thickness effects.

3 Time-of-Flight Calibration

Previously the distance between the two-timing modules, measured with a ruler, was used to calibrate the data from channel to TOF using known alpha particle energies. This brings in uncertainties from the distance between the detectors to the broadening of the source itself. Since we are interested in understanding how sharp the response was from different parts of the system and manipulating conditions to understand changes, calibrating the time with cable delays was an appropriate starting point.

3.1 Timing Calibration

To calibrate the timing data, specific lengths of cable were used to delay signals since we have no instrumentation modules with a delay on the order of nanoseconds. Initially the output signal from a 419 Precision Pulse Generator was split with LEMO cables with different time delays between the split signals. Those signals were fed to a constant fraction discriminator (CFD) and the outputs fed to the start and stop inputs of the time to pulse height converter (TPHC). The time delay was verified on an oscilloscope before each run, shown in Figure 15. In Figure 16 the 25, 50, and 75 ns delays are plotted; the 25 and 50 ns pulses are 6 channels wide and the 75 ns delay is wider due to the broadening from a longer delay signal.
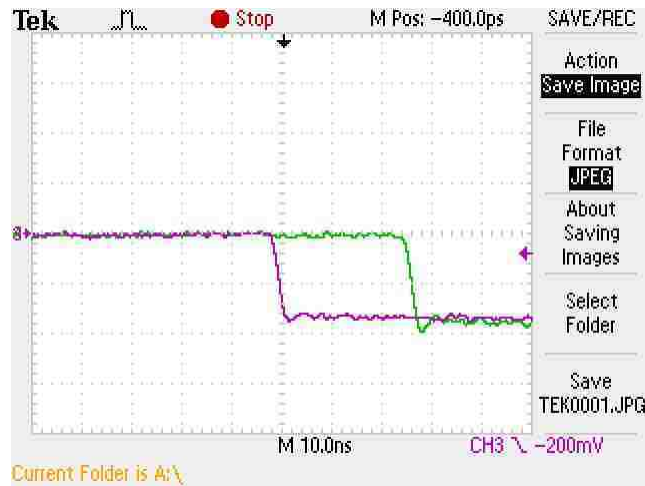
Figure 15: Oscilloscope trace of a 25 ns cable delay.
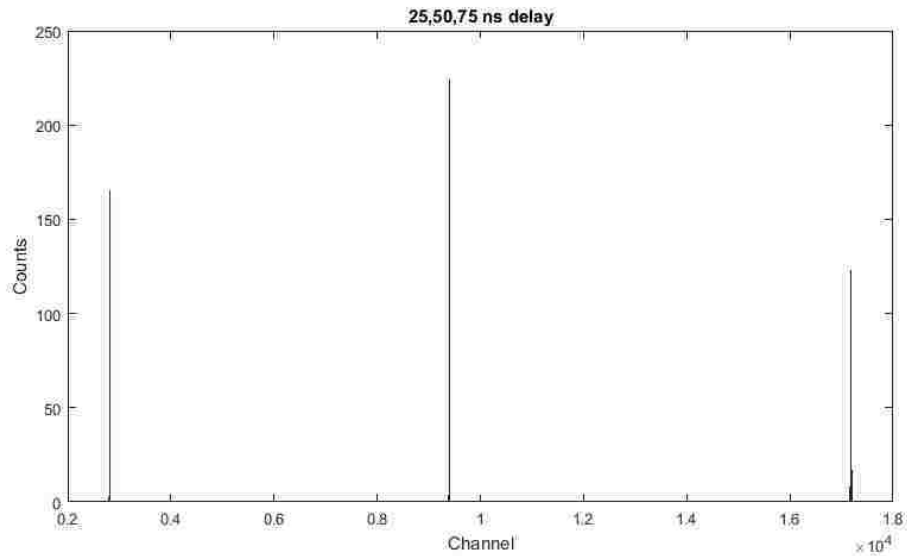
Figure 16: 25, 50, 75 ns cable delays taken on May 15 in terms of channel number, the larger channels correspond to longer delays.

It was discovered after sufficient data was collected that this calibration method was not

ideal. Some LEMO cables had small tears near the connectors and when wiggled would

produce a longer or shorter delay. The pulser that was used also caused the delays to

change over time. The pulser was initially used so that calibrations could be made while

the spectrometer itself was not on, and all calibrations could be done the same way, and the different shape of the pulser signals on different length cables caused different triggering in the discriminators. The method that worked best was feeding the pulser directly into the discriminator, splitting the output of the discriminator, and sending those signals to the TPHC. Even better was using the output of a single MCP instead of the pulser into the discriminator and splitting that signal through different delay cables. In Figure 17 the sharp MCP raw signal is shown in orange and the square logic signal from the CFD is the blue signal.

Figure 17: Oscilloscope trace of MCP signal before (orange) and after going through the discriminator (blue).

3.2   Set-up

Time-of-flight measurements started on April 26, 2017. From that time to Jun 21, 2017 the first calibration method was used, with an unfortunate drift. The 419 Precision pulse generator (pulser) signal was split and the start and stop signals were fed to the discriminator, where the discriminator outputs were then fed to the TPHC. This method

23

of calibration was used for the different thickness foil measurements and the first three

position sensitive measurements. This method was used so that calibration measurements

could be made while the spectrometer was not running.

After June 21st, it was apparent that the calibration had been drifting, seen in the

overnight calibration run results in Figure 21. The next method, splitting the signal after

the discriminator displayed in the block diagram in Figure 19, the overnight run results

are shown in Figure 22.
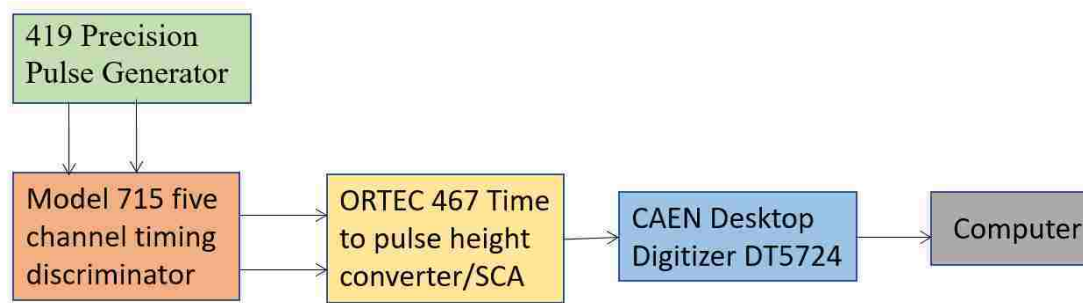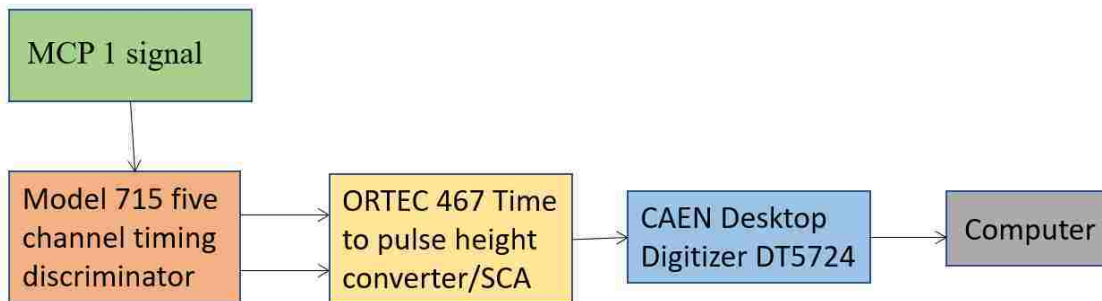
Figure 19: Block diagram of calibration with signal split after discriminator.

TOF measurements were made during both periods and so measurements after June 21 have a better timing calibration.

3.3 TOF Calibration Results

3.3.1 CAEN HIST vs. ASCII Files

The CAEN software brought more initial issues, the channel number seemed to drift and have an odd multiplication factor from the GUI histogram to the output ASCII file. This difference is shown in Figure 20. This was partially resolved when the software was updated on May 29, there is still a discrepancy between the displayed histogram to the ASCII file but that difference is constant with the software update. Values from the ASCII file are exclusively used and not from the displayed histogram.

6/19 25, 35, 50 ns Delay

$y = 4.999E\text{-}12x + 1.393E\text{-}08$

$y = 4.567E\text{-}12x + 1.395E\text{-}08$

- ■ HIST
- ◆ ASC
- —— Linear (HIST)
- —— Linear (ASC)

Time(s) — Channel number
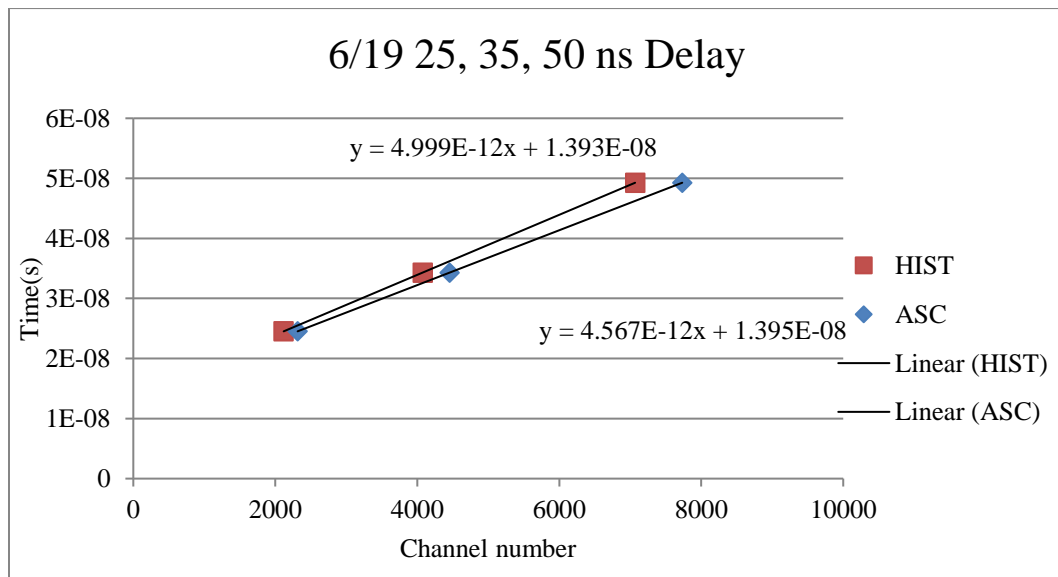
Figure 20: Histogram channel values (blue diamond) and ASCII channel number output (red square).

3.3.2   Overnight Timing Runs

Using the split signal from the pulser, BNC cables totaling a length of 33 ns were run for 15 hours starting at 6pm on 6/22. These values are shown with the standard deviation to show how inconsistent the channel number was behaving using hourly averages, the FWHM of the distribution of the hourly averages 8 channels, graphed in Figure 21.
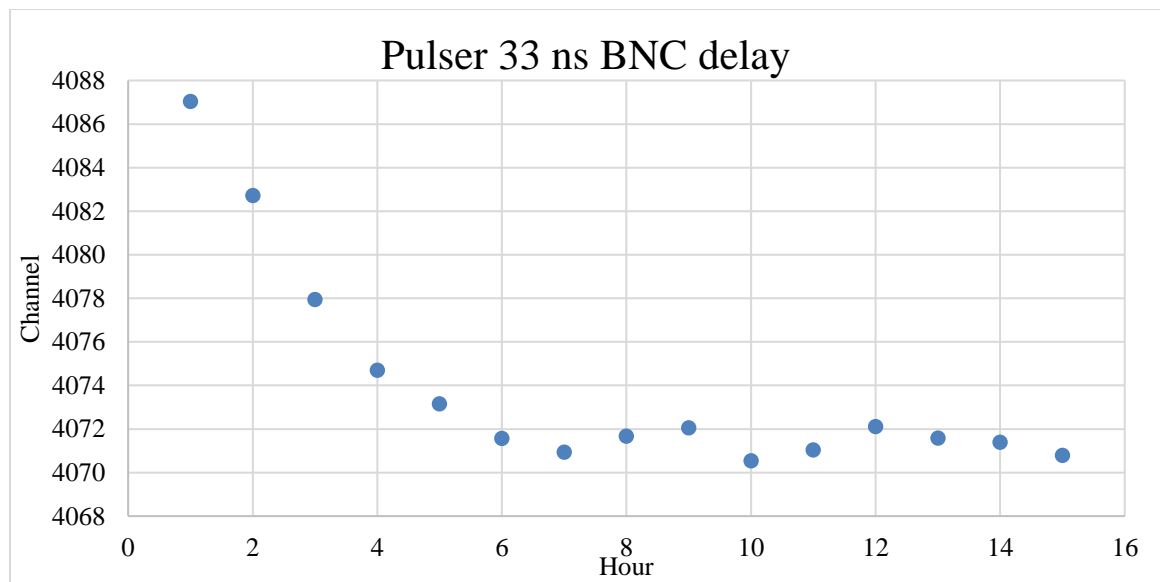
Figure 21: 33 ns cable delay, 15 hour run split from the pulser, hourly averages.

In Figure 22 the MCP was left on and running the signal was split from the output of the discriminator, giving a 31.84 ns delay. These values are much more uniform with a FWHM of 0.46 channels or 3.8 ps.
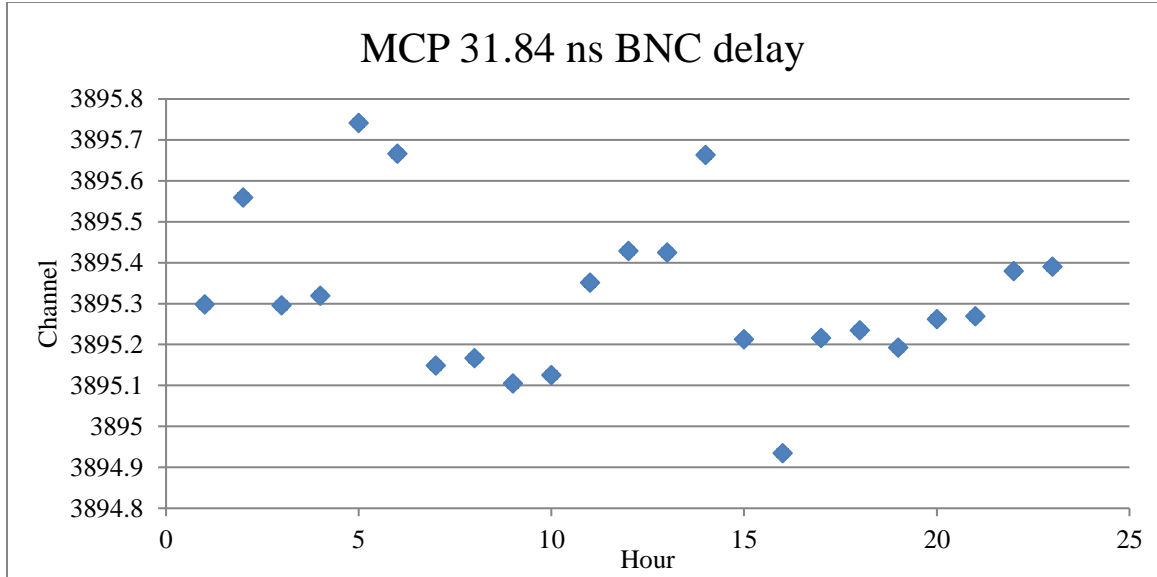
Figure 22: 31.8 ns cable delay ,24 hour run split from the MCP output of the discriminator.

3.3.3 Thickness Calibration

After the runs with different thicknesses of foils in place, a calibration run was performed

with 25, 50, and 75 ns delays as described earlier. All these runs were performed before

updating the CAEN software on May 29th. The three-point calibrations using cable

delays drift between the days, making interpretation of the true TOF data measurements

using the different carbon foil thicknesses difficult. The different TOF measurements

with different carbon foil thicknesses relied on the channel-to-energy equations extracted

from the cable delay calibrations, where the channel was extracted from measurement

and the time taken from the known cable delay. The y intercept shown in the Figure 23

was taken as the average of these three calibrations, 16.8 ns. The results using these

calibrations for the carbon foil thickness runs are summarized in chapter 5.

27

Different thickness foil calibration

$y = 3.39\text{E-}12x + 1.71\text{E-}08$ ■ 15-May

$y = 3.33\text{E-}12x + 1.58\text{E-}08$ ▲ 23-May

$y = 5.04\text{E-}12x + 1.77\text{E-}08$ ● 26-Apr
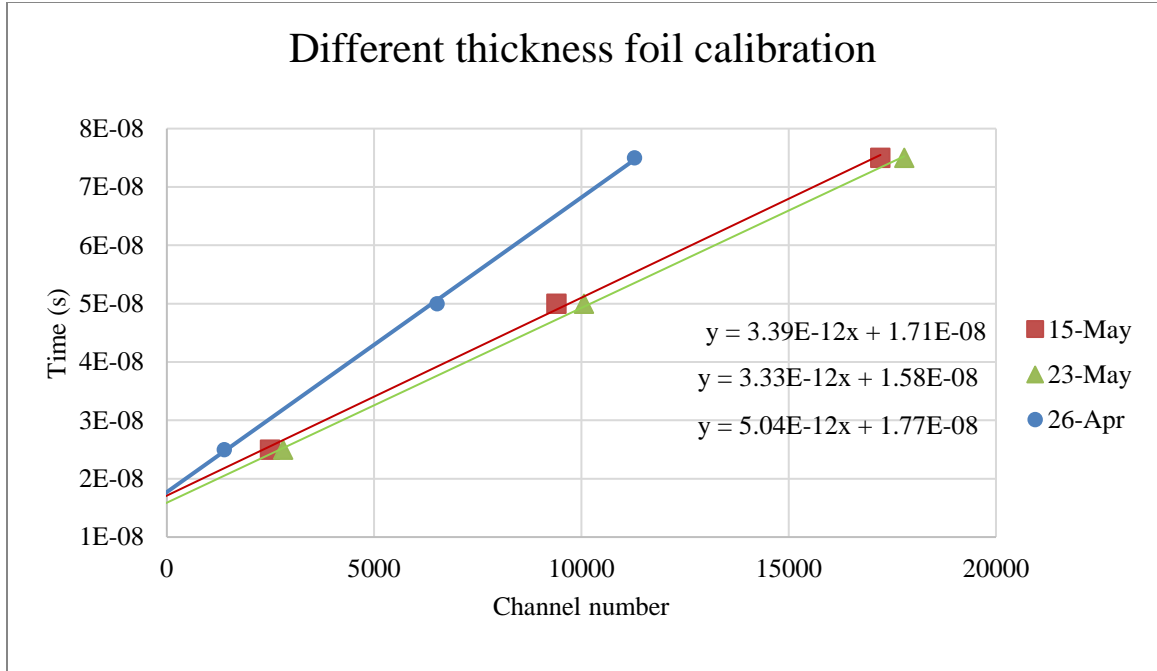
Figure 23: Calibration for different thickness of foil measurements (using 25, 50, and 75 ns delay) with the equation for each line.

3.3.4   Position calibration

Starting June 12 and ending June 29, runs were done using blockers with different hole positions in front of the second TOF detector foil, called blockers, for position measurements described in chapter 4. After each run a series of calibrations were taken. The first three were taken with the pulser and the lemo cables, like the previous calibrations. After June 21 and the overnight run that were taken it was apparent that this calibration method was not ideal. From June 21 and on all calibrations, were taken with the output of the MCP 1 signal, split and fed to the TPHC, using BNC cables. All calibrations used in analyzing the data are displayed in Figure 24 and the equation for each line in Table 3 labeled by the date taken. You will notice that these do not use the same time delay, June 12 to June 19 used 25, 35, and 50 ns delays with LEMO cables.

June 21 and on used 14, 26, 32, 40, 50 ns delays with BNC cables where the oscilloscope

traces were used to confirm the correct time delay.
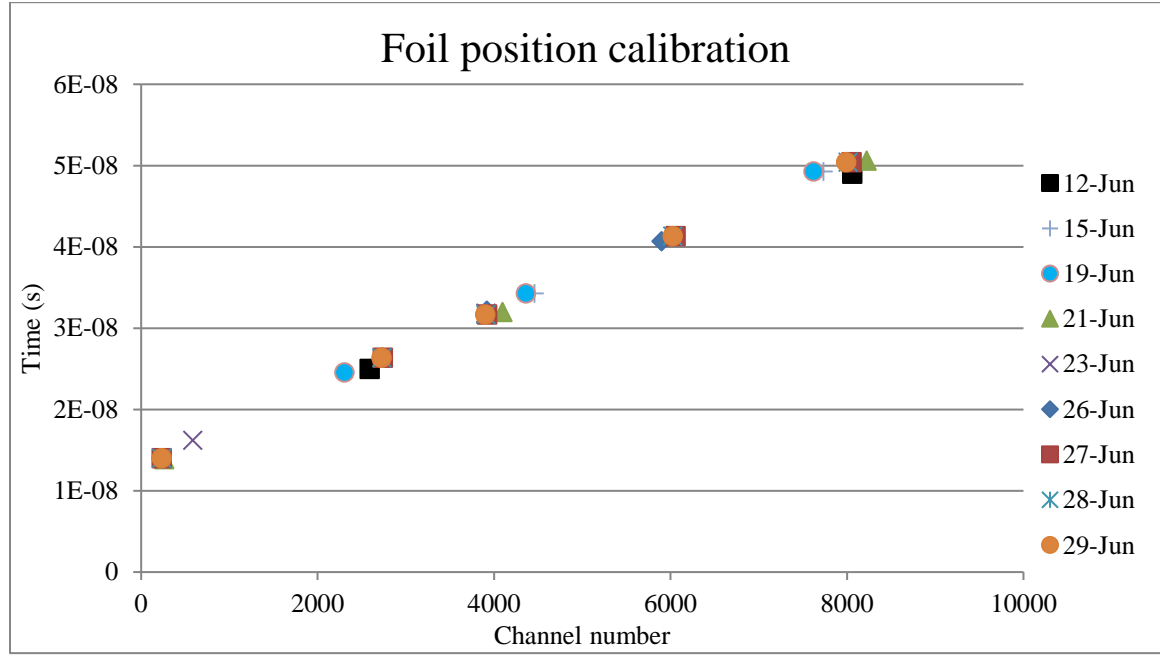
Figure 24: Calibration for position measurements (using a range of different cable delays).

Table 3: Calibration equations for position measurements plotted points in Figure 24.

Date	Calibration
12-Jun	$4.61249 * 10^{-12} * X + 1.28298 * 10^{-8}$
15-Jun	$4.63110 * 10^{-12} * X + 1.3950 * 10^{-8}$
19-Jun	$4.56772 * 10^{-12} * X + 1.3950 * 10^{-8}$
21-Jun	$4.61210 * 10^{-12} * X + 1.3007 * 10^{-8}$
23-Jun	$4.64077 * 10^{-12} * X + 1.3396 * 10^{-8}$
26-Jun	$4.63963 * 10^{-12} * X + 1.3433 * 10^{-8}$
27-Jun	$4.63676 * 10^{-12} * X + 1.3299 * 10^{-8}$
28-Jun	$4.66485 * 10^{-12} * X + 1.3308 * 10^{-8}$
29-Jun	$4.67439 * 10^{-12} * X + 1.3298 * 10^{-8}$

The calibration equations found in this chapter are used in chapter 4 and 5 for the appropriate measurements to convert from channel number to time-of-flight.

4 Geometric Dependencies in the TOF Measurements

Since the upgrade to larger square carbon foils (4.8 cm by 3.8 cm) on the front of the timing modules, the accepted solid angle from the source has increased, giving a larger range to the particle distance travelled between timing foils. This has led to a question on whether the timing resolution has gotten worse from a broadening of the path length. The ^{239}Pu source was placed behind the foil for the first timing module. These blockers were placed over the second timing module in front of the foil to 'block' alphas except those passing through the hole that is cut out.

4.1 Set-up

First, we wanted to explore what effects there are due to where particles interact with the carbon foils, using the set-up described in Figure 7, on the time-of-flight measurements. For most of these runs the ^{239}Pu source was positioned in the Off-Centered source position labeled in Figure 26, slightly above center due to the position of the already machined source mount, Figure 25 show another depiction of the blocker position. This was done for runs labeled: 6/23 no blocker, 6/15 center blocker, 6/19 top left blocker, and 6/21 bottom right blocker. The source was moved to the Centered Un-Collimated source position, the true center of the foil, and used for one run labeled "exact center" with a center blocker on the second timing module to determine TOF for center-to-center alpha particles.
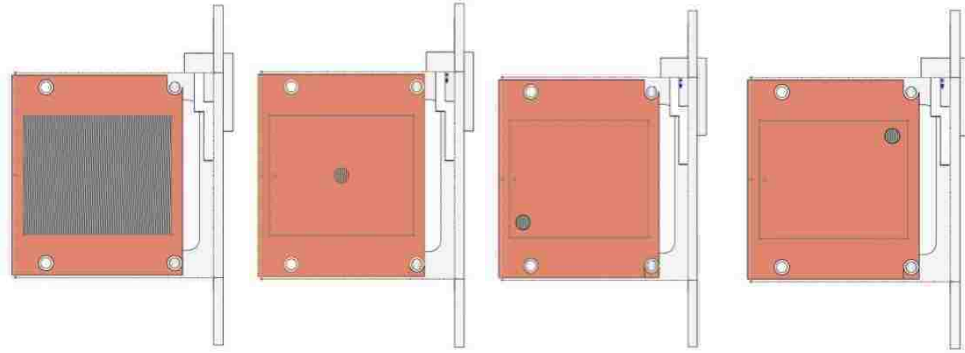
Figure 25: (left) Carbon foil and (center left to far right) blocker position in the center, top left corner, and bottom right corner. Labels are for position relative to the MCP, which is positioned to the right in this figure.
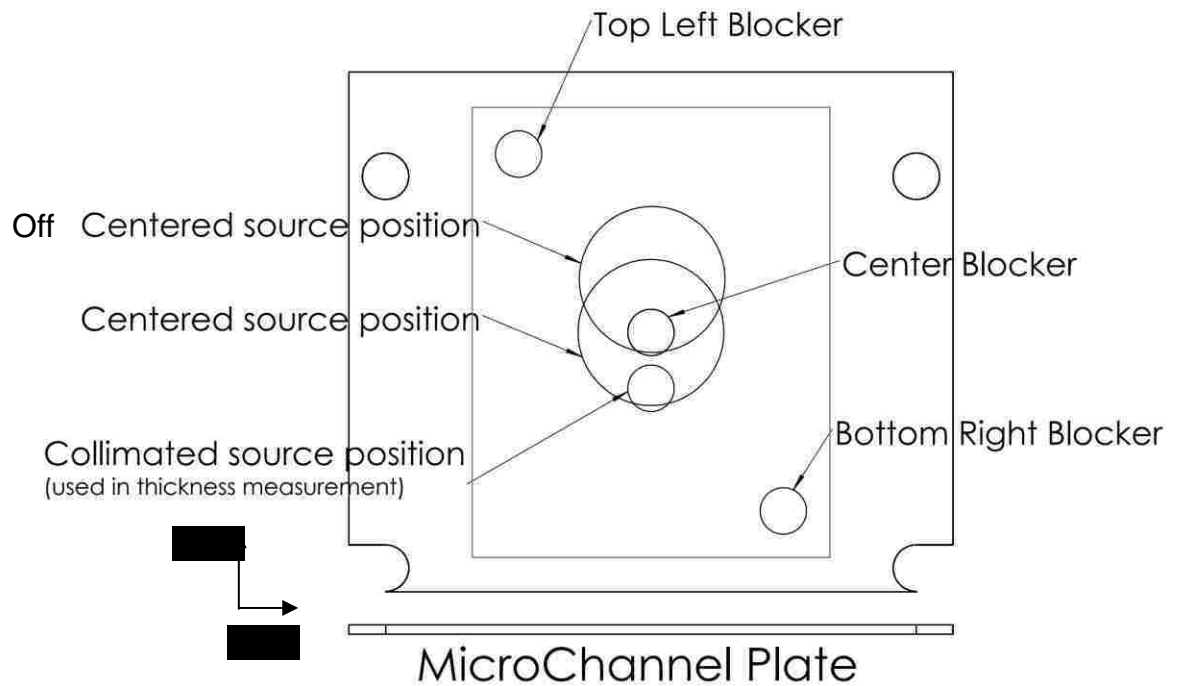
Figure 26: Blocker and source position labels.

The blockers are labeled the way they are in relation to the MCP. In Figure 26 the MCP is shown on the bottom of the blocker, hence the terms top left and bottom right. Shown in Figure 27 the timing modules are rotated 90° so that the MCP is vertical.
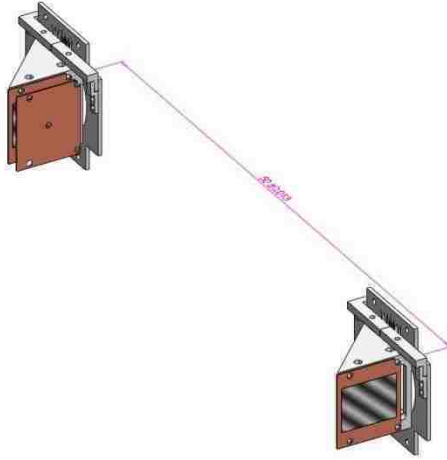
Figure 27: TOF set-up with blocker on the second timing module.

With a 20 $\mu g/cm^2$ carbon foil on both MCPs time-of-flight measurements were taken for 5 different situations. TOF measurements using the exact center of the first and second carbon foils was used to verify the distance between the two carbon foil faces, as pictured in Figure 27. The off-centered source holder is offset from the exact center of the foils but has a diameter of 1.57 cm so it still overlaps the exact center of the foil position. Table 4 describes the distance from the center of foil and of the source position, a dimensioned drawing is in Appendix A.2. The distances from the center of the off-centered source position (not the "centered source position") to the center of the 5 mm diameter hole of each of the blockers is shown in the Table 4, using a value dx as 50 cm (foil-to-foil distance).

Table 4: Foil blocker distances using a value of 50 cm for the TOF distance.

	dz (cm)	dy (cm)	Distance (cm)
Center Blocker	0.57	0	50.003
Top Left Blocker	1.349	1.425	50.038
Bottom Right Blocker	2.489	1.425	50.082

4.2   Results

The following four graphs show 24 hour runs of No blocker (Figure 28), Center (Figure 29), Top Left (Figure 30), and Bottom Right (Figure 31) blockers. As described in the calibration of time-of-flight, chapter 3, after each run a timing calibration was performed. In Table 3 the calibrations varied slightly from each other which is why the appropriate calibration was applied to each data set.

34
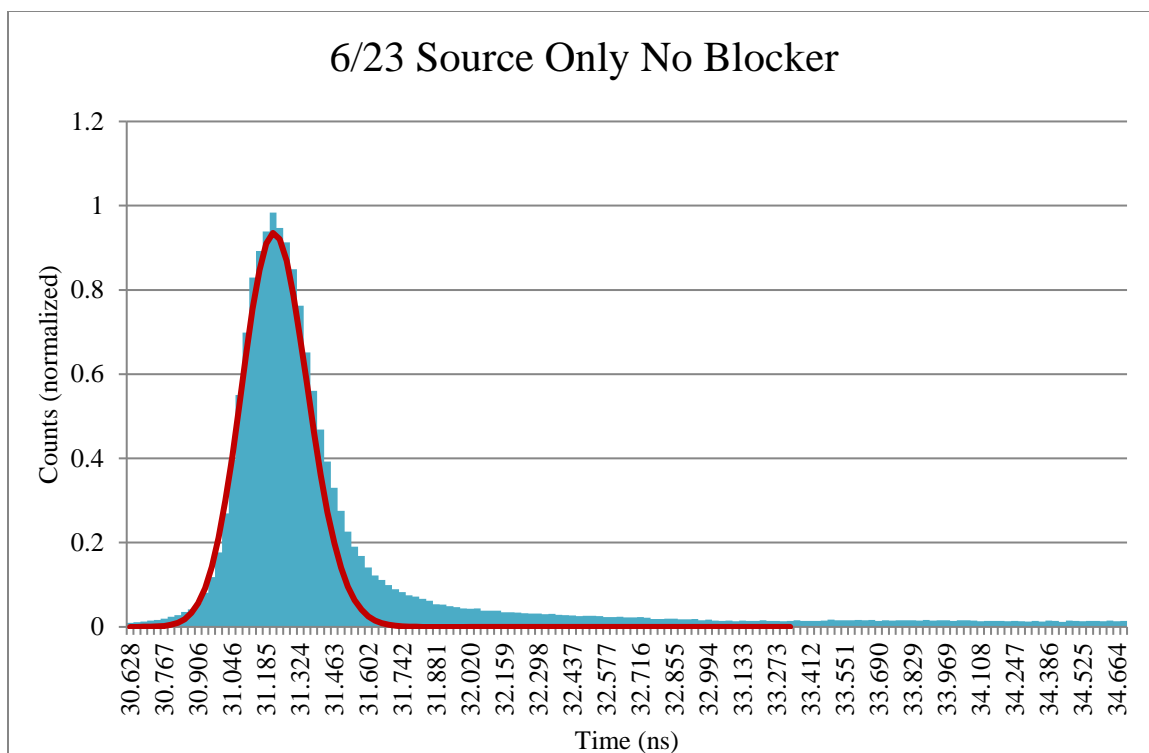
Figure 28: ^{239}Pu source and No blocker of TOF spectrum.
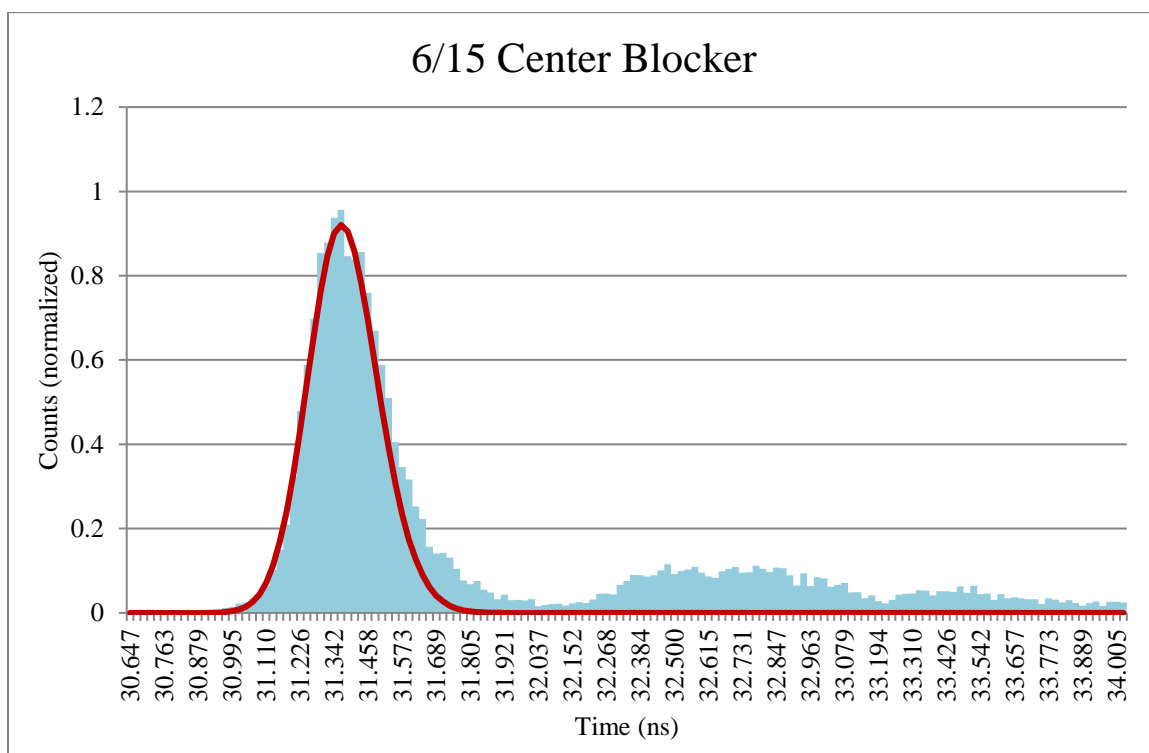
Figure 29: ^{239}Pu source and Center Blocker TOF spectrum.
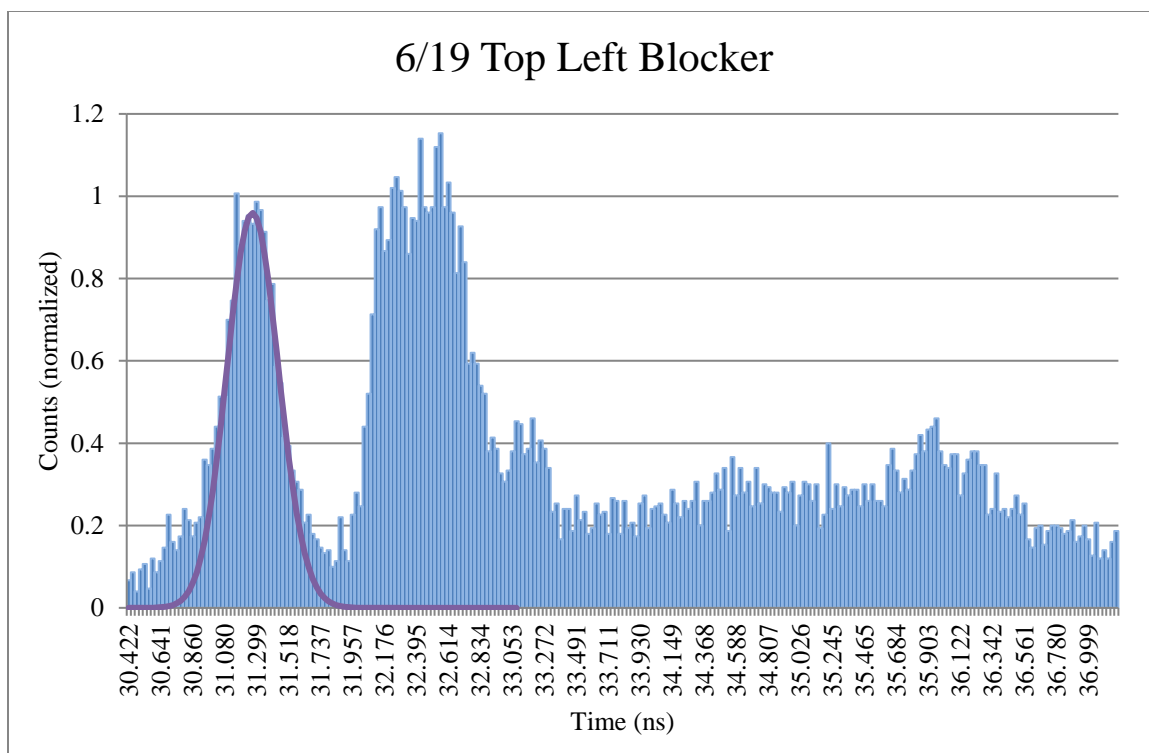
Figure 30: ²³⁹Pu source and Top Left Blocker TOF spectrum.
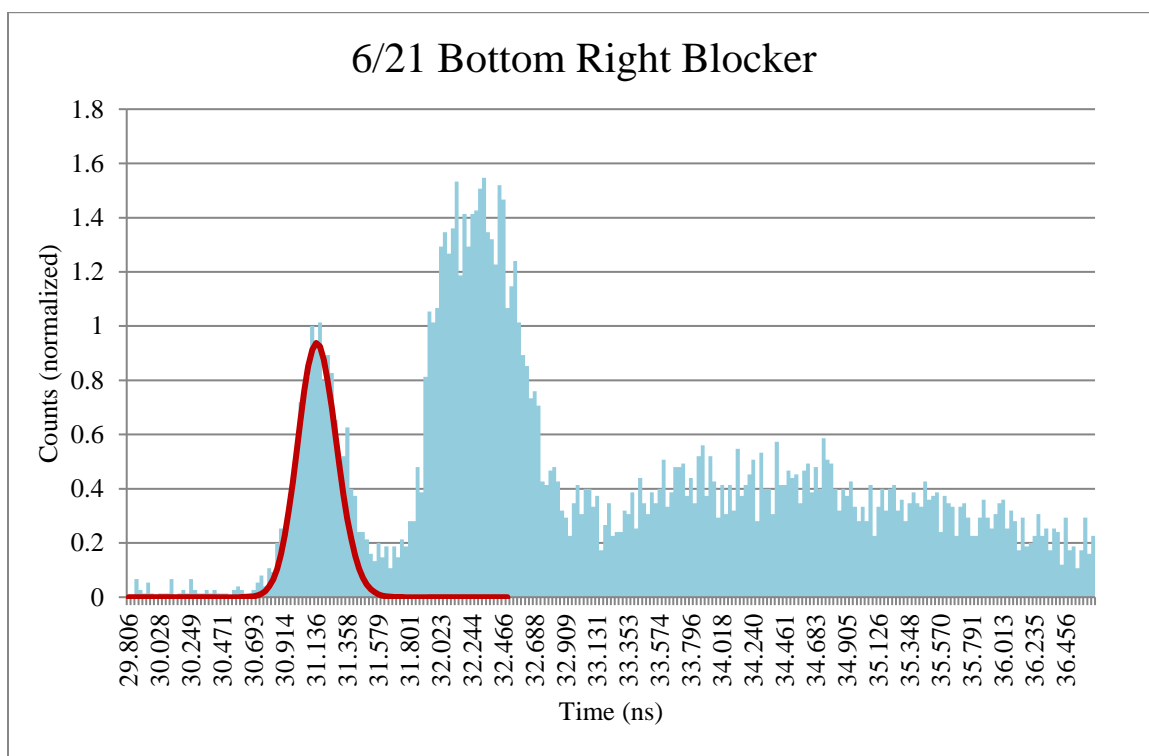
Figure 31: ²³⁹Pu source and Bottom Right Blocker TOF spectrum.

Using the calibrations after each run as described in chapter 3, the data was converted to time-of-flight from channels, as used in Figure 28-Figure 31. Table 5 is a summary of the peak position and the standard deviation of the peak distribution of each run. The distance is also calculated from the time-of-flight, subtracting the dz and dy components to find the dx, carbon face to face distance.

Table 5: Summary of positional effects

Run	Sigma (s)	Counts/Hr.	5.156 MeV alpha time (s)	Calculated distance (cm)
6/23 no block	1.27E-10	11085	3.110E-08	49.120
6/15 center block	1.1E-10	623	3.115E-08	48.967
6/19 top left	1.7E-10	91.7	3.116E-08	49.048
6/21 Bottom right	1.3E-10	34.8	3.119E-08	49.065
6/27 Exact center	9.5E-11	301	3.109E-08	48.950

The TOF as a function of point-to-point distance for all the data is presented in Figure 32. The distance between the foils was determined using the centered source behind foil 1 with the centered blocker in front of foil 2, and the other distances were calculated from this. Expected TOFs were calculated for these different distances, and there is some discrepancy between measurements and the expected values.

The foil and mirrors are both mounted on the same wedge. For each blocker or source position change, the foil-mirror wedge had to be removed and put back in place, leading to possible misplacements between runs. Calculating from the timing, the wedge was put in the same place with a standard deviation of 0.071 cm. This very high sensitivity to

small position shifts suggests a different method for placing the wedge or changing the blockers should have been examined.
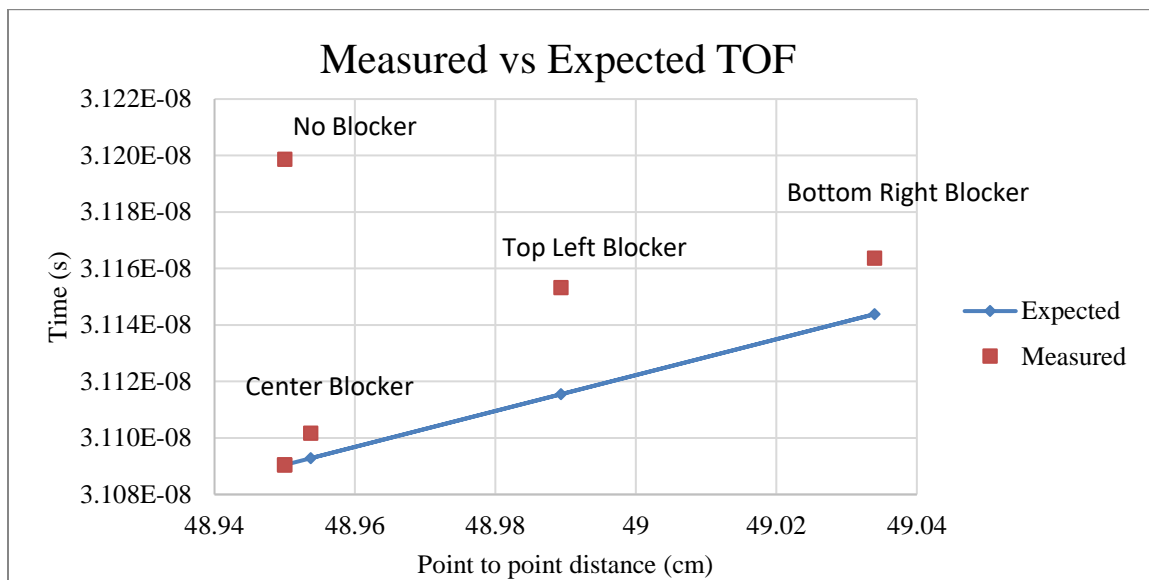
Figure 32: TOF vs. point to point distances.

Physically measuring the distance between the two faces on the spectrometer using a ruler gives a value of 19.4 ± 0.13 inches or 49.28 ± 0.32 cm. This was only measured once after all the runs; it was not thought to be an issue, until the result from using the time calibration were completed.

Spacers are required to keep the mirror electrodes from shorting, which can inadvertently change the distances. The difference in position from 50 cm means that there were more spacers from the face of the mirror to the carbon foil on MCP 2 than on MCP 1, reducing the foil-to-foil distance from what was originally designed. This has since been fixed so that the distance is once again 50 cm.

4.2.1   Second Peak in Blocker Data

Noticeably, each run with a blocker has a second bump following the main peak, but there is no additional spectrum when the blocker is not in place. This is exaggerated in the corner-hole runs and each has a slightly different shape. This may be due to the size of the MCP face being smaller than the size of the foil used. The mirrors used to direct the ejected electrons to the MCPs are optimized for the very center of the foil. Whatever effects that are brought by the FR4 blocker in place are increased the further away from the optimized center of the carbon foil.

A MCNP simulation of the experimental set-up was done with the 5 mm diameter hole in center of the FR4 to examine the contribution of alpha particle scattering. The alphas do interact with the edges of the FR4 in some way but produced very few counts of a lower energy, which would translate to a longer TOF in the spectrum. Instead of contributing to the main peak, this down scatter is separated. The energy spectrum through the hole, including scatter, is presented in Figure 33. In Figure 34 the energy is converted to time-of-flight, using a 50 cm path length, to have an idea of where these peaks shown up on the actual data taken above. The vertical scale is greatly expanded to show the effect of scatter, which is much smaller than the main peak with a height of 100,000 counts.

^{239}Pu 5.156 MeV through 20 μg/cm^2 Carbon foil
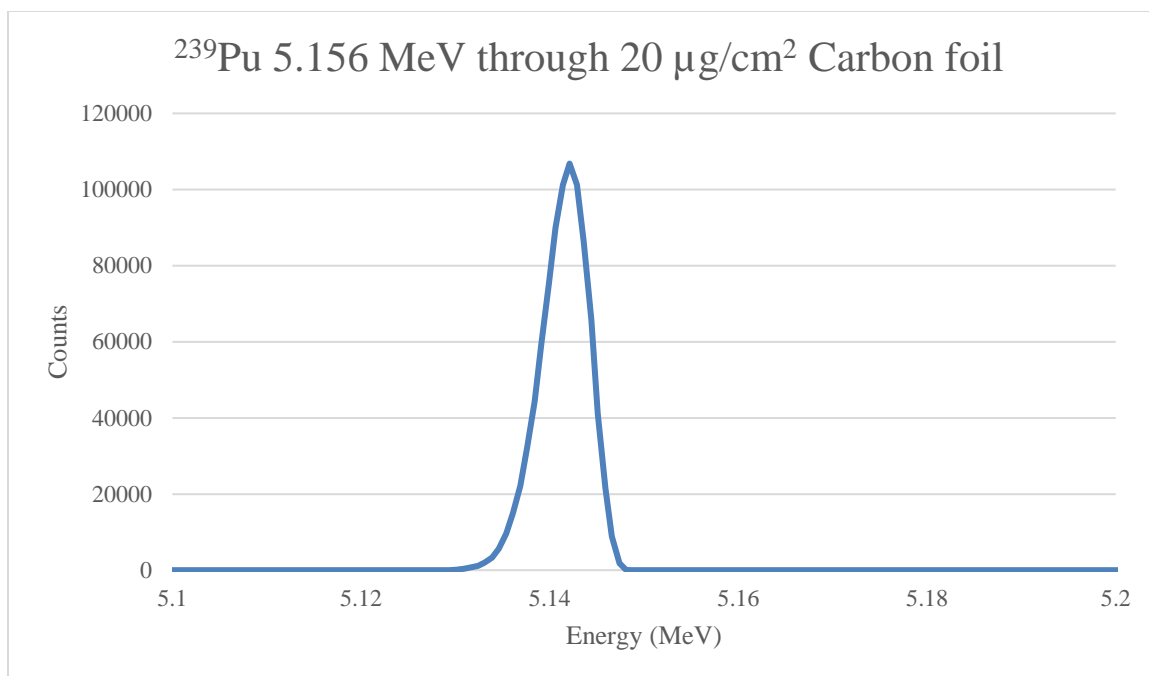
Figure 33: MCNP experiment simulation.

MCNP6 through a center FR4 Blocker
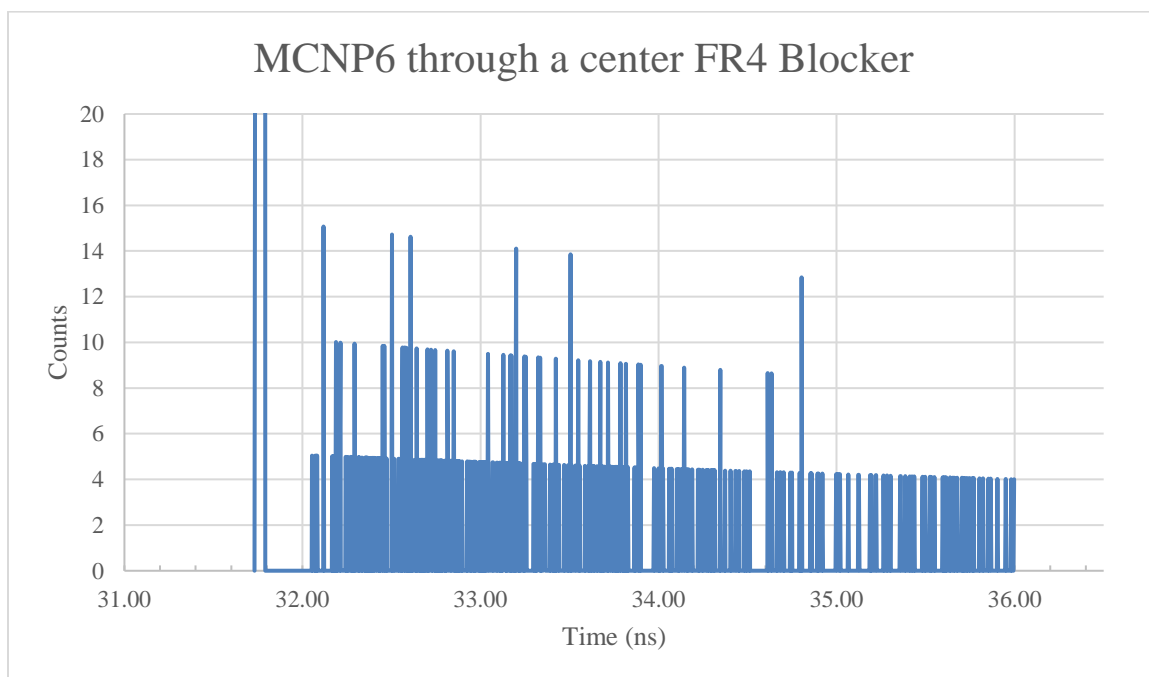
Figure 34: MCNP time-of-flight simulation.

4.2.2   Alpha Particle Timing Resolution Using a Restricted Geometry

Using the exact center to center values, the distance between the foils on the two MCPs was determined to be 48.95 cm for these runs. The centimeter offset has since been removed for foil thickness and other runs. Using the ^{239}Pu alpha source and the 20 μg/cm^2 carbon foils with no blocker resulted in a FWHM of 298 ps. This includes alpha particles entering the second foil not only near the center but away from the center, accepting a spread in the distances travelled and thus an expected spread in TOF for the different alpha particles. Using a center blocker on the second MCP reduced the σt even lower, to 258 ps and 223 ps depending on where the source was located. When the MCP 2 carbon foils had the corner blockers on the FWHM increased and the count rate decreased. The higher count rate using the center blocker shows that there is a difference in detection efficiency over the face of the foil, with a maximum efficiency for particles near the center. As the path length and thus TOF is different for particles striking near the edges vs. the center, this efficiency difference serves to reduce the broadening in the TOF distribution for alpha particles. The difference in efficiency is thought to be due to the alphas ejecting very few electrons, so positioning is very important for electrons to strike the MCP and produce a signal. Fission fragments lose far more energy in the foils and eject far more electrons, so it is possible that the efficiency is not as position sensitive with fission fragments. This has not been studied here though.

5   Carbon Foil Thickness Dependence in the TOF Measurements

When particles pass through thicker carbon foils they will lose more energy than through thinner foils, and increased energy loss increases energy broadening, thus broadening resolution. Energy loss and straggling calculations using SRIM and MCNP, and experimental measurements, are summarized later in chapter 7. In the past, it was thought that 20 $\mu g/cm^2$ were too thin to use as a conversion foil due to the possibility of breaking. With the introduction of a wire grid backing the foil, we are now able to test the thinner and larger area foils.

As discussed in chapter 8, we are reconstructing particle mass by correlating energy and TOF for each particle. This means that we need to understand the energy and timing resolution for single particles. The TOF distributions and energy distributions though give us information on a large number of particles with a broadening of the distribution due to different interactions with the foil by each individual particle. While the energy and TOF distributions (in terms of δE/E and δt/t) are is typical inputs for uncertainty analysis to find δm/m as these quantities are measurable, it appears more appropriate to understand the system without straggling due to foils. While this is impossible to measure directly, as we wouldn't get a signal in the TOF and we wouldn't hold gas in the IC, we can back out the system response with zero thickness foils and a monoenergetic source. The energy broadening of the energy distribution of the alpha particles from passing through foil 1 means there is a broadening of the velocity distribution, and thus a broadening in the TOF distribution.

In the case of the TOF, by analyzing the time straggling, the broadening of the resulting distribution, from different thickness of foils we can infer what the FWHM for the TOF would be for zero thickness foils. That is, we can interpret the TOF results for a monoenergetic beam with no straggling, more closely to looking at the response for a single particle.

5.1   Set-up

The TOF set-up used our typical 50 cm foil-to-foil distance. The ^{239}Pu source was mounted behind foil 1, as in Figure 7, and was collimated with a diameter of 5 mm and positioned 0.6 cm below the exact center of the foil, as labeled collimated source position in Figure 26. The thicknesses of both foils were varied, with the foil thicknesses of foil 1 and 2 matching, using 20, 55, and 100 $\mu g/cm^2$ thicknesses for each. Results are presented for each pairing, for both energy loss and straggling. A center blocker is used for one run with the 20 $\mu g/cm^2$ foil, but due to a major decrease in efficiency the combination of a blocker and collimated source was only used for this one run.

5.2   Results

The data from each run is overlaid with a Gaussian fit of the three main alphas in ^{239}Pu, with the appropriate intensities from branching, and summed to produce a total peak explicitly shown in Figure 35 for the three dominant alpha energies from ^{239}Pu: 5105, 5144, and 5156 keV. The sigma of the sub-Gaussian peaks is set to be equal for all peaks

and that, as well as the amplitude, is found by a best fit of the sum line to the data. In all

other plots only the sum peak is shown for ease of viewing.
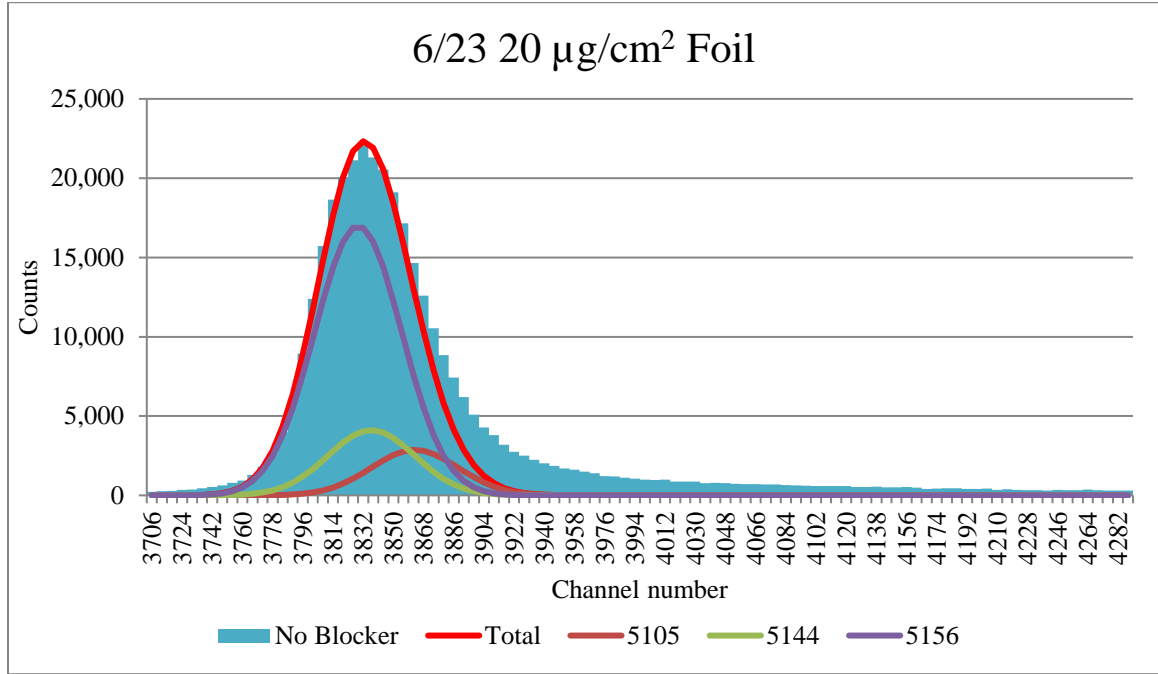
Figure 35: 20 µg/cm² carbon foil with Gaussian fits centered on the three dominant alpha energies from ²³⁹Pu, and sum peak of the fits.

The thinnest foil used was a 20 $\mu g/cm^2$, this is graphed in Figure 36 and a summary of

different runs using this thickness foils is given in

Table 6. This table gives the energy of the alphas expected after foil 1 as they enter the

TOF region, the calculated TOFs using these energies, the centroids of the peaks using

the multi-energy peak fit described, and the amplitude and sigma found for the best fit

Gaussian sum.

44

20 µg/cm² foils were expected to break, because foils this thin had not been used before. It was difficult to even mount the foils in the frames, through a process called floating, without breaking the foils. This was solved using a mesh backing affixed to the frames.

As the foils were more stable with the mesh backing, throughout all runs shown the same pairs of carbon foils for the three thicknesses were used. For the position measurements as well, with the benefit of the mesh backing, the same 20 $\mu g/cm^2$ foils were used throughout, which are the same 20 $\mu g/cm^2$ foils used for the thickness analysis.
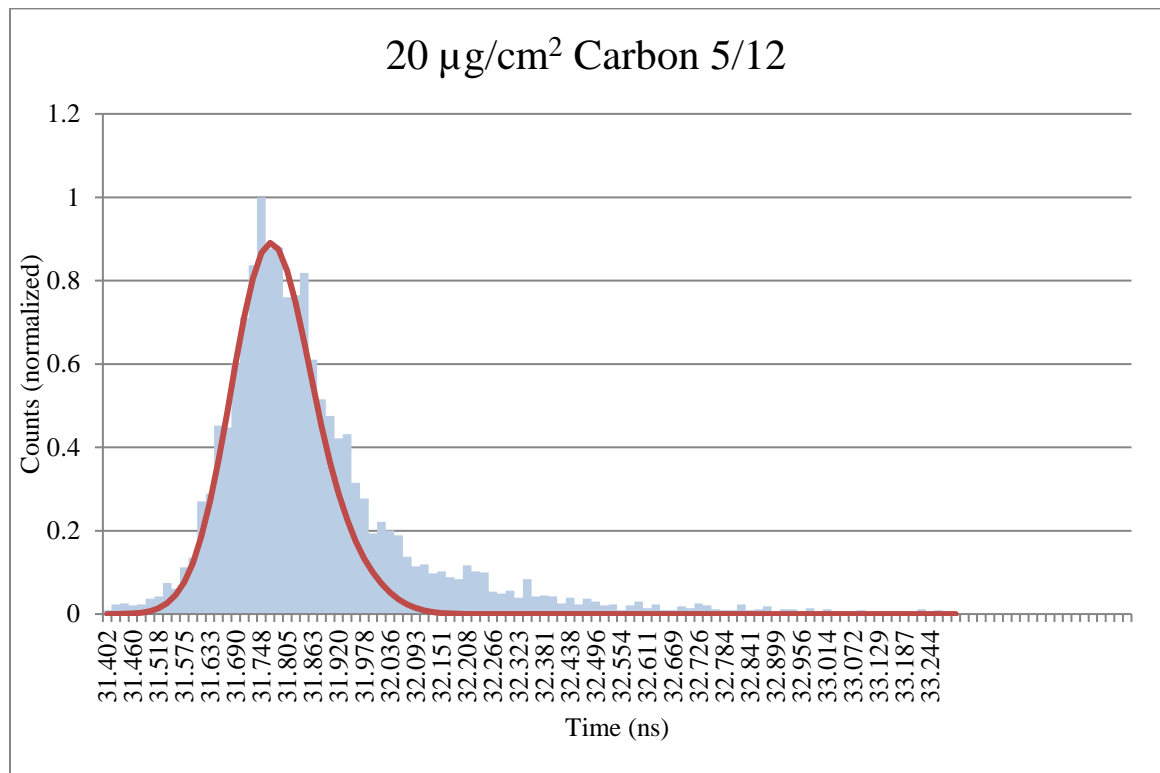
Figure 36: TOF spectrum with a collimated ²³⁹Pu source and 20 µg/cm² foil.

Table 6: Peak information in terms of channel number, with centroids of the different energy alphas as extracted from fits given for each date, using 20 μg/cm² thick foils.

	Energy after foil	Time (50cm)	5/10	5/12	With center blocker 6/10
Alpha1	5.140	3.175E-08	3868	4655	3855
Alpha2	5.128	3.179E-08	3877	4666	3864
Alpha3	5.089	3.191E-08	3909	4704	3896
Run Time (hr)			1.7	48	67
Sigma (ps)			95	85	85
Amplitude			145	430	110

As far as the order the experiments were performed, the 55 $\mu g/cm^2$ thick foil

experiments were the first to be run and there were problems with the setting of the

CAEN software triggering values. The first 3 runs shown in Table 7 were all taken with

different settings and, as seen by the amplitude of the fits vs. the run time (in hours) the

count rate was very low. Starting on April 25 the issue with the settings was fixed with

the software update mentioned, giving a reasonable count rate but the peak locations are

in extremely low channels compared to the 20 and 100 µg/cm² foil runs. Note that these

early runs are also associated with the poor calibrations, suggesting the data should be

retaken. The run taken on April 27 is graphed in Figure 37, and all the runs summarized in Table 7.
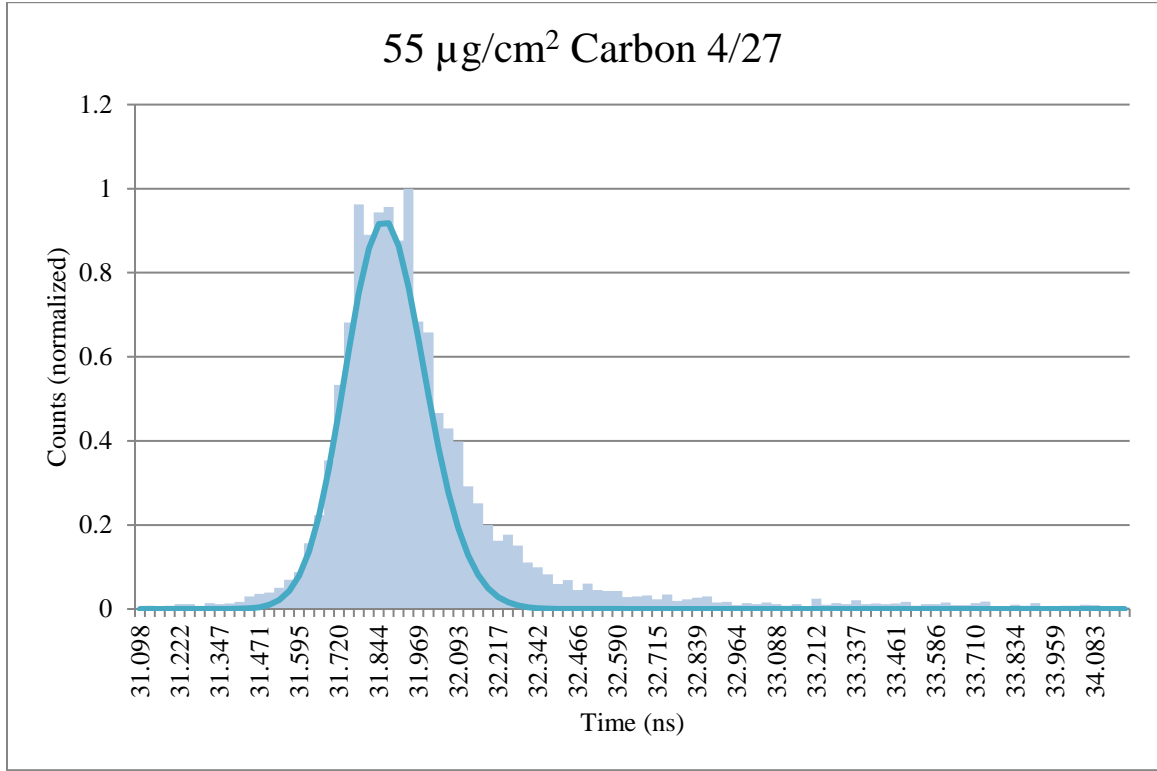
Figure 37: TOF spectrum with a collimated ^{239}Pu source and 55 μg/cm^2 foil.

Table 7: Peak information in terms of channel number, with centroids of the different energy alphas as extracted from fits given for each date, using 55 μg/cm^2 thick foils.

	Energy after foil	Time (50cm)	4/20	4/21	4/24	4/25	4/27	4/28
Alpha1	5.112	3.184E-08	5000	4901	4815	2880	2890	2902
Alpha2	5.100	3.188E-08	5012	4913	4826	2887	2897	2909
Alpha3	5.061	3.200E-08	5053	4953	4866	2910	2920	2933
Run Time (hr)			24.61	19.9	71.7	0.4004	25.5	19.5
Sigma (ps)			250	120	120	120	116	116
Amplitude			75	30	75	35	800	700

47

The thickest foil used is a 100 µg/cm^2 carbon foils with the spectrum graphed in Figure 38 and a summary of the different runs in Table 8.
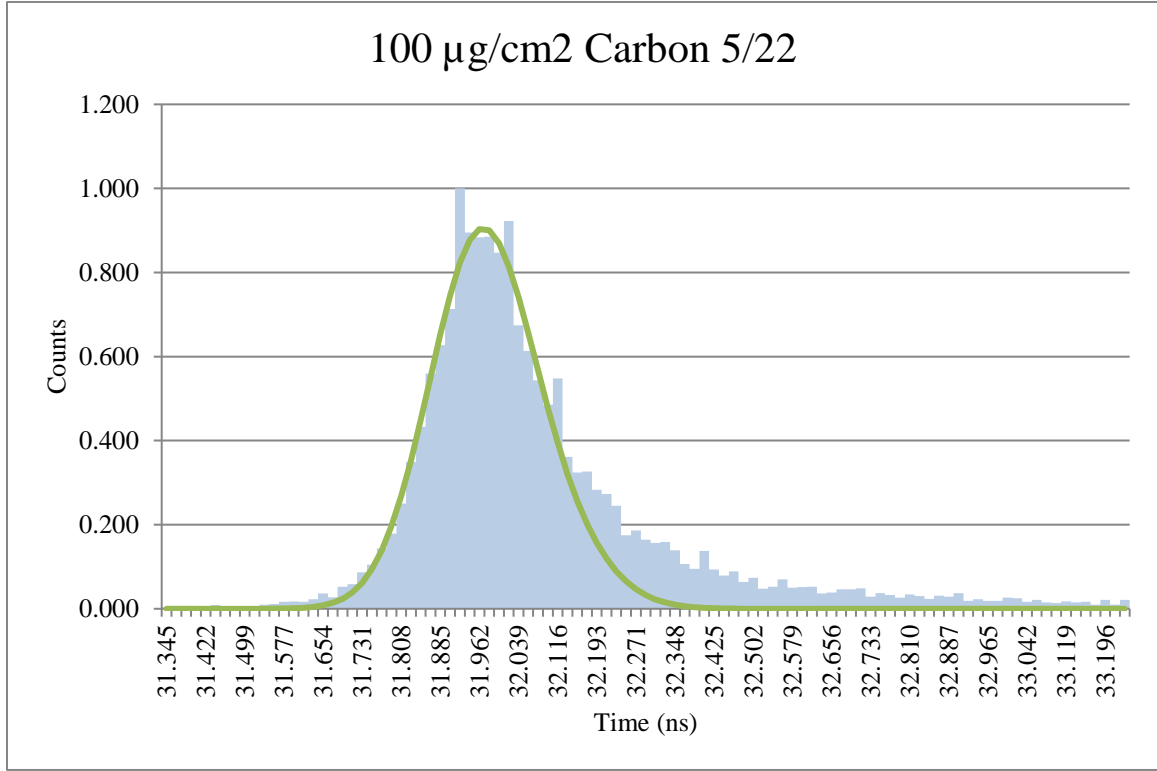
Figure 38: TOF spectrum with a collimated ^{239}Pu source and 100 µg/cm^2 foil.

Table 8: Peak information in terms of channel number, with centroids of the different energy alphas as extracted from fits given for each date, using 100 µg/cm^2 thick foils.

	Energy after foil	**Time (50cm)**	**5/18**	**5/22**	**5/29**
Alpha1	5.076	3.195E-08	4730	4696	3560
Alpha2	5.064	3.199E-08	4742	4707	3571
Alpha3	5.025	3.211E-08	4781	4742	3606
Run Time (hr)			48	48	69
Sigma			120	100	130
Amplitude			900	740	5500

Plotting the FWHM as a function of foil thickness in Figure 39 we clearly see the

expected decrease in straggling with the decrease in thickness.

FWHM of 20, 55, 100 µg/cm^2 Carbon foils
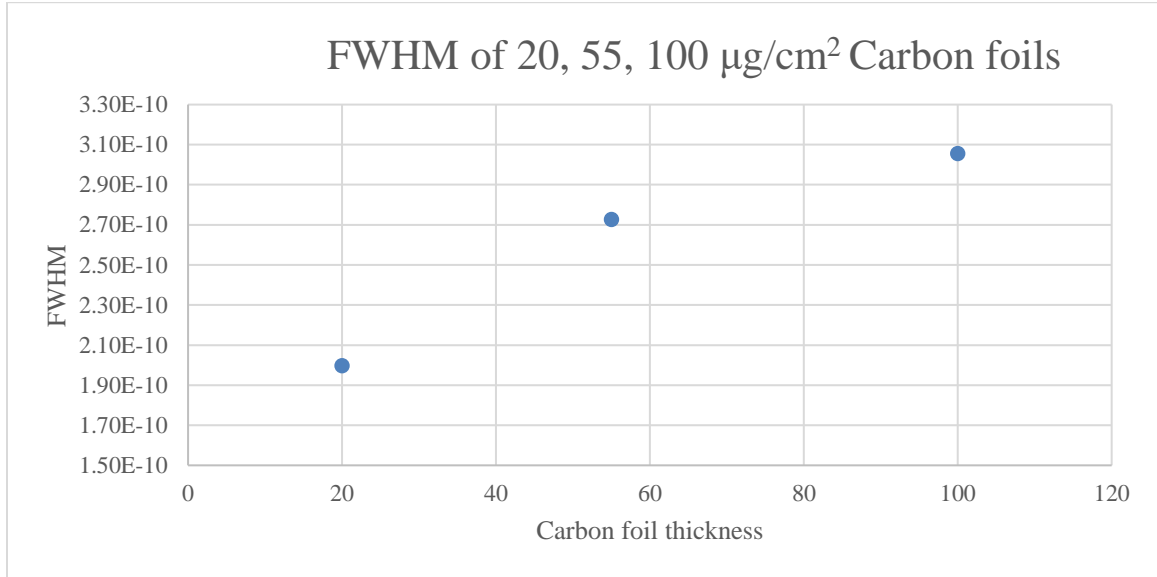
Figure 39: FWHM as a function of carbon foil thickness

There are factors other than the foil thickness that contribute to the widths, such as the

broadening due to the source itself and the broadening of the system. As uncertainties

add in quadrature, we can express these broadenings as $\sigma^2_{total} = \sigma^2_{foil} + \sigma^2_{other\ factors}$, or

equivalently for FWHM. Following this, by plotting the square of the FWHM as a

function of thickness, we can extrapolate back to zero foil thickness and to the FWHM^2

caused by all other factors, shown in Figure 40. That is, we are extrapolating back to the

FWHM of the distribution for zero thickness foil to understand the behavior of the system

with a monoenergetic beam and no straggling in the foils. The energy spread of the

source will be addressed in the full analysis in chapter 8. For the extrapolation plot, since

the 55 $\mu g/cm^2$ foil had a strangely low channel number for the peak centroids, it seems

appropriate to compare just the FWHM of the 20 and 100 $\mu g/cm^2$ foils for clearer

results. For a zero thickness foils, the extrapolated FWHM of the TOF is 168 ps.
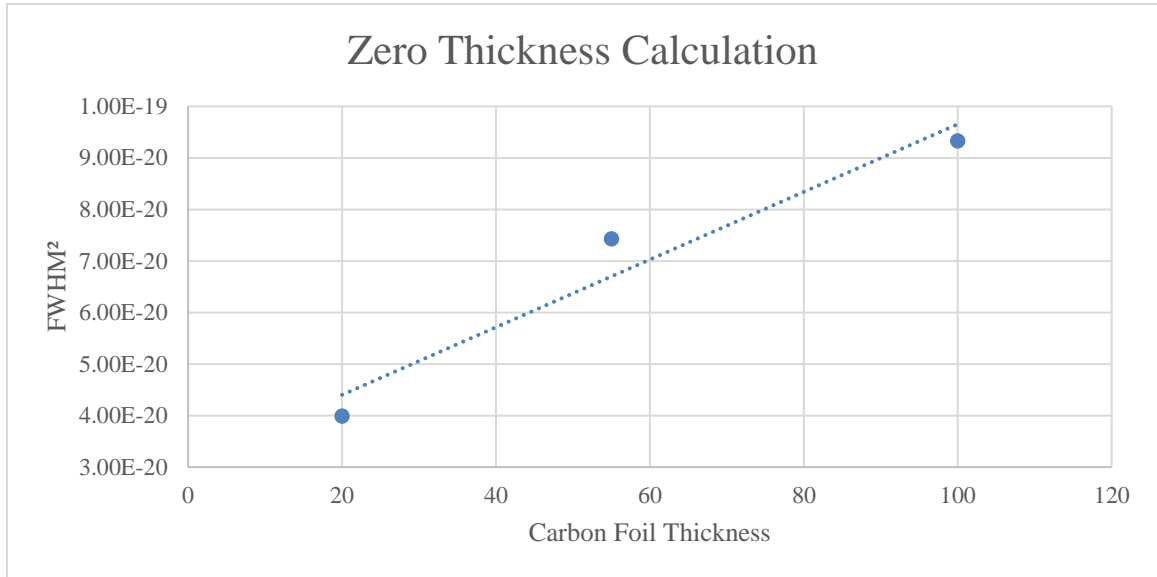
Figure 40: Zero thickness calculation

This is much better than our prior measurement shown in Figure 9 in chapter 2, with a

FWHM of the TOF of 371 ps, and so this is addressed. That previous FWHM was with

total width of the peak and didn't consider the different branching isotopes of ^{239}Pu.

When splitting it into different isotopes the FWHM is 329 ps, shown in Figure 41. This

still has the broadening from 80-100 μg/cm² carbon foils, and the additional broadening

that energy straggling, and thus velocity straggling, contributes over a 1 meter flight path

vs. the 50 centimeters addressed in this chapter. As the flight path and thus TOF is also

doubled, this latter broadening is expected to cancel out when finding proportional

uncertainty, δt/t. System based effects on broadening should not double and so the total

δt/t is expected to be lower for longer TOF flight paths.
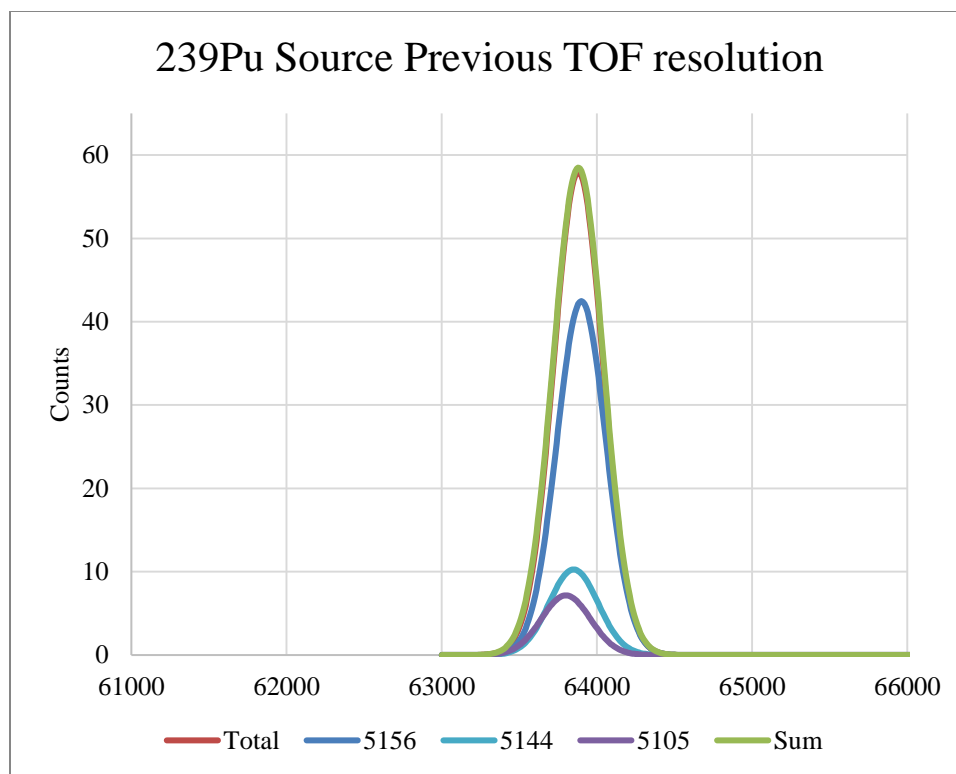
Figure 41: ^{239}Pu alpha particle TOF results for a 1 m flight path and 80-100 μg/cm^2 thick carbon foils, as shown previously in Figure 9 but with the alpha subpeaks explicitly fit to find FWHM values for single energy alphas.

6   Energy Loss Theory

We have examined TOF and TOF broadening as a function of different carbon conversion foil thicknesses. The TOF slowing and broadening from the foils is caused by energy loss and energy broadening in the conversion foils. We can study this energy loss and broadening directly. As energy loss and straggling is also important for the SiN entrance window to the ionization chamber, we study this for both carbon foils and thin SiN windows.

There is an explicit need for this information for our work, after seeing a difference in broadening when using different conversion foils on each timing module, we can look at the energy broadening and loss with simulations and an experimental set-up. We must incorporate the energy lost in the foils and window to the energy add back described in chapter 2.3.4 energy loss correction. To understand the energy loss, we compare three different approaches, SRIM simulation, MCNP simulation, and experimental measurements using a silicon semiconductor detector and observing the energy loss from ^{252}Cf alphas and fission fragments. In chapter 7 the experiment and results will be discussed; this chapter will discuss stopping power theory and what calibration methods are used.

6.1   Stopping Power Theory

According to Bohr's theory, the electronic stopping power of an ion with an atomic number of Z_1 and velocity v is written as

$$-\frac{dE}{dx} = \frac{4\pi Z_1^2 e^4}{m_e v^2} N Z_2 L$$

N is density of target atoms, Z_2 is the atomic number of the target atoms, m_e and e are the electron mass and charge, L is the stopping number (Bohr and Wheeler 1939).

As the projectile loses energy, the velocity decreases and the stopping power increases. For very thin targets though, as we hope for our carbon conversion foils and ionization chamber entrance window, the loss is slight enough that the stopping power is approximately constant and energy loss and thickness should be linearly related.

As this is the expression for interaction of the charged projectile with the electrons of the target material, the charge state of the projectile is the important quantity for Z_1. For alpha particles, this is just 2 for most of the projectile path, but for heavy projectiles like fission fragments the charge state of the projectile varies as a function of the velocity of the projectile and the binding energies of the atoms involved due to charge exchange, making direct application of this equation difficult. For this reason, simulations such as MCNP and SRIM, that estimates the charge state, are extremely useful.

6.1.1 SRIM Energy Loss

The software package, The Stopping and Range of Ions in Matter (SRIM) (J. Ziegler 2017) uses the relativistic version of the Bethe-Bloch stopping power equation and includes additional corrective terms, such as the Shell correction and Density effect.

Equation 3

$$S = \frac{k\,Z_2}{\beta^2} Z_1^2 [L_0(\beta) + Z_1 L_1(\beta) + Z_2^2 L_2(\beta) + \cdots]$$

L_0 contains all the correction factors of the Fano factor formula and constants (Ziegler 1999). SRIM is well benchmarked to alpha particle data, but there is far less work on fission fragments and so this work must be compared with other simulations as well. SRIM stopping power accuracy graphs compared to experimental data for alphas and fission fragments are shown in Appendix A.1, where there is a wealth of data for alpha particle benchmarking and a paucity of data for fission fragment benchmarking (J. Ziegler 2017).

6.1.2 MCNP Energy Loss

The Monte Carlo N-Particle code (MCNP) is optimized for neutrons but, with the use of different libraries, can be applied to different particles, in our case the average heavy and light fission fragments of ^{252}Cf. The energy loss through different thickness foils and materials can also be simulated in MCNP. Based on libraries in MCNP the stopping

power used in calculations are collisional and radiative. The electronic collisional

stopping power is set as:

$$-\left(\frac{dE}{ds}\right) = \frac{10^{24}\alpha^2 h^2 c^2}{2\pi mc^2} Z\left\{ln[\tau^2(\tau+2)]C2 + C3 - \beta^2 + C4\left(\frac{\tau}{\tau+1}\right)^2 - \delta\right\}\frac{1}{\beta^2}$$

where $\alpha = \frac{2\pi e^2}{hc}$, h is Planck's constant, τ is kinetic energy , m is rest mass, and β is v/c.

The radiative stopping power is:

$$-\frac{dE}{ds}|_{rad} = 10^{24}Z(Z+\bar{\eta})(\alpha r_e^2)(T+mc^2)\Phi_{rad}^{(n)}$$

where Φ is the scaled electron-nucleus radiative energy loss cross section based on

library data. Radiative stopping power, Bremsstrahlung, is much more important for light

charged projectiles such as electrons going at extremely high velocities than for atoms at

fission energies, or even alpha particles, and so collisional stopping power, interactions

with the electrons in the target, is the only important part for our work.

6.1.3 Pulse Height Defect

The energy loss of the projectiles can be calculated or simulated, but to extract measured

values requires dealing with real instrumentation with real limitations. Ideally, signals

from an energy detector are dependent only on the energy of the incident projectile. There are several factors modifying that though. For example, there may be energy loss in entering a detector that then is not recorded by the detector. Also, the energy deposited in the detector may not be read out the same way for different particles. For highly charged particles such as fission fragments, the ionization caused in the detector may be very dense, which can lead to charge recombination and a suppressed signal size, called a pulse height defect (PHD). PHD is formally defined as the difference between the true energy of the heavy ion and the apparent energy, determined from an energy calibration from alpha particles (Forgue and Kahn 1967).

Different fission fragments may have different masses and charge states. With more mass, the same kinetic energy translates to a lower velocity. In addition, charge state increases with mass. Thus, higher masses may have higher stopping powers which leads to denser ionization in the detector and more recombination, and more of a pulse height defect, hence a mass dependent PHD. This mass dependence is minimal in gas ionization detectors, and a simple linear relation can be found between the pulse height and the energy deposited, $E = a*Ph + b$, with E being energy, Ph being pulse height, and a and b the slope and offset of the linear relation, respectively. Silicon detectors, being solid, have a much higher ionization density and a more noticeable mass dependent pulse height defect, this is addressed in the following section.

6.2   Mass Dependent Pulse Height Defect

As the particles pass through the carbon foils and the SiN window, they will experience interactions with the material and lose energy (Schmidt, et al. 1976). Calculating the energy loss from the carbon foils is important to consider, as it is a part of the energy add back as discussed in chapter 2.4. While SRIM had been used in the past to calculate the energy loss through the carbon foils and window, SRIM is better benchmarked for alphas than for fission fragments and detector measurements would give more confidence in the energy add back values. The general form of the energy calibration of the solid-state detector for fission fragments is (Schmitt, Kiker and Williams 1965)

Equation 6

$$E = (a + a'M)x + b + b'M$$

where a, a', b, b' are constants for a detector operated under constant conditions. In the Schmitt et al. paper for Si surface barrier detectors, referenced above, the constants are:

$$a = {24.0203}/{(P_L - P_H)},$$

$$a' = {0.03574}/{(P_L - P_H)},$$

$$b = 89.6083 - aP_L,$$

$$b' = 0.1370 - a'P_L \,.$$

 E and M are the ion energy and mass respectively, and x is the corresponding pulse

height. P_L and P_H are the centroid channels of the light and heavy peak.   Schmitt et al.

calibrated on the relation of Br and I ions and alpha particles as shown in the Figure 42.

This calibration method is referred to as "Schmitt Calibration" in the rest of this paper.
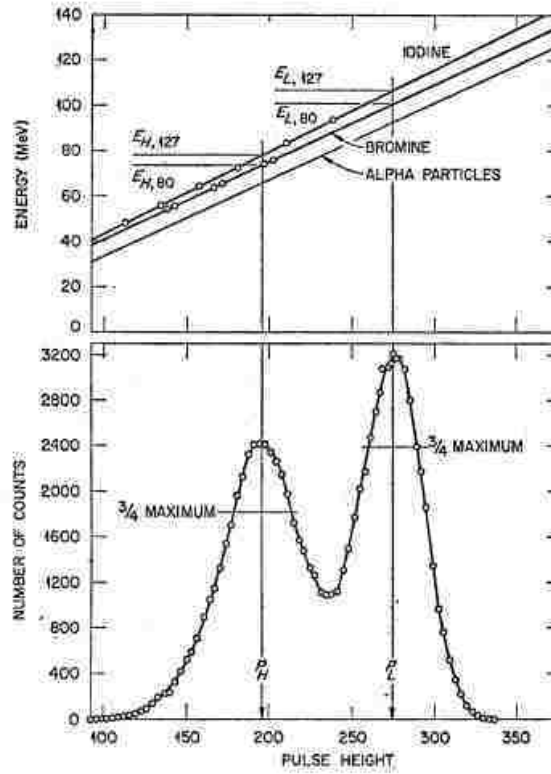
Figure 42: ^{252}Cf Calibration of solid-state detectors for heavy ions and fission fragments using ^{80}Br and ^{127}I, from Schmitt et al.   (Schmitt, Kiker and Williams 1965).

The Si detector we used a passively implanted planar silicon (PIPS), to look at energies

associated with fission fragments. Our ^{252}Cf source is slightly modified by a 100 µg/cm2

layer of Au to prevent source leakage, while Schmitt et al. used a source prepared by the self-transfer method.

6.2.1   Parameters to Use Schmitt Calibration

To use this Schmitt method of calibration, certain parameters must be met, shown in Figure 43, a comparison to data taken is shown in chapter 7.3.2.3 (Knoll 2010). Additional parameters are described in the Schmitt et al. paper.

Spectrum Parameter	Expected Value
N_L/N_V	~2.9
N_H/N_V	~2.2
N_L/N_H	~1.30
ΔL	~0.36
$\dfrac{(L-H)}{\Delta H}$	~≤0.44
$\dfrac{(L-H)}{(H-HS)}$	~≤0.69
$\dfrac{(L-H)}{(LS-L)}$	~≤0.48
$\dfrac{(L-H)}{(LS-HS)}$	~2.17
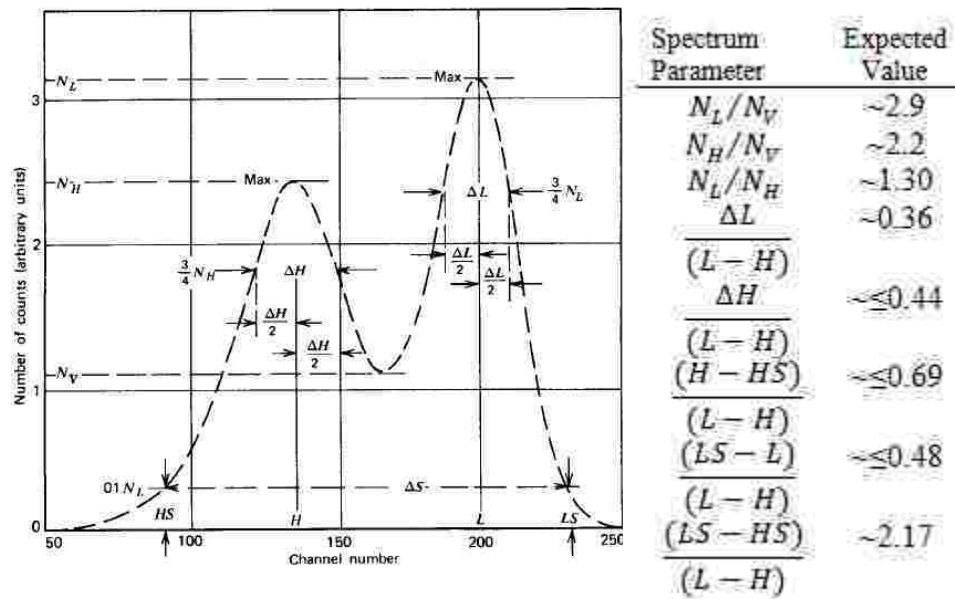
Figure 43: Spectrum parameters for ^{252}Cf for solid-state detectors for the Schmitt method, from G. F. Knoll (Knoll 2010).

6.2.2 Modifications to the Schmitt Constants

Weissenberger et al. performed an experiment at the Lohengrin mass separator to validate Schmitt et al. constants to convert the original channel spectrum to an energy spectrum (Weissenberger, et al. 1986). These updated values are listed below.

$$a = {24.3}/{(P_L - P_H)},$$

$$a' = {0.0283}/{(P_L - P_H)},$$

$$b = 90.397 - aP_L,$$

$$b' = 0.1150 - a'P_L.$$

Where P_L and P_H are the channel numbers of the centroids of the light and heavy peaks, respectively, following as with the work by Schmitt et al. These updated constants are what we will use in the section on energy loss.

7   Energy Loss Measurements and Simulations

We are concerned with fission fragment energy loss and energy broadening in the spectrometer as it affects the measurement resolution. Fission products were simulated and measured. As there is a broad range of fission fragment species, it is difficult to perform clear measurement of energy loss directly on these, and so alpha particles were also simulated and measured in many parts of this work.

7.1   Energy Loss Measurement Set-up

The energy loss was measured by using a radioactive source, a PIPS detector, and the foil being characterize placed between them, as in Figure 44. This was all operated within a vacuum chamber to reduce energy loss to air. Details of the detector, sources, foils, and vacuum chambers are presented below.
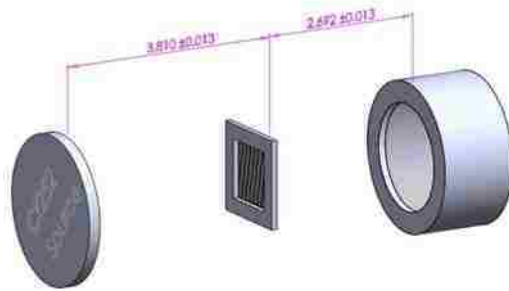
Figure 44: Detector, foil, and source basic set-up.

7.1.1 Passivated Implanted Planar Silicon (PIPS) detector

The PIPS detector is made to replace the silicon surface barrier detector and diffused junction detector. A silicon surface barrier detector is a type of a semiconductor detector; it measures the effect of an incident charged particle on ionization within the solid material which is under bias. The silicon is doped with impurity atoms to form a p-n junction. With a reverse bias voltage applied, this is a depletion region. In the depletion region, there are no free charge carriers, the particle that enters loses energy by creating electron-hole pairs in this region (Knoll 2010).

The radiation is measured by the amount of charge carriers that are freed in the detector material set between two electrodes. As a particle enters the material with a certain energy, a proportional number of electron-hole pairs are created. In Si, the average energy to create an electron-hole pair is 3 eV. Under the influence of the electric field, the electron-hole pairs travel to the electrodes and the motion is measured as a pulse. The number of electron hole pairs is proportional to the amount of energy deposited.

7.1.2 Sources

There are three sources that we used in the analysis of energy loss from alphas; a 0.0318 µCi TriNuc source which consists of ^{239}Pu, ^{241}Am, and ^{244}Cm, 1.67 Ci ^{239}Pu source, and a 1 Ci ^{252}Cf source, which is decayed down in approximately 0.5 µCi. When measured with no foil the FWHM of single energy alphas of the TriNuc, ^{239}Pu, and ^{252}Cf are 16.5, 42.4, and 28.3 keV respectively. The sharper peaks of the TriNuc source were a benefit

but the source intensity made it less useable. The ^{252}Cf was used for fission fragment energy loss, as it is the only fission source.

7.1.3 Measurement Chambers

Three different chambers were used for measurements based on their benefits. For example, though the ConFlat setup had the best vacuum, it required unbolting and re-bolting 20 bolts each time for access to the chamber. Specification of the chambers are described below

7.1.3.1 NIM Based 7401 Alpha Spectrometer

To confirm the previous add back method, a Canberra A-450-20-Am 24008 PIPS detector was used, which is optimized for alpha particles (Canberra 2012). Initially a TriNuc source of ^{239}Pu, ^{241}Am, and ^{244}Cm was tested to confirm the thickness of the carbon foils against the SRIM measurements. This was run in a NIM based 7401 alpha spectrometer, shown in Figure 45, shown with an electronics block diagram. A schematic of the measurement is shown in Figure 44. The experimental set-up starts first running by an 'empty' chamber, this entails the TriNuc source on a sample slide and a slide that will eventually hold the carbon foils in place above the source, all this below the PIPS detector at the top. This 'empty' set-up is then pumped down to 100 µHg (0.1 torr) and is run for five minutes. Then an iteration of different foil thicknesses is placed in the slide above the source and run at the same conditions. The block diagram of the electronics is

shown in Figure 45. In Table 9 the different energies and intensities of the TriNuc source are listed.

Table 9: Tri-nuclide alpha energies and intensity (NNDC; Brookhaven National Laboratory 2017)

Isotope	Energy (keV)	Intensity (%)
^{239}Pu	5156.59	70.77
	5144.3	17.11
	5105.5	11.94
^{241}Am	5485.56	84.8
	5442.8	13.1
^{244}Cm	5804.77	76.9
	5762.64	23.1
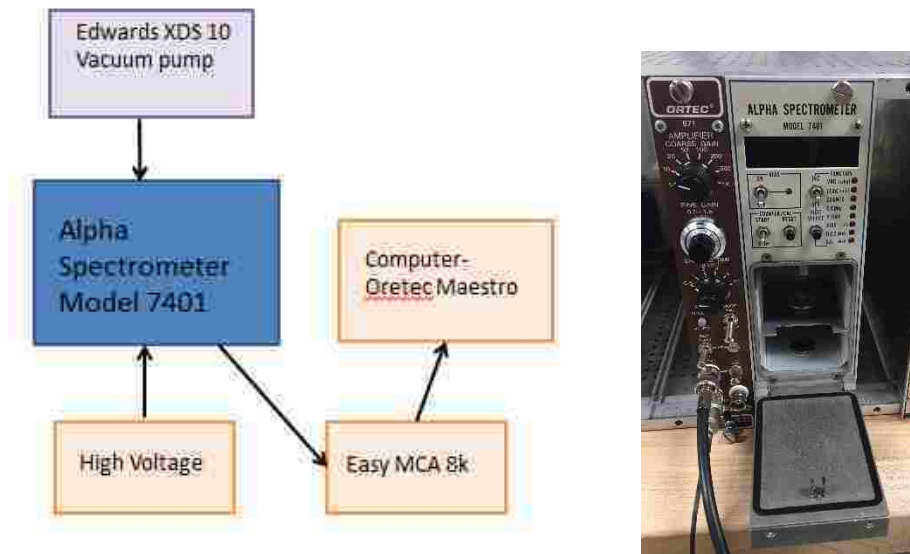
Figure 45: Block diagram of alpha energy loss experiment (left) and Alpha Spectrometer Model 7401(right).

7.1.3.2   Ortec 808

To look at fission fragment energy add-back the same chamber cannot be used. The

model 7401 detector is optimized for alphas, as it rejects signals greater than 10 V, which

is where the detector pulses fall for fission fragments. Energy loss experiments were run

in an EG&G Ortec 808 vacuum chamber, with the same PIPS detector but with no

internal amplifier. The distances between the source, foil, and detector are described in

Figure 46. With a ^{252}Cf source in place, the chamber was pumped down to a vacuum of

12 mbar (10 torr) and then run for 3 hours to collect data, the electronics used are the

same as in Figure 47, with an Ortec 808 chamber instead of the ConFlat. This chamber

failed to keep a steady pressure with a proper gauge and the results should consider this.

7.1.3.3   ConFlat Chamber for Fission Fragments

When it was found that air was a significant source of energy loss, another set-up was

constructed. An 8-inch ConFlat 50 cm long tube was assembled to have the same

distance between the source, carbon foils, and detector as the EG&G Ortec 808.The

distances between the source, foil, and detector are described in Figure 46. The ConFlat

tube and physical setup is shown in Figure 47. The components are described in the

following block diagram, Figure 48. The ConFlat chamber was pumped down to 0.22

mbar and runs were taken for ~19 hours (70,000 s). All runs were repeated from the

Ortec 808 in the ConFlat chamber except for the 700 and 900 SiN runs.
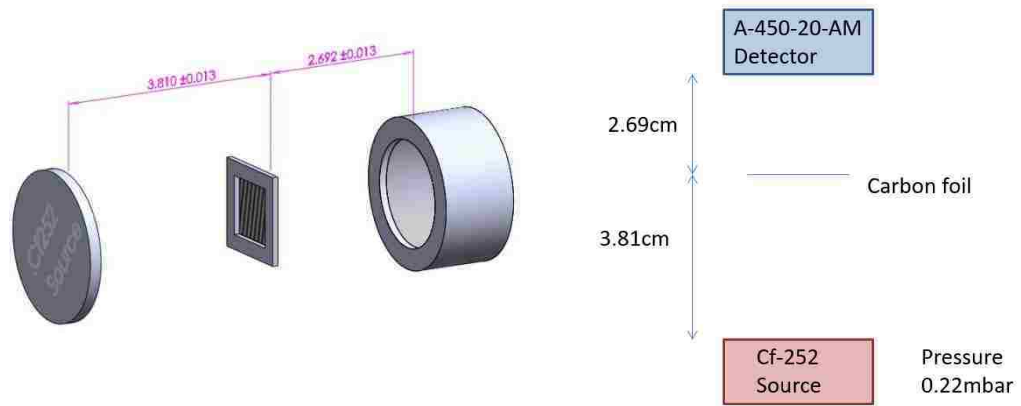
Figure 46: Schematic of the energy loss experimental set-up.

Figure 47: Energy Loss experimental set-up (Left) and pressure chamber (right).
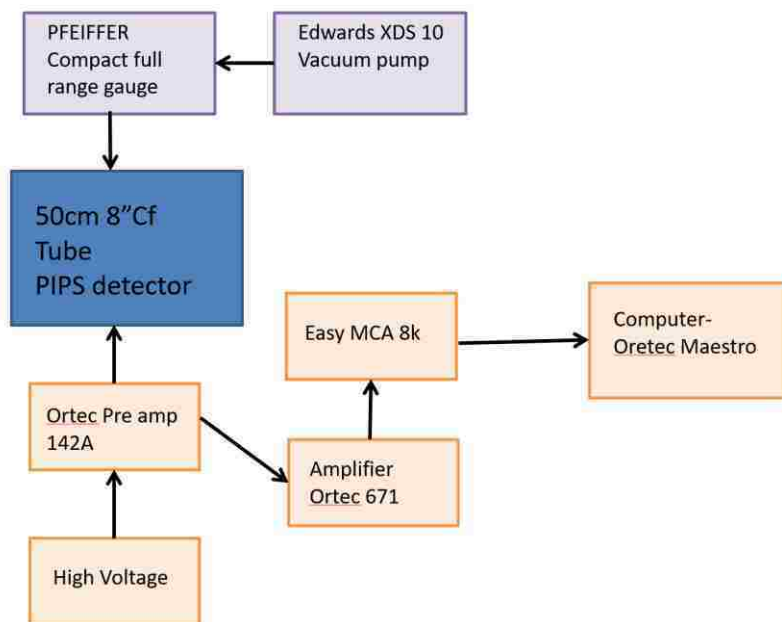
Figure 48: Block diagram of fission fragment energy loss experiment.

7.1.4 Foils and Windows

The different thicknesses of carbon foils used are labeled as: 21, 43, 55, 60, 64, 76, and

100 $\mu g/cm^2$. The foils were mounted on their frames by floating on top of a bath of

deionized water and then the aluminum frame scooped from under to position the foil

over the opening shown in Figure 49. The foils self-adhere to the frames. Some foils were

stacked to produce a thicker total, $64 + 21 = 85$ $\mu g/cm^2$ and $64 + 43 = 107$ $\mu g/cm^2$. It is

also noted that the foils used here for energy loss calculations were different than the

ones used in the previous TOF section, and each foil is labeled according to the slide that

it was cut from.

Figure 49: 43 $\mu g/cm^2$ carbon foil floated on frame (left) and bare aluminum frame (right).

The different thickness of silicon nitride used are 200 and 500 nm. These were also

stacked to produce thicker windows to measure energy loss; $500 + 200 = 700$ nm, $500 +$

$2(200) = 900$ nm. The SiN windows were far more fragile to stack on top of one another

than the carbon foils.

7.2 Simulations of Energy Loss

To understand the expectations of the energy loss measurements, SRIM and MCNP calculations were performed. SRIM and MCNP work well for alpha particles but results for fission fragments are not as reliable for SRIM, as mentioned in chapter 6.1, and reliability is not clear for MCNP, so these are more used for a general understanding. Using the calibration values given in Table 2 and known alpha energies, SRIM was run for each of the carbon foil thicknesses and SiN window. Visualization of a typical run is shown in Figure 50. Distances and pressures used are based on our experimental work, described in this thesis. As each particle left the simulation region, equivalent to passing through the air into the detector in the experiment, the remaining energy of each particle simulated was recorded. Analysis of this simulated data set allowed extraction of energy loss and straggling.
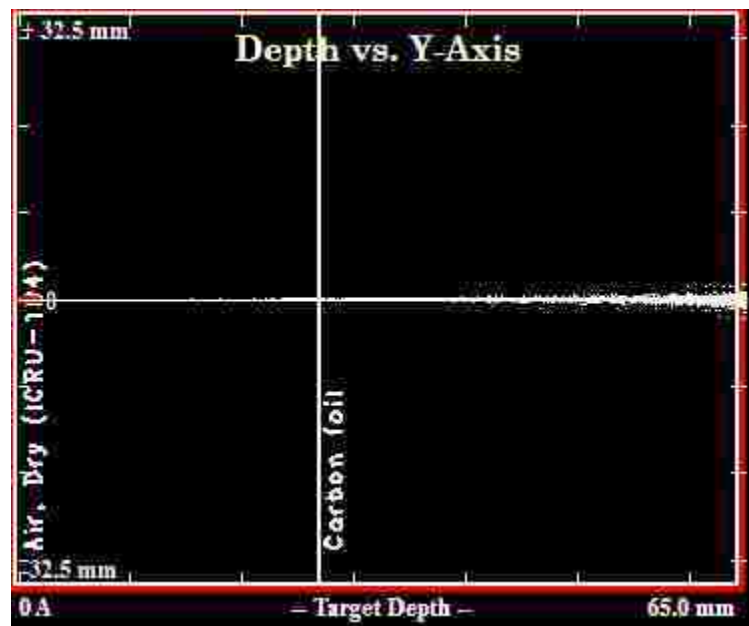
Figure 50: Visualization of a SRIM simulation using alpha particles. Air thicknesses are described in the text for MCNP. The carbon thickness is 20 µg/cm2. Lateral straggling is visible in this image. Information on energy loss and straggling is in the associated simulation results tables.

In MCNP the ^{252}Cf source was examined using just an average heavy and light fragment, ^{141}Cs with an energy of 79.37 MeV and ^{106}Mo with an energy of 103.77 MeV, respectively. These two projectiles were modeled as mono-directional, monoenergetic, pencil beam sources. The simulated ^{252}Cf source had 100 $\mu g/cm^2$ of gold set directly over the active region to more closely approximate the true source. In the experiments, the alpha particles then travelled through 3.81 cm of air, a carbon foil of chosen thickness, another 2.69 cm of air, then into the detector. The detector specifications are given as 50 nm of Si equivalent followed by 20 mm of Si in the depletion region, which is the active detection volume. By using a modified F4 tally, the energy deposited in each region is recorded. The MCNP code was written by fellow student Phoenix Baldez.

7.3   Results

7.3.1   Alpha Results

As described in the method for alpha energy loss the TriNuc source was first to be measured to verify that the PIPS detector was working correctly and that we would be able to compare with SRIM data. For no foil and at 100 µHg (0.1 torr) pressure a spectrum of each alpha source is taken with the 7401 alpha spectrometer. The TriNuc source gives the best resolution with a FWHM of 16.5 keV, shown in Figure 51.
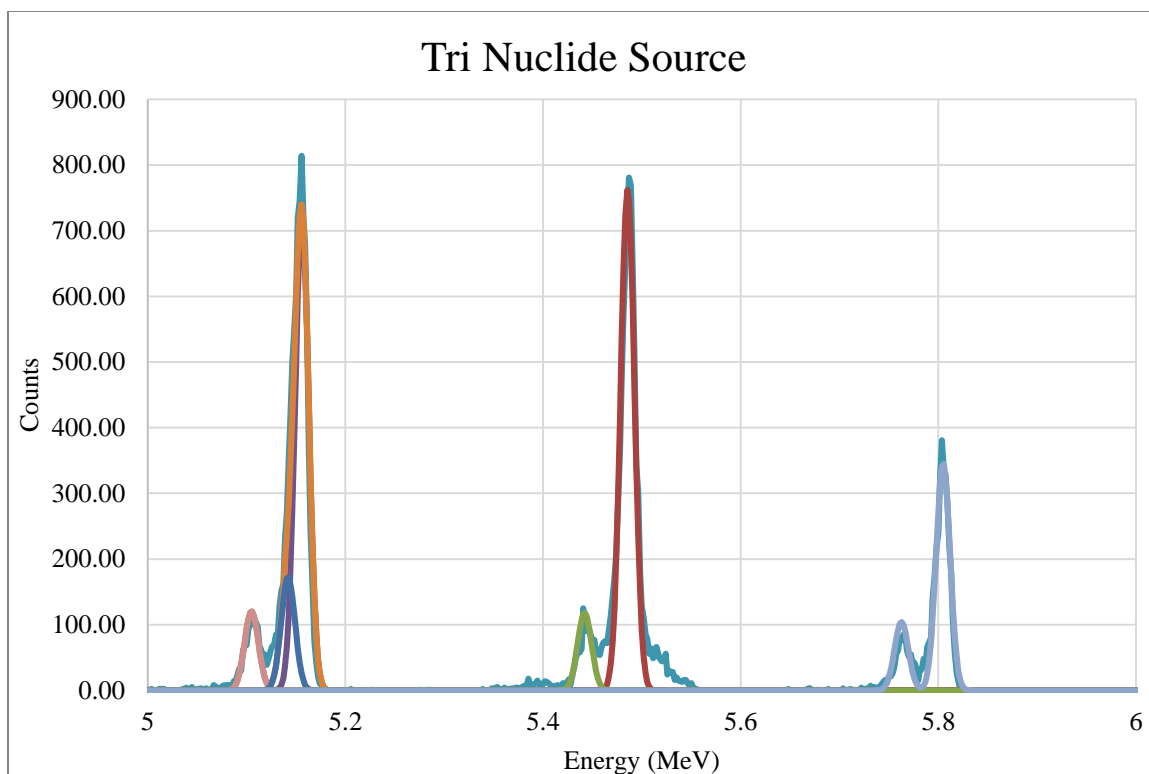
Figure 51:TriNuc alpha spectrum run in the 7401 alpha spectrometer at 100 µHg (0.1 torr). FWHM of 16.5 keV.

The ^{239}Pu source was run under the same conditions and has a larger FWHM at 42.4 keV displayed in Figure 52. This could be due to a thicker layer of the active material or layers or dust, oils or other contaminates have covered the surface over the years. This is important for analysis of the TOF broadening.
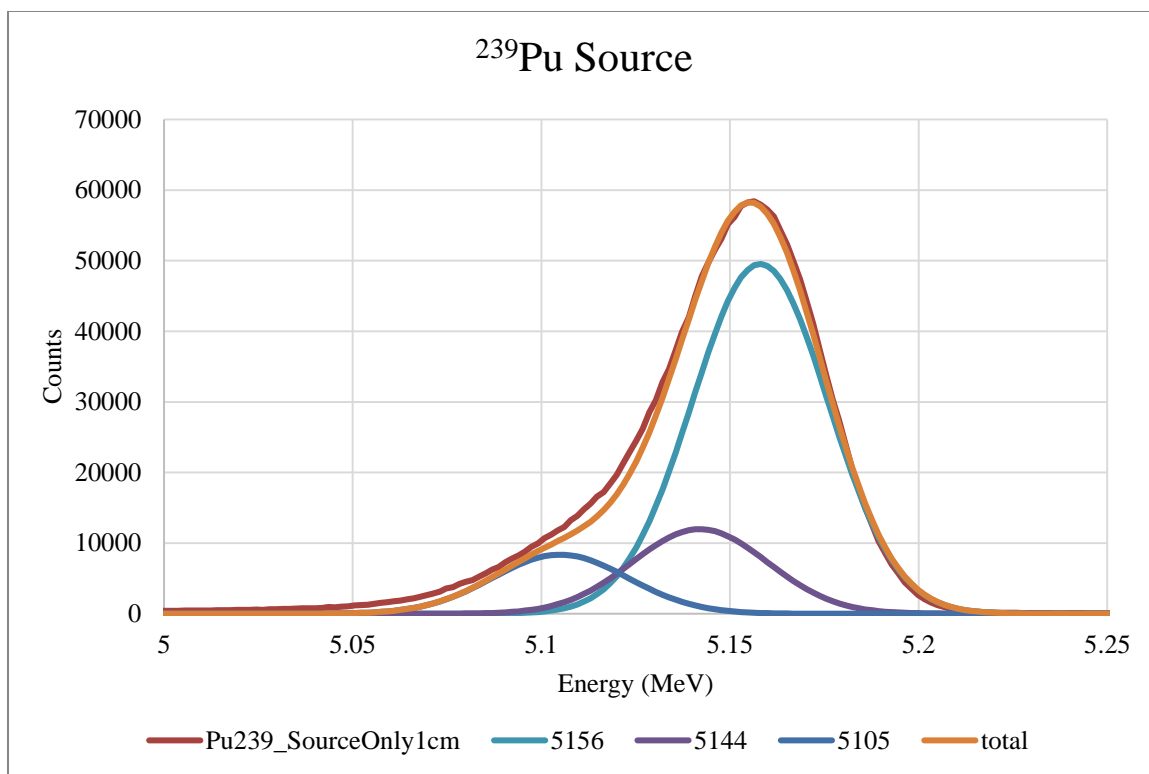
Figure 52: ²³⁹Pu alpha spectrum run in the 7401 alpha spectrometer at 100 μHg (0.1 torr). FWHM of 42.4 keV.

The ^{252}Cf source was run with the same conditions for alpha measurements. The energy spectrum is shown in Figure 53, with a FWHM of 28.3 keV, there is also a larger down scatter at lower energies from the peak consistent with the source having a $100 \ \mu g/cm^2$ gold layer. It is important that these were all ran at the same pressure for energy broadening of the source discussed in chapter 8.1.
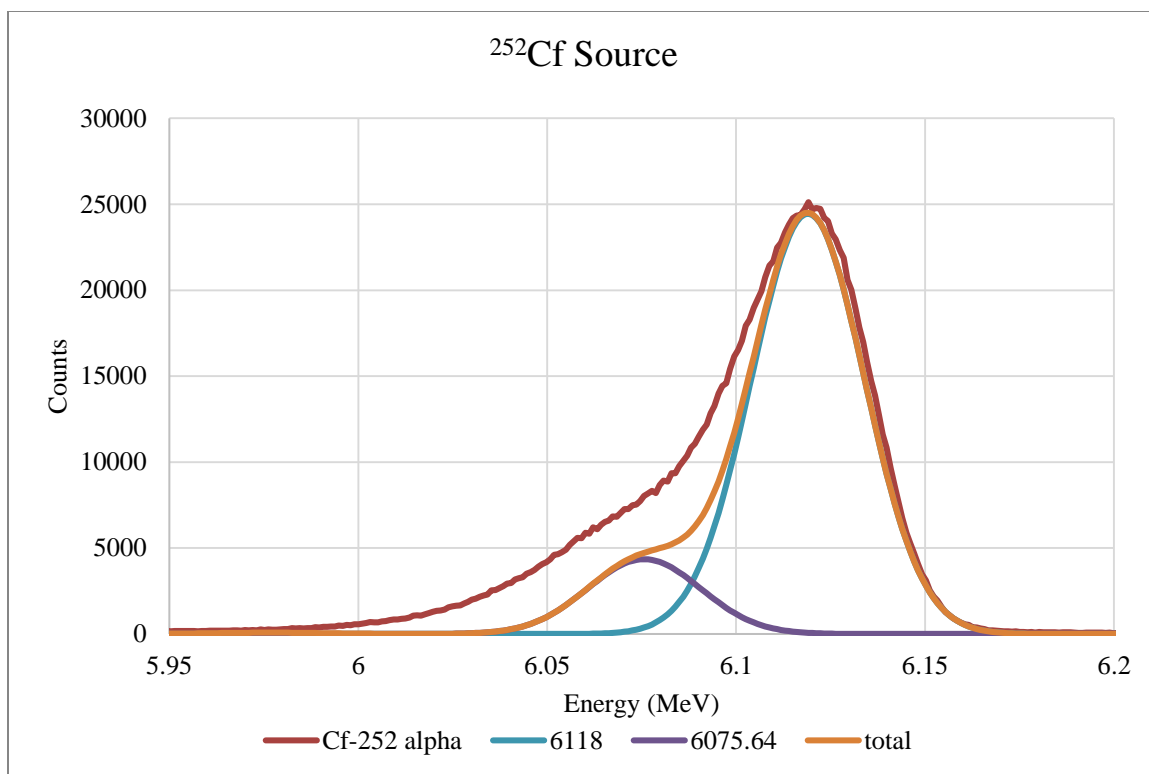
Figure 53: ²⁵²Cf source alpha spectrum run in the 7401 alpha spectrometer at 100 µHg (0.1 torr). FWHM of 28.3 keV.

7.3.1.1 Carbon Foils

7.3.1.1.1 TriNuc Source

A source only (empty) alpha particle measurement was taken using the TriNuc source and the spectrum linearly calibrated on the lowest peak (^{239}Pu) at 5.156 MeV and the highest peak (^{244}Cm) at 5.8048 MeV shown in Figure 51. This calibration from the source only run is used on all the runs to see the energy lost.

SRIM calculations were performed to determine the expected energy loss through several carbon foils, using the listed thicknesses. This was done using the dominant peak from

each of the three nuclides in the source, ^{239}Pu, ^{241}Am, and ^{244}Cm, at 5.156, 5.485, and

5.804 MeV. The actual energies through the foils and thus the energy losses were

measured through these foils. The experimental values and SRIM values are compared in

Table 10 and Figure 54.

As shown in Figure 54 there is a slight difference in SRIM simulations vs experimental

data. From SRIM there have been numerous experiments to validate the stopping power

accuracy, theory and experimental agree to better than 10% as discussed in the theory

chapter 6.1.1 (Ziegler 1999), but this doesn't explain the full range of differences seen.

Each peak is fit with the appropriate intensity of the alpha particle for each nuclide listed

in Table 10. The energy loss of the major peak is calculated for the different thicknesses

of foils listed and shown in Figure 54 and Table 10, both compared to SRIM values.

Figure 54 also shows a foil that was labeled 60 $\mu g/cm^2$, discussed below.

Table 10: Alpha energy loss of SRIM and Experimental (keV) of the TriNuc source.

C foil density (µg/cm²)	SRIM ^{239}Pu (keV)	SRIM ^{241}Am (keV)	SRIM ^{244}Cm (keV)	Exp. ^{239}Pu (keV)	Exp. ^{241}Am (keV)	Exp. ^{244}Cm (keV)
21.00	17.01	16.25	15.62	17.36	17.12	15.80
43.00	34.52	33.06	31.72	30.49	29.25	29.08
64.00	51.12	48.89	46.98	47.84	47.33	44.09
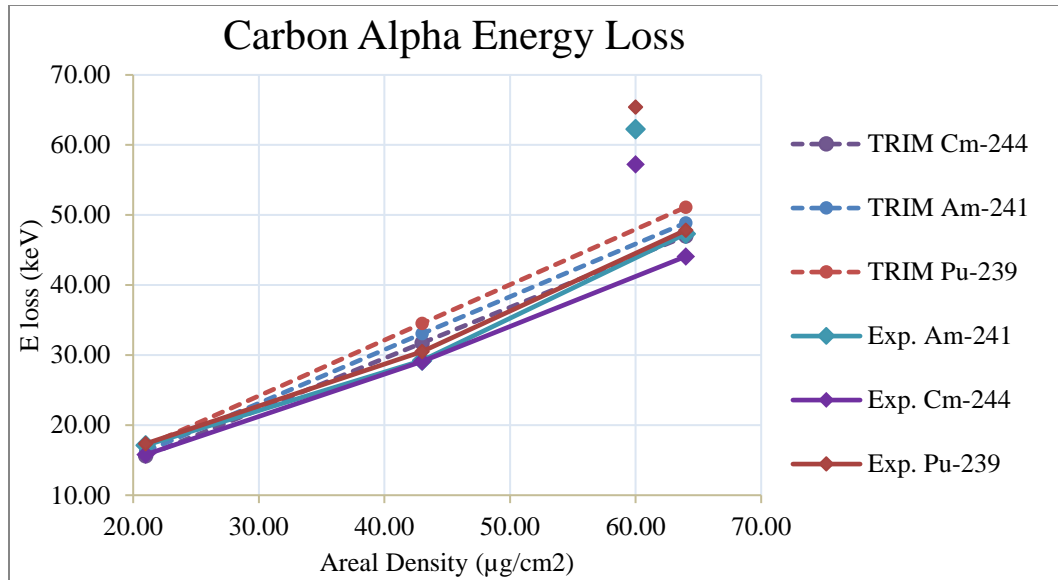
Figure 54: TriNuc alpha energy loss in different thicknesses of carbon foils.

In Figure 54 you can see the vast difference in the experimental values from a 60 to 64 $\mu g/cm^2$ carbon foil, and a small expected change in the SRIM results. The percent difference of the experimental and SRIM value are ~25% for the 60 $\mu g/cm^2$, and ~5% for the 64 $\mu g/cm^2$. This has led us to believe that the 60 $\mu g/cm^2$ is labeled incorrectly, by using the linear relation from the SRIM values the thickness was determined to be 80.6 $\mu g/cm^2$. This may be an important tool to double check the thicknesses of the foils that we receive.

7.3.1.1.2 ^{239}Pu Source

Used in the time-of-flight calculations we compare SRIM, MCNP, and Experimental Energy Loss from a ^{239}Pu source. In Figure 52 is the ^{239}Pu spectrum fit with different peaks depending on the intensity of each alpha.

Energy loss after passing through one foil is important to calculate the time-of-flight. The energy left after alphas pass through 20, 55, and 100 $\mu g/cm^2$ foils are shown in Table 11, it is displayed in this manner instead of energy loss to calculate TOF in chapter 4, 5, and 8. Only values from SRIM were used in calculations for time-of-flight in chapter 4 and 5.

Table 11: Summary of SRIM, MNCP, and Experimental energy loss of alphas through carbon foils.

Energy (MeV)	Thickness ($\mu g/cm^2$)	SRIM Energy Left (MeV)	SRIM σ	MCNP Energy Left (MeV)	Experimental (MeV)	Experimental σ
5.156	20	5.140	0.003	5.142	5.130	0.019
5.156	55	5.112	0.004	5.117	N/A	N/A
5.156	100	5.077	0.006	5.085	5.052	0.023
5.144	20	5.128	0.002	5.130	5.105	0.019
5.144	55	5.100	0.004	5.105	N/A	N/A
5.144	100	5.064	0.006	5.073	5.035	0.023
5.105	20	5.089	0.002	5.091	5.075	0.019
5.105	55	5.061	0.004	5.066	N/A	N/A
5.105	100	5.025	0.006	5.032	5.000	0.023

Each thickness of carbon was analyzed in SRIM and MCNP, using a PIPS detector only the 20, and 100 foils were measured as no 55 foils had been transferred to a 1cm x1cm testing square. The experimental set-up was the same as used for the TriNuc source, measurements were made with the 7401-alpha spectrometer chamber pumped down to a pressure of 100 µHg (0.1 torr). All calculations used in the analysis in chapter 4 and 5 use the SRIM values but it is interesting to note that MCNP shows less of an energy loss for each foil, and experimentally a substantial amount more. This is described further in chapter 8.

7.3.1.1.3 ^{252}Cf Source

^{252}Cf has an alpha at 6.118 MeV (81.4%). By measuring the energy loss and comparing that value to SRIM calculations we can verify the thickness of each carbon foil without having to run a separate test with the TriNuc source. As you will notice in the Table 12, the 76 $\mu g/cm^2$ foil is losing less energy than expected, which lends us to believe that it is mislabeled and thinner. Figure 55 shows the ^{252}Cf alpha spectrum of the source (red) and after passing through a 21 µg/cm^2 carbon foil (blue).
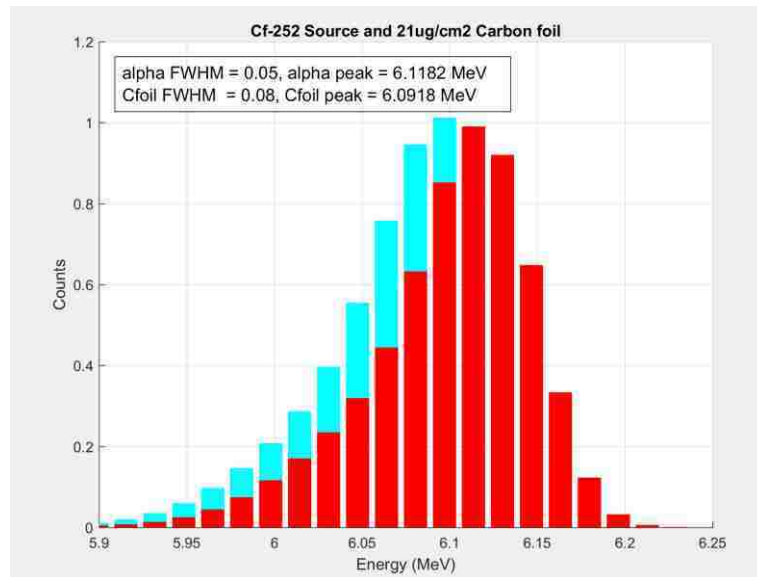
Figure 55: ^{252}Cf 6.118 MeV alpha peak (red) with a 21 µg/cm^2 alpha spectrum (blue).

For every run done for ^{252}Cf fission fragments the 6.118 MeV alpha energy loss was also noted and is shown in Figure 56. A linear fit was plotted to the SRIM results and extracted thickness depending on the energy loss is given in the following Table 12. All

the carbon foils, except that labeled 76 $\mu g/cm^2$ were used in the fission fragment energy loss calculations.
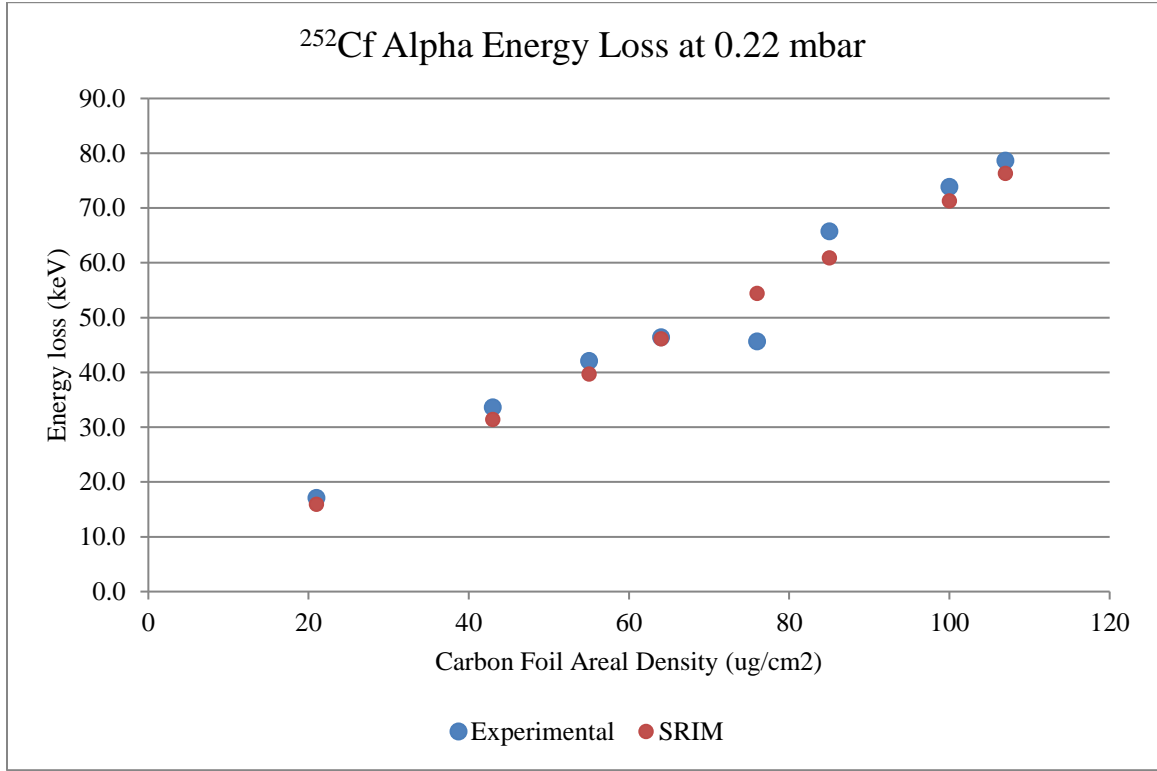
Figure 56: A comparison of SRIM calculated and experimentally determined ^{252}Cf 6.118 MeV alpha energy loss through carbon foils (keV).

Table 12: Measured thicknesses of Carbon foils compared with the labeled thicknesses.

Given thickness μg /cm²	21	43	55	64	76	85	100	107
Extracted thickness μg /cm²	22.6	46.2	58.3	64.4	63.3	91.9	103.6	110.3

7.3.1.2   SiN Windows

Alpha energy loss in the silicon nitride (SiN) windows was only performed for the same set-up as for fission fragment energy loss, all using the [252]Cf source. The SiN windows are composed of a manufacturing secret proportionality of silicon and nitrogen, so the commonly used proportionality of 3:4 was used for simulations, for Si_3N_4 though we write simply SiN. The energy loss through SiN is compared between SRIM and experiment in Figure 57. Though SRIM matched experimental values quite well for the TriNuc, [239]Pu, and [252]Cf alpha source through carbon, SRIM overestimated the energy loss from alphas through SiN for both thickness here. This could easily be due to a mischaracterization of the elemental mix of SiN which would change the mass thickness.
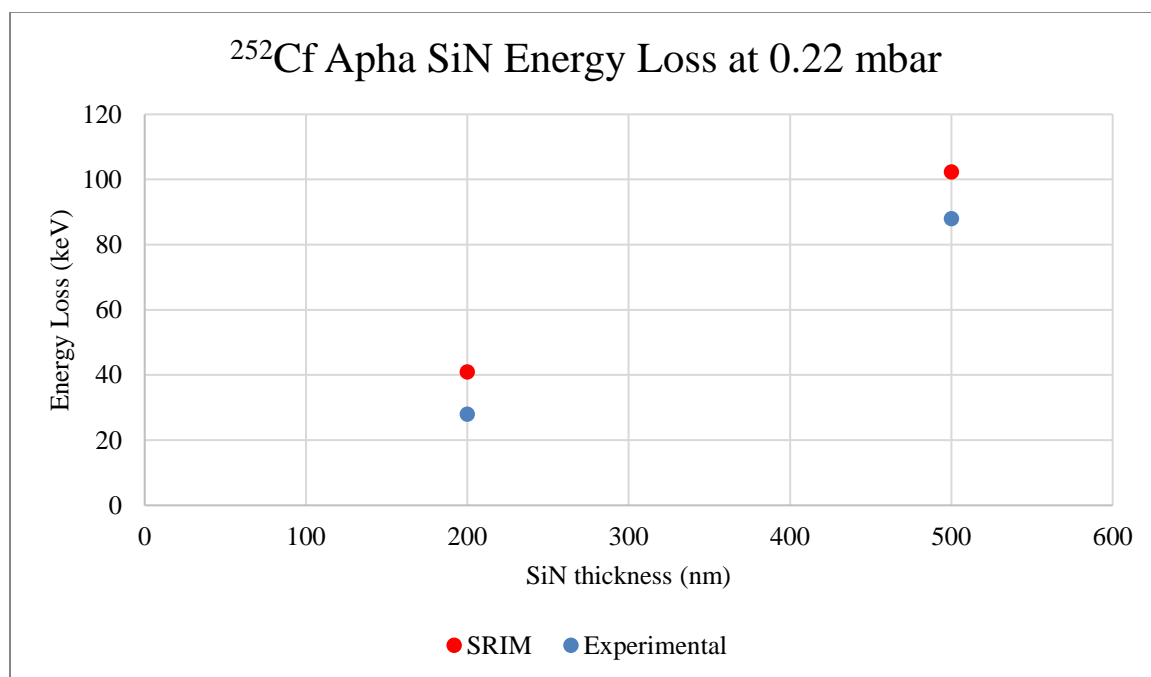
Figure 57: A comparison of SRIM calculated and experimentally determined [252]Cf 6.118 MeV alpha energy loss through SiN windows (keV).

7.3.2　Fission Fragment Results

7.3.2.1　Pulse Height Defect

The ^{252}Cf alphas and fission fragments were measured in the ConFlat setup with no foil between the source and PIPS detector to understand the pulse height defect (PHD) seen in the PIPS. Calibrating using the ^{252}Cf alpha energy and assuming channel 0 corresponds with 0 energy results in the straight line shown in the top graph of the Figure 58. The known energies of the ^{252}Cf fission spectrum are 68.22 MeV and 95.41 MeV for the heavy and light peaks, respectively, and these are plotted vs. the measured peak channels in Figure 58. We estimated a pulse height of 92% of a perfect pulse height for light and 86% for heavy. Using the method described in Wilkins et al. (Wilkins, et al. 1971) to correct for the PHD the energy losses deviated from the true values by less than 2.5% or 1.83 MeV. Examining the method described in Forgue et al. (Forgue and Kahn 1967) to correct the pulse height defect the resulting energy is within 1 MeV of the true value. Forgue et al. and Wilkin et al. have described a 40 μg/cm^2 gold detector window energy loss as 0.6 MeV for both the heavy and light fragments. From the MCNP simulations show that 0.59 MeV for light fragments and 0.68 MeV for heavy fragments energy loss through the 50 nm Si equivalent detector window. The MCNP only shows the total energy deposited in the detector, with no differentiation of energy deposited by ionization or non-ionization.

Since the Schmitt method is a valid calibration method there is no need to use the alpha calibration and the addition of the PHD. The Schmitt calibration method agrees within 1 MeV with a method based on an alpha-calibration line after a PHD correction.
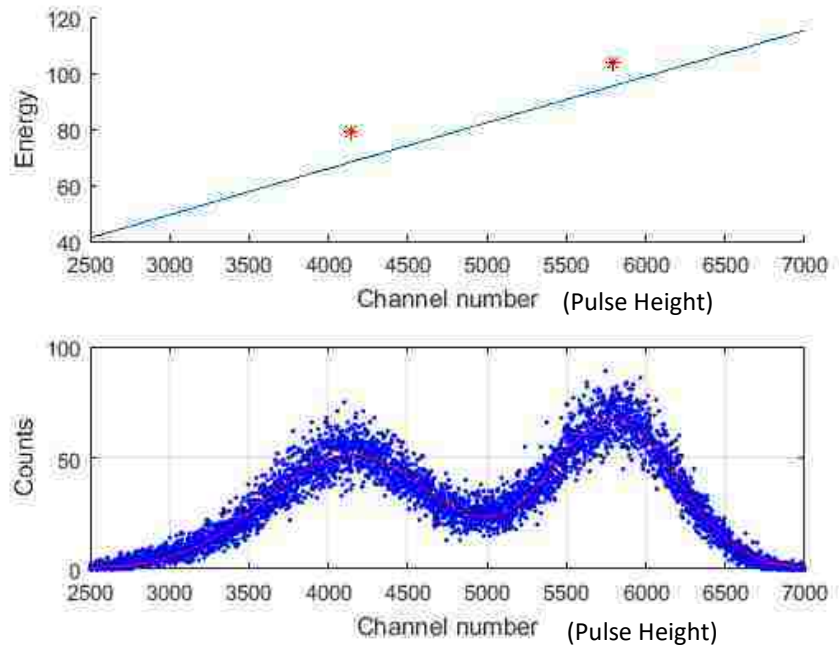
Figure 58: Alpha calibration of light and heavy peak without the addition of PHD calibrated on 6.118 MeV and zero (blue line) published values for light and heavy energy peaks of ^{252}Cf.

7.3.2.2   Mass Independent Calibration of Data

The energy spectrum of the ^{252}Cf source, in terms of channel, is shown in Figure 59. Using the heavy peak at channel 4120 and the light peak at channel 5741, with the known peak energies, a linear calibration equation is found: E=0.015*Ch + 17.350 with the energy, E, in MeV and Ch being the channel number. This mass independent calibration is straight forward analysis of the data and is used to compare with the mass dependent

calibration following the method of Schmitt et al. (Schmitt, Kiker and Williams 1965) and Weissenberger (Weissenberger, et al. 1986).
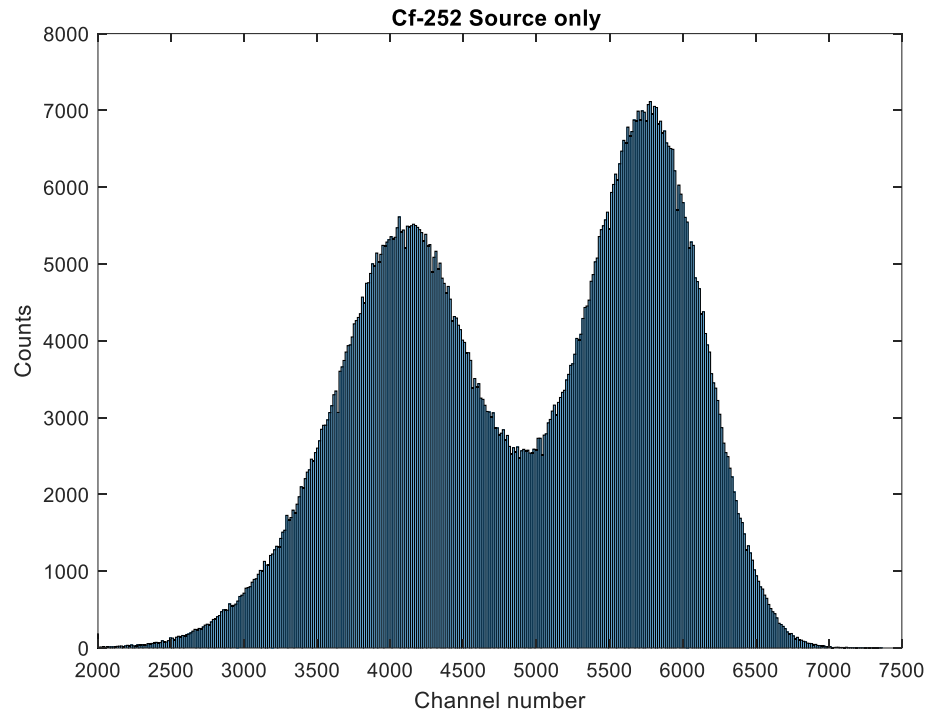
Figure 59: ^{252}Cf fission spectrum.

The ^{252}Cf source has a 100 μg/cm^2 gold foil in front to prevent shedding of source material. It is acknowledged that this affects the energy that leaves the source. The peaks without foil slowing are expected to be 103.77 and 79.37 MeV for the light and heavy peaks, respectively. With the gold foil, these become 102.10 and 77.65 MeV, respectively. As this is a small effect it should have make only a small change to the mass independent linear calibration. The mass dependent calibration, next section, uses parameters found from uncoated sources and thus should give the true energies from the pulse heights.

7.3.2.3 Schmitt Mass Dependent Calibration of data

To use the Schmitt method for extracting the mass dependent PHD from a Si detector the spectrum must be near some spectrum parameters. These are listed in Table 13 as the valid values, alongside the experimentally derived values for our ^{252}Cf fission spectrum. These are close enough to be considered a match and thus the Schmitt method is used.

Table 13: Schmitt calibration spectrum parameter values.

Spectrum Parameter	Expected Value	Experimental Value
N_L/N_V	~2.9	2.864
N_H/N_V	~2.2	2.195
N_L/N_H	~1.30	1.304
$\Delta L/(L-H)$	~0.36	0.3702
$\Delta H/(L-H)$	~$\leq$0.44	0.444
$(H-HS)/(L-H)$	~$\leq$0.69	0.690
$(LS-L)/(L-H)$	~$\leq$0.484	0.480
$(LS-HS)/(L-H)$	~2.17	2.171

To convert the channel number to energy the constants found in Weissenberger et al. are used, repeated here, for the Schmitt equation E= (a + a'M)x + b + b'M,

$$a = {24.3}/{(P_L - P_H)},$$

$$a' = {0.0283}/{(P_L - P_H)} \, ,$$

$$b = 90.397 - aP_L \, ,$$

$$b' = 0.1150 - a'P_L \, .$$

As stated in chapter 6.2 it is acceptable to use a linear dependence of pulse height on fragment mass, a method used in Hakim et al., Muller et al., and Benetti et al., hence the single order of M in the Schmitt equation (Hakim and Shafrir 1971) (Muller and Gonnenwein 1971) (Benetti, et al. 2002).

7.3.2.4   Comparison of Linear Calibration and Schmitt Calibration

The mass dependence of the calibration can be assessed by examining the difference between the results using mass independent and mass dependent calibrations. If we compare the difference between the linearly calibrated values (diamonds) to the Schmitt values (squares) in Figure 60, with the linear calibration we see less of an energy loss for heavy fragments and more energy loss for light fragments. When thinner carbon foils are used the differences between the energy losses between the linear and mass dependent calibrated data decrease.
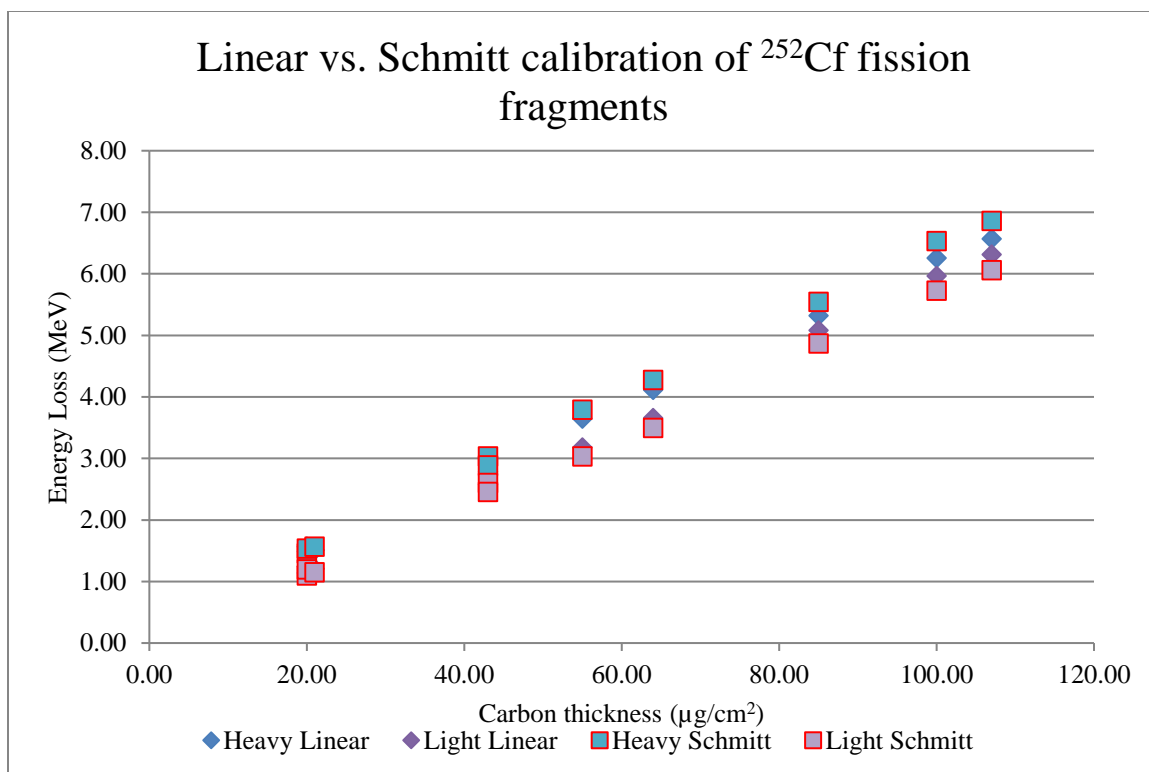
Figure 60: Linear (diamonds) vs. Schmitt calibration (square) in terms of energy loss (MeV).

While both methods give values for energy loss that are close to one another, no other

fission fragment energy loss papers have been found that use a linear calibration while

the three papers found on fission fragment energy loss: Hakim et al., Muller et al., and

Benetti et al., (Hakim and Shafrir 1971) (Muller and Gonnenwein 1971) (Benetti, et al.

2002). All have used a linear dependence of pulse height on fragment mass (Hakim and

Shafrir 1971). For the sake of comparing data where the same analysis methods are

performed, the following sections use the Schmitt calibration.

7.3.2.5   Fission Fragment Energy Loss Results

Fission fragment energy loss through carbon foils and through SiN was simulated with both SRIM and MCNP and compared with experiment using the Schmitt PHD correction, see Figure 61 and Figure 62. Similar to work summarized in Knyazheva et al. (Knyazheva, et al. 2006), we found that SRIM gave a much lower estimate of energy loss for carbon foils than what our experiment results produced. Interestingly SRIM overestimated on the energy loss through the SiN window, this could be because the SiN window has more components than Si and N, or different proportionality, while the 3:4 proportionality assumed for Si_3N_4 is what was run in SRIM.

The carbon foils were measured using an air pressure of 0.22 mbar, and SRIM and MCNP calculations use this pressure. For SiN two different air pressures were used, 0.22 mbar and 12 mbar, as discussed previously. The 12 mbar measurements were performed for SiN thicknesses of 200, 500, 700, and 900 nm. The 0.22 mbar measurements were performed for only SiN thicknesses of 200 and 500 nm. Simulations were performed for both 0.22 and 12 mbar pressures for SiN, but the differences were small (~3%) to not depict them in Figure 62 for a slightly simplified graph.
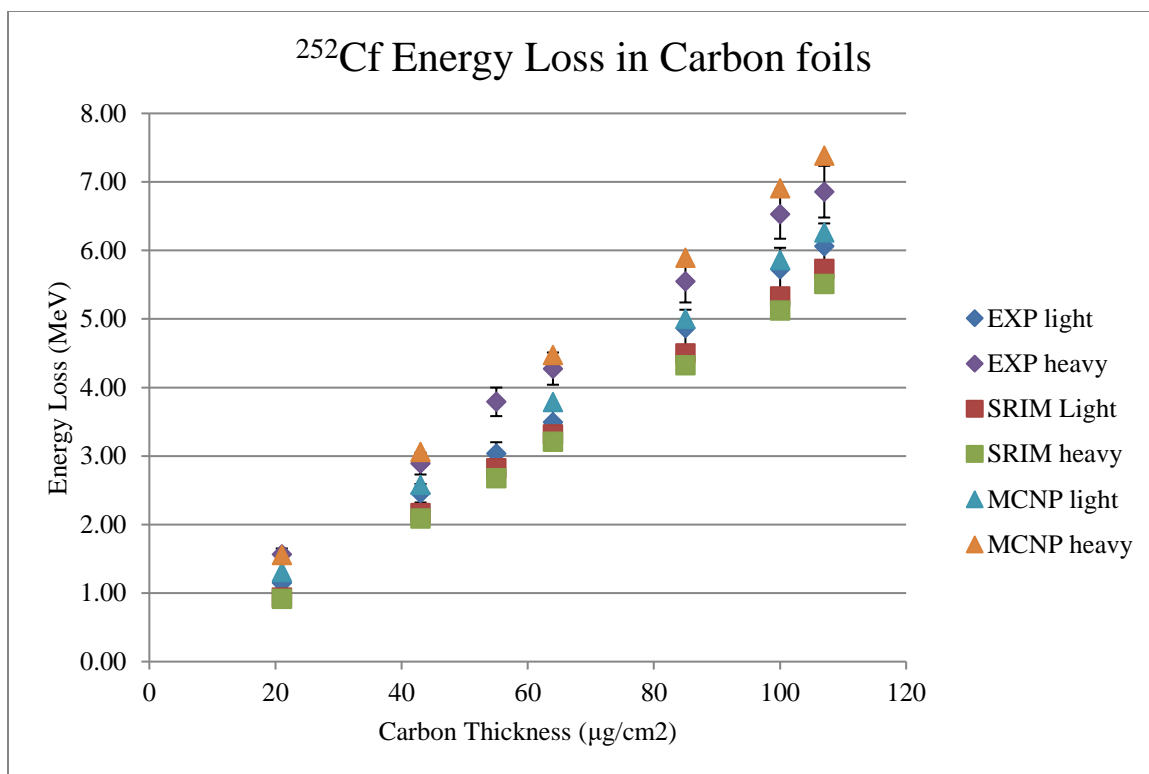
Figure 61: Energy loss in carbon foils at 0.22 mbar using Schmitt calibration method, SRIM, and MCNP.
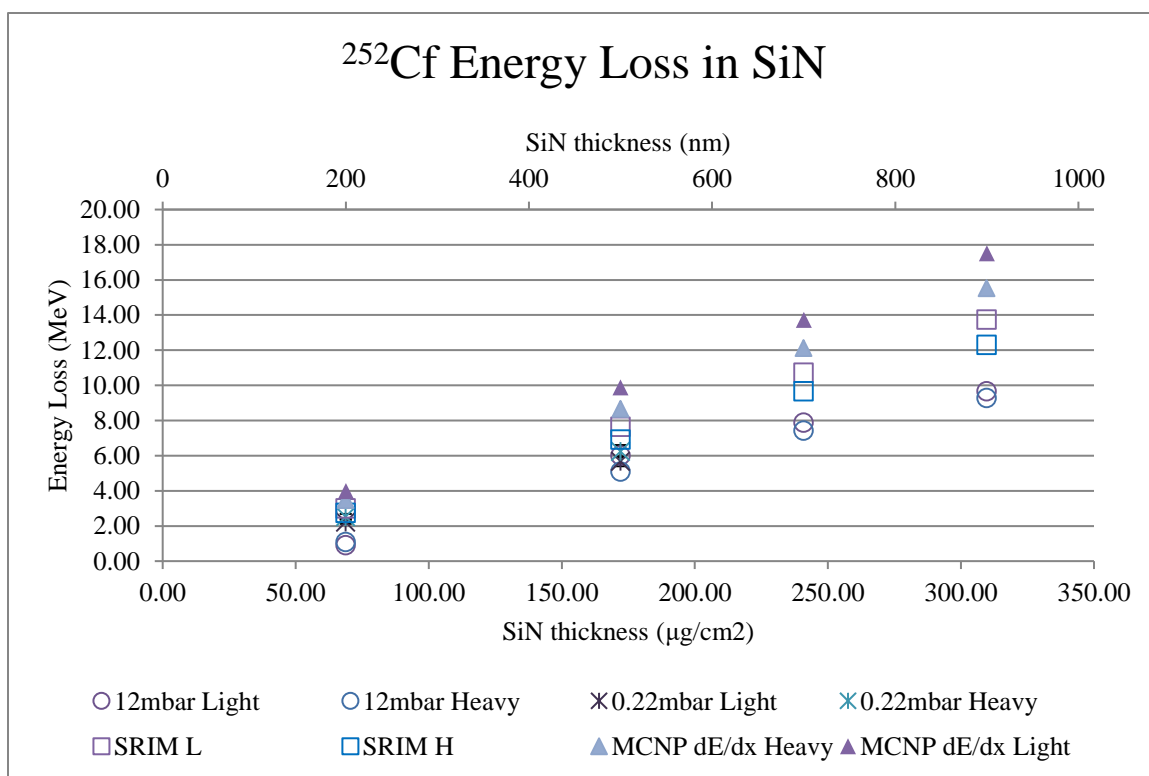
Figure 62: Energy loss in SiN at 0.22 mbar and 12 mbar using Schmitt calibration method, SRIM, and MCNP.

7.3.2.6 *Stopping Power Results for Carbon Foils*

For a more recognizable representation of the data we used stopping power. This is

expressed using the change in energy and an assumption of the foil or window being thin

enough that dE/dx is uniform through the foil or window, as $\frac{dE}{dx}(E) = \frac{E_{hole} - E_{foil}}{t}$, where

E_{hole} is the incoming energy; the energy that would be seen through a hole in the foil, E_{foil}

the energy after passing through a foil, and t is the thickness of the foil. The notation is

used to be consistent with Knyazheva et al. Using this math, the data is presented in

Figure 63 and Figure 64, with points for the experimental, MCNP, and SRIM energy loss.
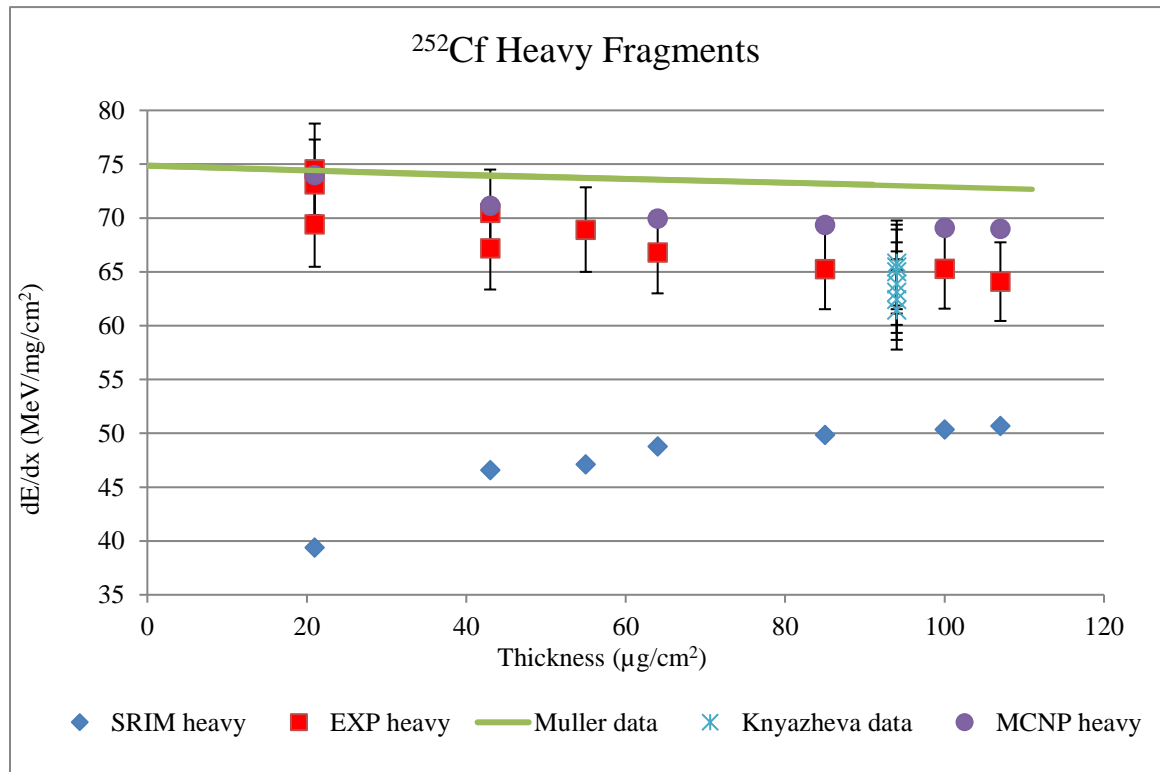
Figure 63: Stopping power of heavy fragments over different thickness of carbon foils.
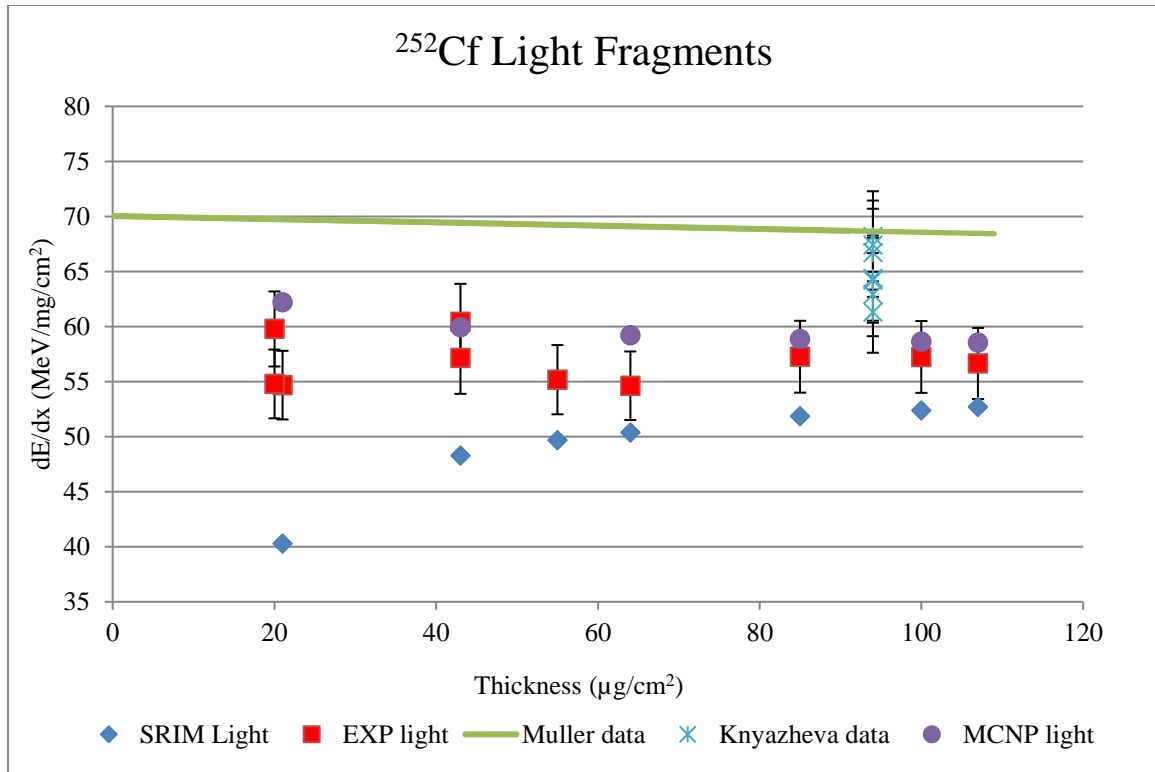
Figure 64: Stopping power of light fragments over different thickness of carbon foils.

In Figure 63 and Figure 64 our experimental data is shown as red squares; the purple circles are MCNP results and the blue diamonds are SRIM results. The green line is data collected from Muller presented as a straight line (Muller and Gonnenwein 1971), for various thicknesses of carbon foils, added to these graphs as reference. The blue asterisks are data from Knyazheva et al. (Knyazheva, et al. 2006), which is for several different nuclides through the same thickness foil, and corrections were made to the Knyazheva et al. data in the final plot that is related to the semi-empirical fit. There is a good agreement between our experimental data and MCNP results for both the light and heavy fragments. SRIM, on the other hand, consistently understates the energy loss for both light and heavy fragments.

An important motivation for understanding energy loss is, as mentioned, for energy add-back through timing foil 2 and the SiN window to relate the IC detected energy to the energy in the TOF region. Since the data studied was only for the average energy of the two peaks and for energy loss correction to the spectrometer data, we needed to correct for multiple Z and A values, therefore the experimental stopping power was compared to the SRIM stopping power, as was done by previous researchers.

It appears better to use MCNP but for ease of calculation SRIM may be used with a factor understood between the calculated and experimental values. A relationship can be made now for any thickness of foil that is used, to compare to the 94 $\mu g/cm^2$ that was ran by Knyazheva et al. Their values for experimental to SRIM ratio, Exp/SRIM, for a 94 $\mu g/cm^2$ foil is 1.15 ± 0.07 for light fragments and Exp/SRIM = 1.30 ± 0.08 for heavy fragments, while for 100 $\mu g/cm^2$ carbon foils they are Exp/SRIM light = 1.09 ± 0.07 and Exp/SRIM heavy = 1.30 ± 0.07. More important to us as most of the foils that we used were not 94 $\mu g/cm^2$ but were 21 $\mu g/cm^2$, these ratio values for this thinner foil are Exp/SRIM light = 1.40 ± 0.08 and Exp/SRIM heavy = 1.84 ± 0.10. As seen in the stopping power graphs as a function of carbon foil thickness, Figure 63 and Figure 64, the experimental values seem to slightly increase with a thinner foil while SRIM shows it to decrease.

Figure 65 is a ratio of energy loss found experimentally divided by energy loss from SRIM, with a comparison to the published Knyazheva et al. ratio values, triangle data points.
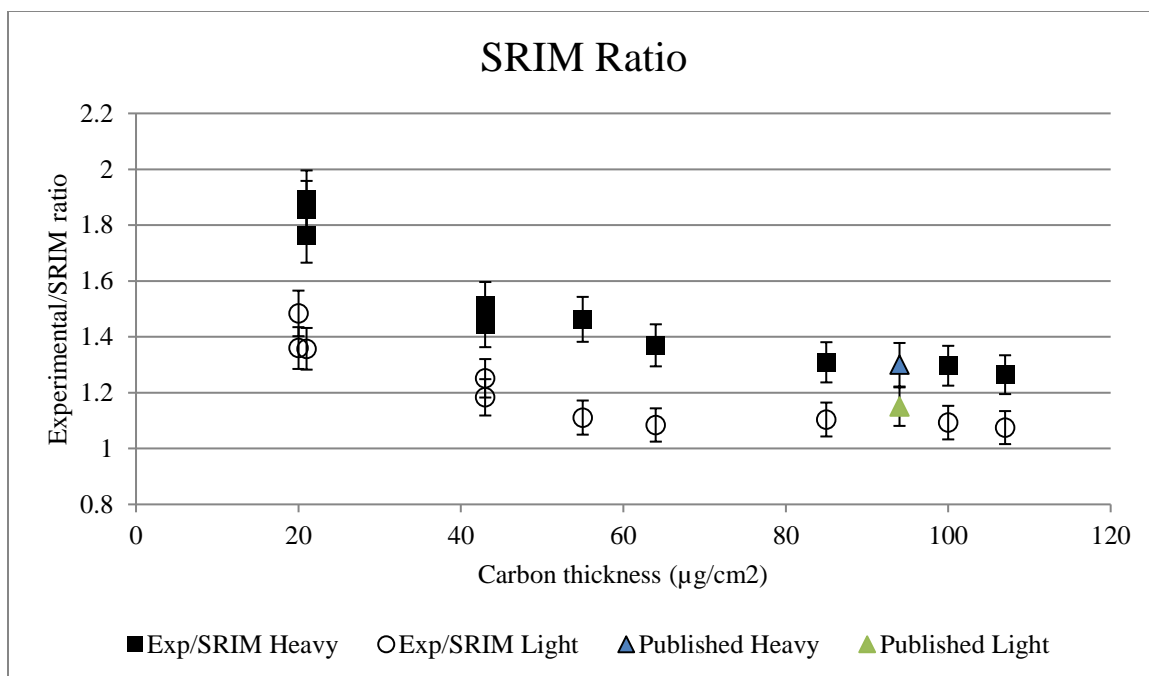
Figure 65: Experimental/SRIM ratio for different thicknesses of carbon foils.

The same ratio comparison is plotted for MCNP simulation results in Figure 66, this ratio is much more flat and close to 1 than the SRIM ratio.
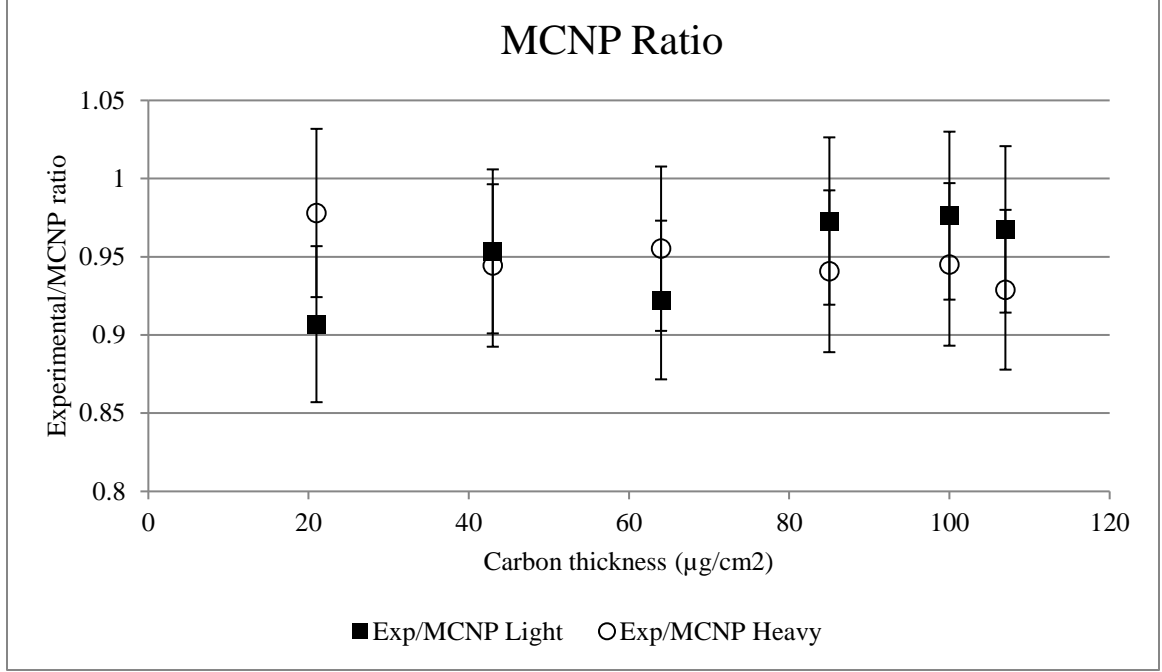
Figure 66: Experimental/MCNP ratio for different thicknesses of carbon foils.

The determination of the error was calculated using the method in Knyazheva et al., which is stated as Equation 7, where $\left(\frac{\delta E}{E}\right)$ is the accuracy of the energy measurement and $\frac{\delta(\Delta x)}{\Delta x}$ is the accuracy of the foil thickness determination (Knyazheva, et al. 2006).

Equation 7

$$\frac{\delta(dE/dx)}{dE/dx} = \sqrt{\left(\frac{\frac{E_{hole}}{\sqrt{N_{hole}}} + \frac{E_{foil}}{\sqrt{N_{foil}}}}{E_{hole} + E_{foil}}\right)^2 \times \left(\frac{\delta E}{E}\right)^2 + \left(\frac{\delta(\Delta x)}{\Delta x}\right)^2}$$

The overall accuracy is calculated as 5.7%, by using 0.9% for the energy resolution and 5.5% for the accuracy of the foil thickness.

Silicon nitride windows were used in both the UNM spectrometer and the LANL

SPIDER fission fragment spectrometer, thus the same analysis was done on this material.

Figure 67 shows the experimental and simulation results for the 12 mbar run. Since the

first measurements were taken at 12 mbar (9 torr), a more extensive set of thicknesses of

the windows were taken. When the same set-up was rerun in the more air tight chamber,

only runs with 200 nm and 500 nm SiN window were done; these data points are shown

in Figure 67. The experimental set-up of the 700 nm and 900 nm thick SiN runs

consisted of stacking the 200 nm and 500 nm windows and with this being such a delicate

process these runs were not repeated in the later 0.22 mbar chamber. Figure 68 shows the

stopping power of the two runs that were completed at a pressure of 0.22 mbar, along

with SRIM and MCNP results.
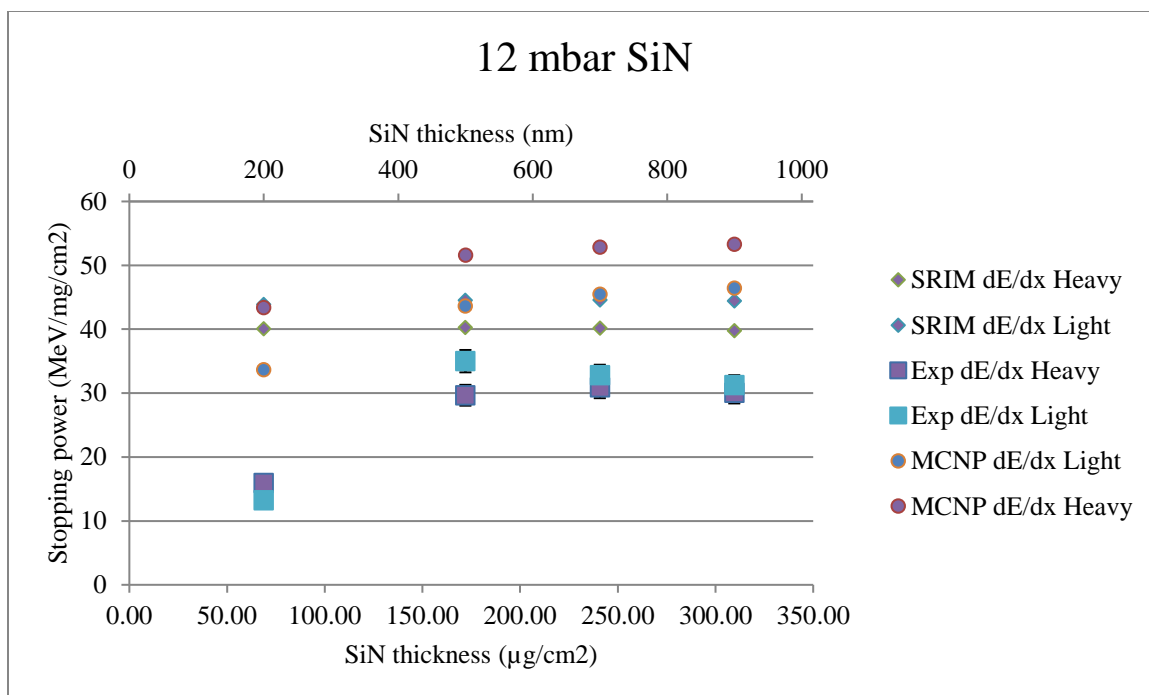
Figure 67: Stopping power of light and heavy fragments at 12 mbar of silicon nitride.
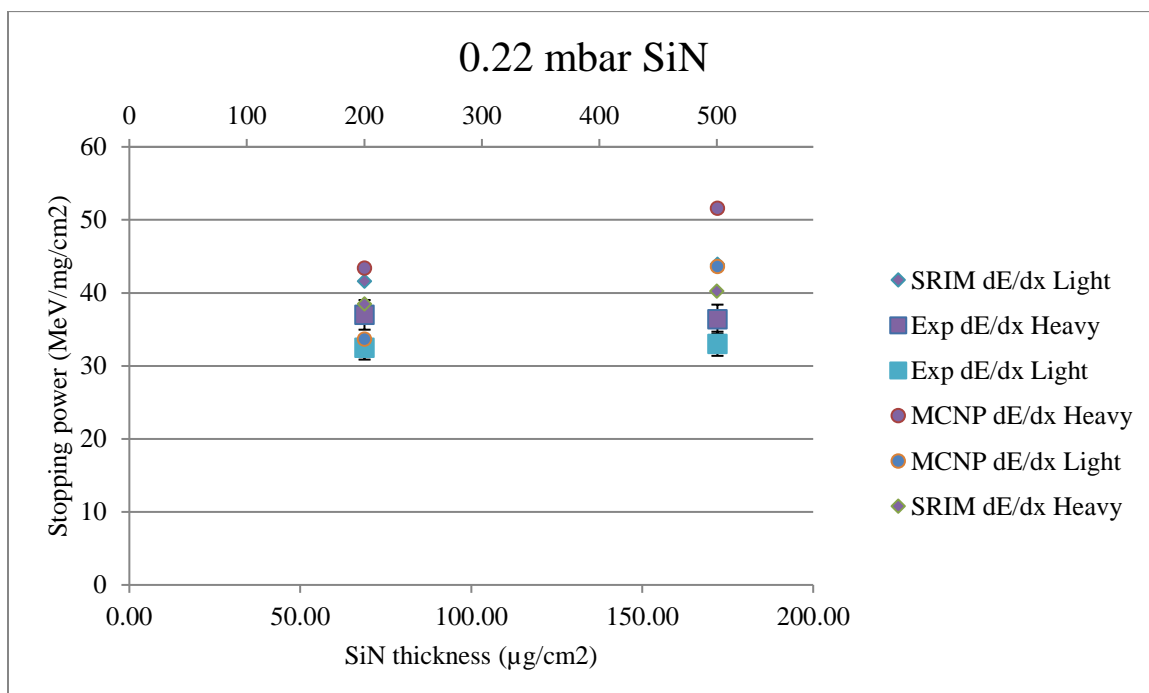
Figure 68: Stopping power of light and heavy fragments at 0.22 mbar of silicon nitride.

Figure 69 is the experimental/SRIM ratio of the both the 12 mbar and 0.22 mbar stopping

power values. For the 12 mbar pressure and 200 nm thick (68 μg/cm^2) SiN window, the

Exp/SRIM ratio is very low compared to the other values. The ratio for the 200 nm

window at 0.22 mbar, experimental versus SRIM is then found as Exp/SRIM light = 0.97

± 0.13 and Exp/SRIM heavy = 0.85 ± 0.09, this shows that SRIM is overestimates the

stopping power compared to our experimental data. The ratio is much closer to one for

the 500, 700, and 900 nm thickness (172, 240, and 309 μg/cm^2, respectively) though still

typically only about 0.8. Figure 70 is the experimental/MCNP ratio for both the 12 mbar

and 0.22 mbar runs. The MCNP simulations still overestimate the energy loss through

SiN, similar to SRIM, again with the thinnest window at 12 mbar being the farthest ratio

from 1.
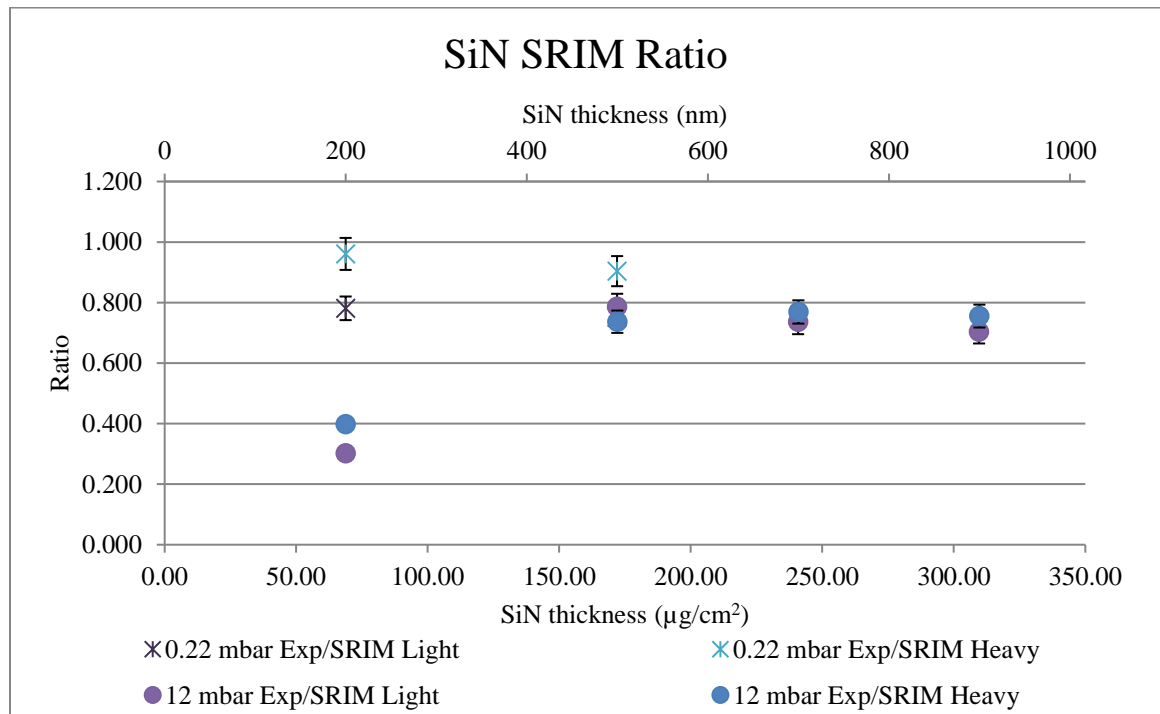
Figure 69: Experimental/ SRIM ratio for different thicknesses of silicon nitride.

94
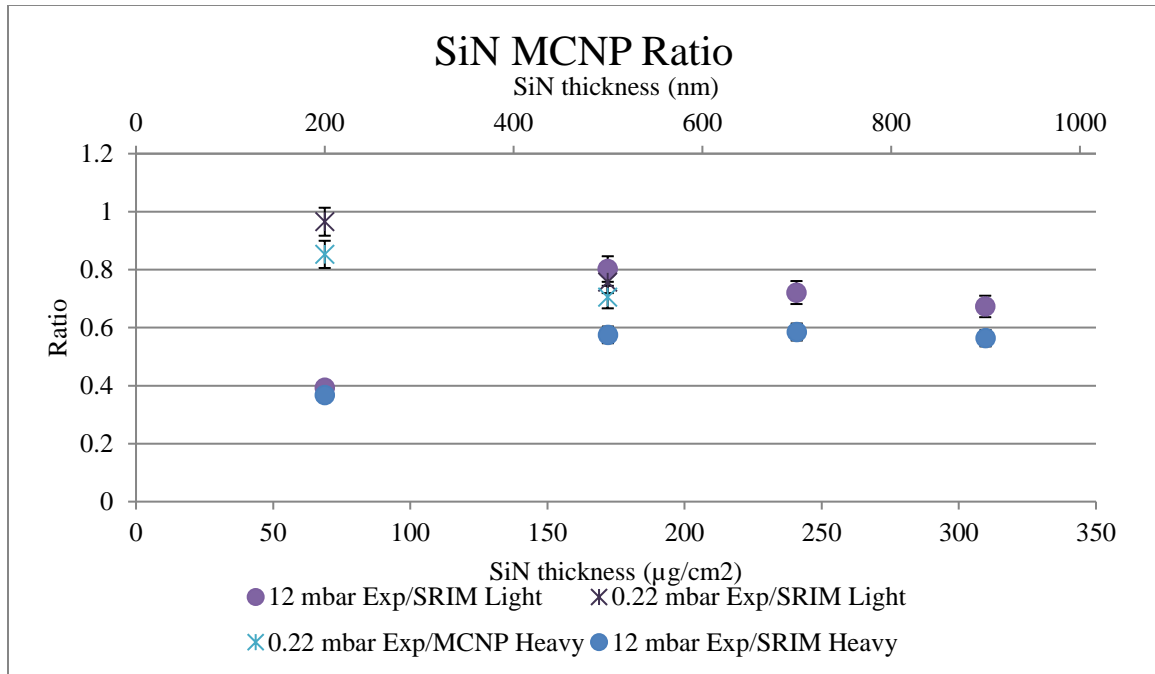
Figure 70: Experimental/ MCNP ratio for different thicknesses of silicon nitride.

SiN has a lower stopping power than the carbon foils, 35 compared to 65 MeV/mg/cm^2. The Experimental/SRIM energy loss ratio has been calculated for different thicknesses of carbon foils and silicon nitride windows. Using this information and with the fission fragment data from Schmitt et al. (Schmitt, Kiker and Williams 1965), reproduced in Table 2, simulations were performed using both SRIM and MCNP. For the 21 $\mu g/cm^2$, the ratio values are Exp/SRIM light = 1.40 ± 0.08 and Exp/SRIM heavy = 1.84 ± 0.10. And for the 200 nm SiN window Exp/SRIM light = 0.96 ± 0.13 and Exp/SRIM heavy = 0.78 ± 0.10. In the stopping power graphs of carbon foils, MCNP follows the same trends as our data; MCNP gives numbers that more closely match experiment values with an Exp/MCNP ratio of 1 for heavy fragments and 0.9 for light fragments for a 21 µg/cm^2; and a 200 nm silicon nitride window with a ratio of 0.85 for heavy fragments and 0.97 for light fragments.

8 Full System Analysis

The emphasis of this thesis work is to understand the sources of uncertainty in the system with the goal of reducing the uncertainties and sharpening the system resolution. Following the explanation of the velocity and energy measurement dependence on the extracted mass presented in chapter 2.3, we can understand the relation between timing and energy uncertainty and the mass uncertainty. Both the timing and energy uncertainties are examined here to try to understand the many contributions to the measured uncertainties, and to estimate what part is inherent to fission fragment measurements in the UNM fission fragment spectrometer.

In chapter 2 we saw the basic v-E setup, reproduced in Figure 71 below. The fractional uncertainty in mass determination, also presented in chapter 2, is also reproduced here for discussion: $\frac{dm}{m} = \sqrt{\left(\frac{\partial E}{E}\right)^2 + \left(\frac{2\,\partial L}{L}\right)^2 + \left(\frac{2\,\partial t}{t}\right)^2}$. As mentioned, the time-of-flight is measured as the time between the signal from timing modules t1 and t2. There is energy loss in all interactions, the t1 and t2 carbon conversion foils and the SiN entrance window to the ionization chamber, which causes a broadening of the energy distribution.

Figure 71: v-E detector.

To determine the mass, the time-of-flight reading and the reading of the energy detector are correlated for each particle. To extract energy in the TOF region, where v is measured, to apply the basic kinematic equation relating energy, velocity, and mass means that we have to correct the energy reading just for the energy loss from the t2 carbon foil and the SiN entrance window for addback. The TOF has some inherent resolution limits, as does the energy reading from the ionization chamber, and so both these components of the system need to be characterized.

The easiest approach to characterizing the system would be to use calibration beams. Unfortunately we do not have access to these. To understand the TOF and energy resolution for fission fragments, meaning the resolution we would find if we had perfect monoenergetic beams of an individual particular fission fragment species, we have to extrapolate from alpha particle data, energy loss data, and simulations, using uncertainty analysis to handle energy and timing broadening.

In this chapter we work to analyze the individual factors going into the energy and timing broadening seen in measurements, and extract the contributions from these factors. The factors that we are considering are the sources themselves, the carbon foils and SiN windows, and the inherent limitations in the resolutions of the PIPS detector and the ionization chamber.

8.1   Alpha Uncertainty

The uncertainty of the measurements in the thesis are due both to inherent uncertainties in the system and in uncertainties in the sources used. We attempt to isolate the uncertainty contributions of the detector, the sources themselves, and the foils in the energy measurements. We then extend this to the uncertainty in the TOF measurements. The source broadening translates to timing broadening and energy broadening, so the first step to backing out the uncertainty of the system is to understand the broadening due to the sources.

The TriNuc, ^{239}Pu, and ^{252}Cf sources were all examined to determine the energy broadening in the sources themselves, using the alpha spectrometer and identical experimental set-up, described in chapter 7.1.3.1. Using the energy broadening, the velocity broadening and thus the timing broadening can be calculated. The timing broadening information can also be used to determine a more accurate FWHM for the time-of-flight system. After analyzing alpha particles, assumptions can be made about fission fragments. Light fission fragments have about the same velocity as the alpha particles studied, though there is more energy loss and thus broadening. Heavy fragments are slower and more charged and thus the broadening is even greater. Correlations between alphas and fission fragments will be made, but these can only be approximate.

In this section, we attempt to isolate the uncertainty contributions of the detector, the sources themselves, and the foils in the energy measurements. We then extend this to the uncertainty in the TOF measurements.

8.1.1   Source

Finding the uncertainty in the ^{239}Pu source in important to use while finding the broadening in the TOF. We compare the TriNuc to the ^{239}Pu source using the PIPS detector. The PIPS detector has some inherent resolution at the relevant alpha particle energies and the sources have some broadening, which gives the measured spectrum broadening. To extract individual contributions, we can write:

$$\sigma^2_{measurement} = \sigma^2_{Detector} + \sigma^2_{source\ itself}$$

From Canberra's data sheet, the model number A450-18AM correlates to an active area of 450 mm^2 and an alpha resolution of 18 keV FWMH for ^{241}Am 5.486 MeV line using a 0.5 μs shaping time constant (Canberra 2012). The detector used in these experiments was labeled A450-20AM which thus, from the labeling has a listed resolution of 20 keV FWHM. The measured FWHM for the tri nuclide source was 16.5 keV, very close to the listed value. Since the measured value of the TriNuc source is smaller than the listed detector resolution, this lower value will be used for the detector resolution. As we performed measurements with a much more active, but broader energy distribution ^{239}Pu source, the ^{239}Pu peaks from the TriNuc source are shown in Figure 72, for comparison

with the more active ^{239}Pu source in Figure 73, repeated from Figure 52 for the sake of clarity here.
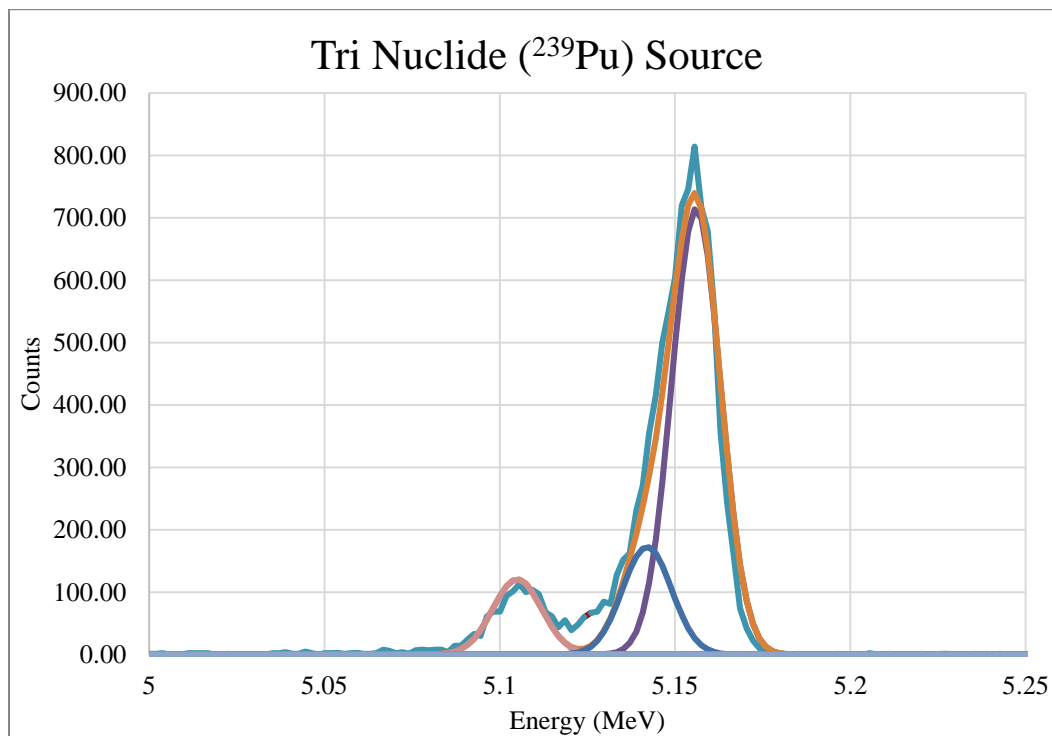
Figure 72: Tri Nuclide (^{239}Pu) alpha spectrum FWHM 16.5 keV.
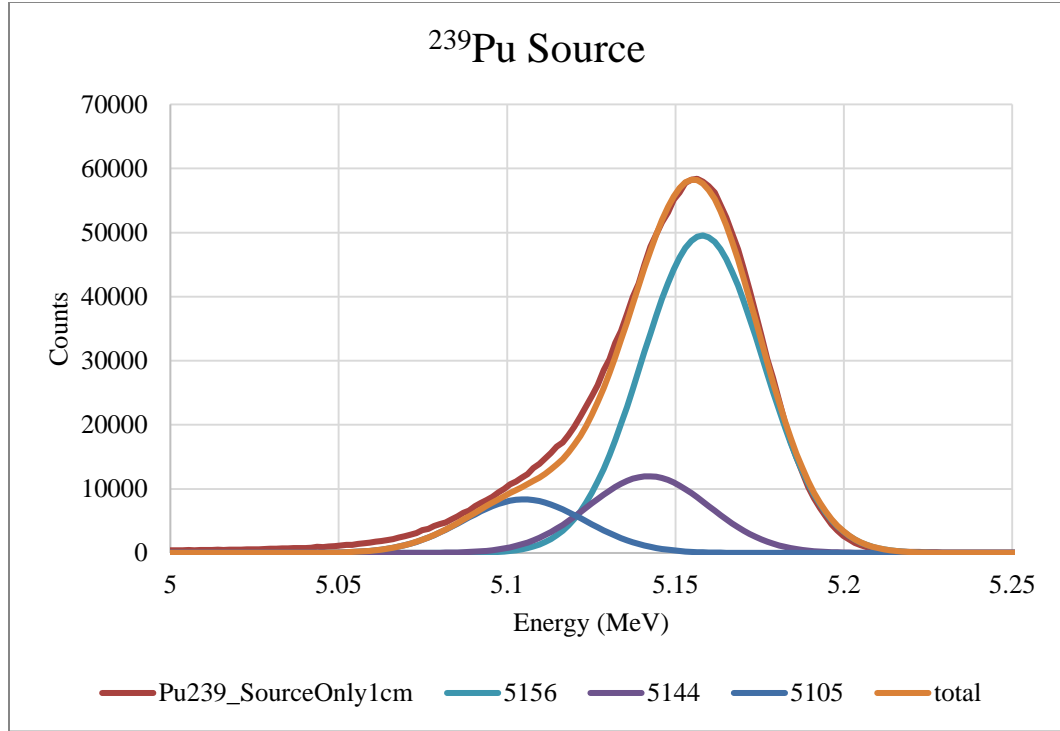
Figure 73: ^{239}Pu source alpha spectrum FWHM 42.4 keV.

The TriNuc source was replaced by the ^{239}Pu source in the same set-up, with a resulting

FWHM of 42.4 keV for the most active branch, 5156 keV. Using the previous Equation

8 showing adding uncertainties in quadrature, and the linear relation between sigma and

FWHM for Gaussian shaped distributions, and using the FWHM of the detector as 16.5

keV, the FWHM of the ^{239}Pu source is calculated as 39 keV.

This uncertainty is also performed on the ^{252}Cf alpha spectrum with only the source and

detector and no intervening foils, in Figure 74, with a measured FWHM of 28.3 keV.

Then by again using Equation 8, a final FWHM of 23 keV is calculated.
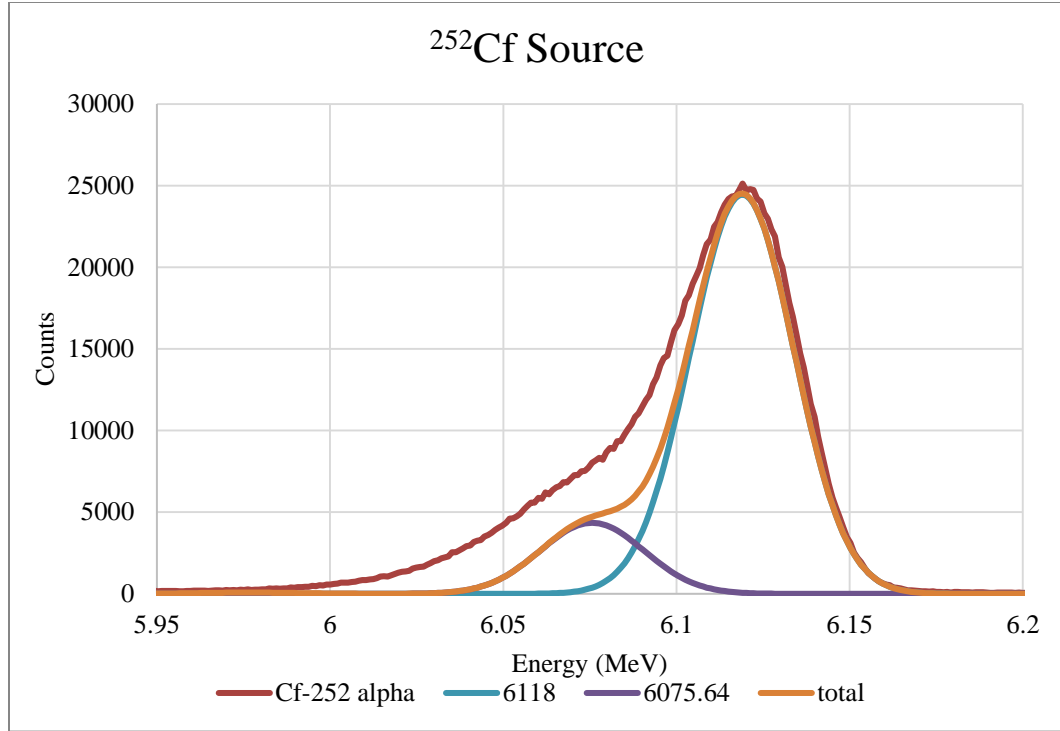
Figure 74: ^{252}Cf source alpha spectrum FWHM 28.3 keV.

8.1.2 Carbon Foil

By estimating the energy broadening the source itself introduces we can examine the energy loss experiments using Carbon and SiN foils with the Pu source, and understand the energy broadening contribution from just the foil. Equation 8 is expanded to show more individual contributions as Equation 9:

Equation 9

$$\sigma^2_{\substack{measurement \\ through\ foil}} = \sigma^2_{PIPS} + \sigma^2_{Pu-239\ \alpha} + \sigma^2_{Foil}$$

With a measured FWHM of 44.7 keV through the 20 µg/cm² foil then the math becomes

$44.7^2 = 16.5^2 + 39^2 + \sigma_{Foil}^2$ where sigma really represents FWHM here as in the rest of the thesis. Thus, we extract a FWHM due to the 20 µg/cm² foil contributions of 14.4 keV, or a fractional FWHM/centroid value of $\frac{\delta E}{E} = \frac{14.4\ keV}{5130\ keV} = 0.28\%$.

Similarly, for the 100 µg/cm foil with a measured FWHM of 54.1 keV we find $54.1^2 = 16.5^2 + 39^2 + \sigma_{Foil}^2$, giving a FWHM contribution from just the foil of 33.7 keV and a fractional broadening value from the 100 µg/cm² foil of $\frac{\delta E}{E} = \frac{33.7\ keV}{5052\ keV} = 0.67\%$

Simulations allow perfect beams and an isolation of just foil contributions. A SRIM simulation of the 3 foils used in chapter 5 is summarized in Table 14, to highlight the different in energy straggling in this simulation. It is noted that these values are smaller than extracted values, which may indicate unconsidered sources of broadening.

Table 14: SRIM δE/E for different thicknesses of carbon foils with a [239]Pu alpha.

	20 µg/cm²	55 µg/cm²	100 µg/cm²
E	5140	5077	5112
δE/E	0.06 %	0.08%	0.11%

8.1.3   Time Broadening

Broadening in the alpha particle energy, broadens the alpha particle velocity distribution, and thus broadens the measured TOF spectra. To convert the energy broadening to a timing broadening we begin with the classical kinematics equation.

$$E = \frac{1}{2}mv^2 = \frac{1}{2}m\frac{t^2}{L^2}$$

$$\left(\frac{\sigma_E}{E}\right)^2 = \left(\frac{\sigma_m}{m}\right)^2 + \left(2\frac{\sigma_L}{L}\right)^2 + \left(2\frac{\sigma_t}{t}\right)^2$$

As the TOF length is fixed, as is the mass of the alphas, this simplifies to

$$\frac{\sigma_E}{E} = 2\frac{\sigma_t}{t}$$

Or for σ_t in terms of σ_E

$$\boxed{\sigma_t = \frac{t*\sigma_E}{2E}}$$

Note the σ used is the FWHM and not the standard deviation, but the formulas are clearer to write.

With another rearrangement of the classical kinematics equation, the time-of-flight based on the energy of a particle is $t = \dfrac{L}{\sqrt{2*\frac{E}{m}}}$

We can now apply this to separate the contributions in the TOF from the ^{239}Pu source. For the source with no foil we extracted an energy width of 39 keV. The timing broadening just due to this energy width contribution is

$$\sigma_{Pu-239\ \alpha} = \frac{31709ps*39keV}{2*5156keV} = 119.8ps$$

Using the 119.8 ps contribution from the source broadening and the measured broadening from the source alpha particles passing through the foils, we can extract the TOF broadening contribution from just the foils:

$$\sigma^2_{\substack{measurement \\ \alpha\ Foil}} = \sigma^2_{Pu-239\ \alpha} + \sigma^2_{Foil} + \sigma^2_{Other\ system\ effects}$$

Particle per particle the energy broadening of the t1 foil gives a broadening to the TOF distribution, each TOF data point is precisely measured. There is little broadening of alphas compared to fission fragments, and using alpha data we extrapolate back to a zero thickness for t1 foil and thus a zero foil based straggling TOF. The FWHM extracted of the system, without foil broadening, is 160 ps. Therefor without either the foil or source broadening contributions, the TOF system appears to have a FWHM resolution of 118 ps for a single particle measurement. An additional broadening from all the other factors is noted in the direct experimental data of ensembles of particles. Table 15 summarizes the fractional timing resolution for a zero thickness, 20 µg/cm^2 and 100 µg/cm^2 carbon foils, for a TOF distance of 50 cm.

	Zero thickness	20 µg/cm²	100 µg/cm²
Measured FWHM (ps)	168	200	306
Source contributions removed (ps)	118	160	282
Measured Energy (MeV)	5.156	5.130	5.052
TOF (ps)	31709	31789	32033
δt/t %	0.37	0.50	0.88

8.1.4   1 Meter TOF

As we are seeking to improve resolution, δt/t can be improved by increasing the TOF

path length and thus t. Though energy straggling, and thus velocity straggling, would

also increase δt, any constant factors such as system limitations would be constant. In

addition, as masses are determined particle by particle, the energy straggling into the

TOF system should be of no consequence to mass determination and increasing the TOF

length would only improve the δt contributions to improving the δm/m resolution.

To reiterate from chapter 2.2.1.2 previous TOF resolution measurements, using a meter

as the time-of-flight, and the ~80-100 µg/cm² carbon foil gives a FWHM of 372 ps and

fractional timing uncertainty of $\frac{372ps}{64067ps} = 0.58\%$.

In the previous section, the measured FWHM of Pu alphas was stated as 44.7 keV. Using

this energy broadening over a 1 meter flight path gives a timing FWHM of $\sigma_t =$

$\frac{63578ps*44.7keV}{2*5130keV} = 277\ ps$. The fractional uncertainty then is δt/t = 277 ps/63578 ps =

0.44%. We would like to know the width of the time of flight if we had a monoenergetic source, that is without the source width contributions and without the PIPS detector characterization width, which is not relevant here. Using the 14.4 keV width from just the t1 foil contributions as presented when removing the source and PIPS detector contributions to the 44.7 keV measured width, so for a monoenergetic beam of 5130 keV alpha particles into the t1 foil, this becomes 89 ps or 0.14 % TOF resolution. This of course does not consider broadening due to the TOF system itself.

8.2   IC Alpha Energy Spectrum

Just as there is an inherent resolution limit in the PIPS detector, there is a limit for the ionization chamber. The resolution is expected to be different for fission fragments vs. alpha particles, as there is a great difference in signal size and thus charge counting statistics, but the alpha particles are very well controlled for mass and energy, and there are direct measurements with these, and so we begin analysis of the ionization chamber with alpha particles.

Previously alpha particles have been measured in the ionization chamber with a range of conditions, with different windows, gas, and pressures. The windows used are 1.5 µm thick Mylar and 200 nm thick SiN. The gases used are isobutane or P-10, an argon-methane gas mixture with 10% methane. The pressures are high enough to stop the alpha particles within the 9 cm active region of the ionization chamber, which is higher than the pressures used for much higher stopping power fission fragments.

8.2.1 Ionization Chamber ^{252}Cf Alpha Particle Spectrum

A ^{252}Cf alpha particle spectrum from the ionization chamber, using P-10 gas and a 1.5 μm thick Mylar entrance window, is shown in Figure 75. The FWHM is 81 keV, giving a fractional energy resolution of δE/E = 1.33%. The contributions to the broadening come from the source itself, the Mylar entrance window, and the inherent response of the ionization chamber. From the previous section we extracted a source contribution of 23 keV FWHM. We do not have direct measurements from Mylar but use a SRIM derived broadening of 19.4 keV. Adding the broadening contributions in quadrature as before, using following equation

Equation 11

$$\sigma^2_{measurement \atop \alpha} = \sigma^2_{Window} + \sigma^2_{Cf-252\ \alpha} + \sigma^2_{IC\ \alpha}$$

We find the broadening contribution of the ionization chamber itself of 75.6 keV for ^{252}Cf alpha particles through a Mylar window into P-10 gas, giving a fractional contribution δE/E of 1.23%.

Measurements were also performed for the ^{252}Cf alpha particles into the ionization chamber, but through a 200 nm SiN window into isobutane gas. The spectrum is shown in Figure 76. The measured width is 76.8 keV, the ^{252}Cf source contribution is 23 keV once again, and the SRIM modeled SiN window contribution is 12.3 keV. Using the

same Equation 11 for the Mylar window above, a broadening contribution from the

ionization chamber is found with 72.2 keV FWHM, or a δE/E of 1.18%

These δE/E values are extremely similar, the P-10 value was 75.6 keV and the isobutane

value was 72.2 keV.   If the window contributions were removed correctly, the slight

difference between the two values should be from the type of gas used. Every bit helps in

tight improvements in resolution, and the small differences for alpha particles may

translate to large differences for fission fragments.
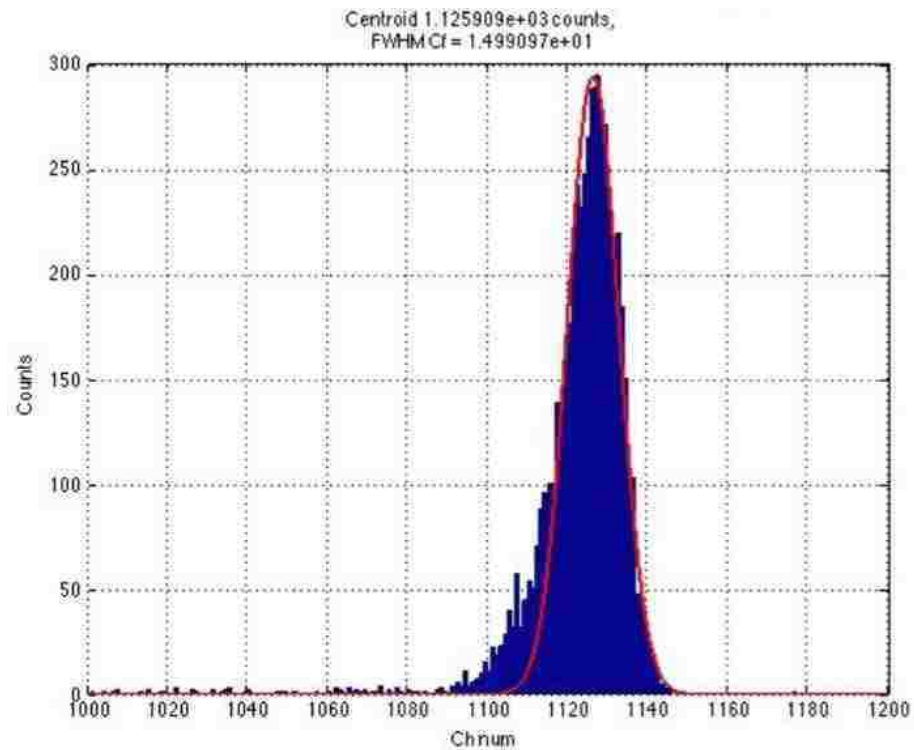
Figure 75: ^{252}Cf alpha resolution for P-10 gas and 1.5µm Mylar (Cole 2016) FWHM 14.9 ch (81 keV).
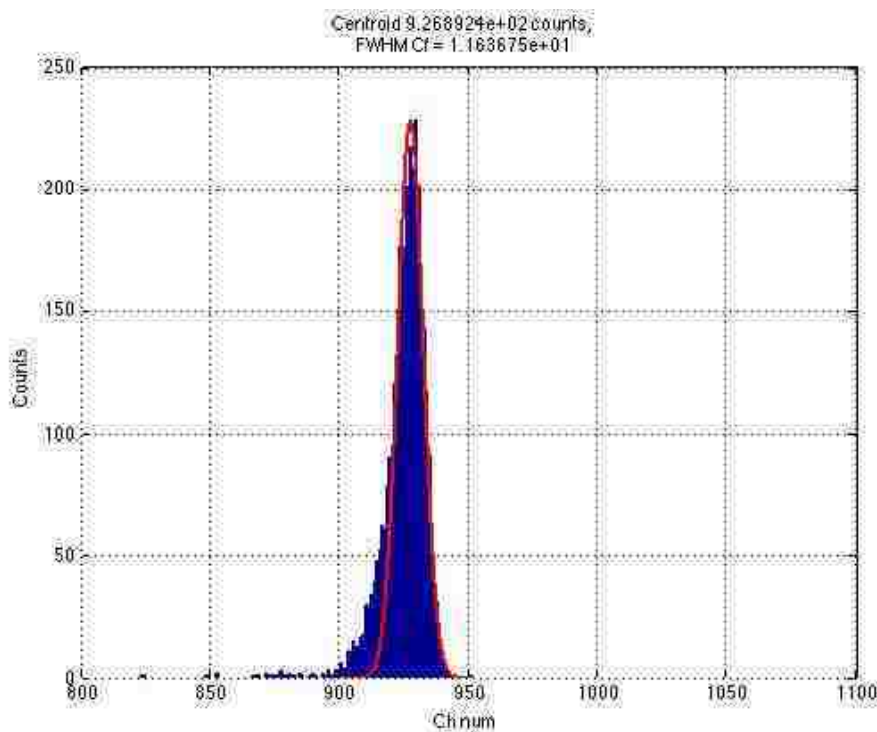
Figure 76:[252]**Cf alpha resolution for isobutane and 200 nm SiN window (Cole 2016) FWHM 11.6 ch (76.4 keV).**

8.2.2 Tri Nuclide IC Spectrum

Ionization chamber measurements were also performed with the TriNuc source, which has a much smaller source energy broadening. These measurements were performed using isobutane gas and a 200 nm thick SiN entrance window, as with the second set of [252]Cf experiments, shown in Figure 77. A resolution of 1.25%, 1.18%, and 1.11% for a FWHM of 64 keV was obtained for the [239]Pu, [241]Am, and [244]Cm peaks respectively (Cole 2016). The value obtained from the weighted average of the resolutions gave an overall alpha resolution of 1.18%. Note that these are the measured resolutions in the IC without backing out individual contributions. The source width measurement for the TriNuc source using the PIPS detector showed a resolution sharper than the stated resolution of the PIPS detector itself, so the source broadening is assumed to be minimal. Other larger

110

contributions will make this irrelevant when adding in quadrature, we do not try and

extract any more information about the TriNuc source broadening, and use the 16.5 keV

FWHM PIPS measurement as the width of this source. The SRIM SiN window

broadening is estimated to be 12.5 keV FWHM for alpha particles. Adding in quadrature

we find the IC resolution, without window or source contributions, to be 1.11%. This is

close to, and consistent with the [252]Cf alpha particle resolution results of a 1.18%.
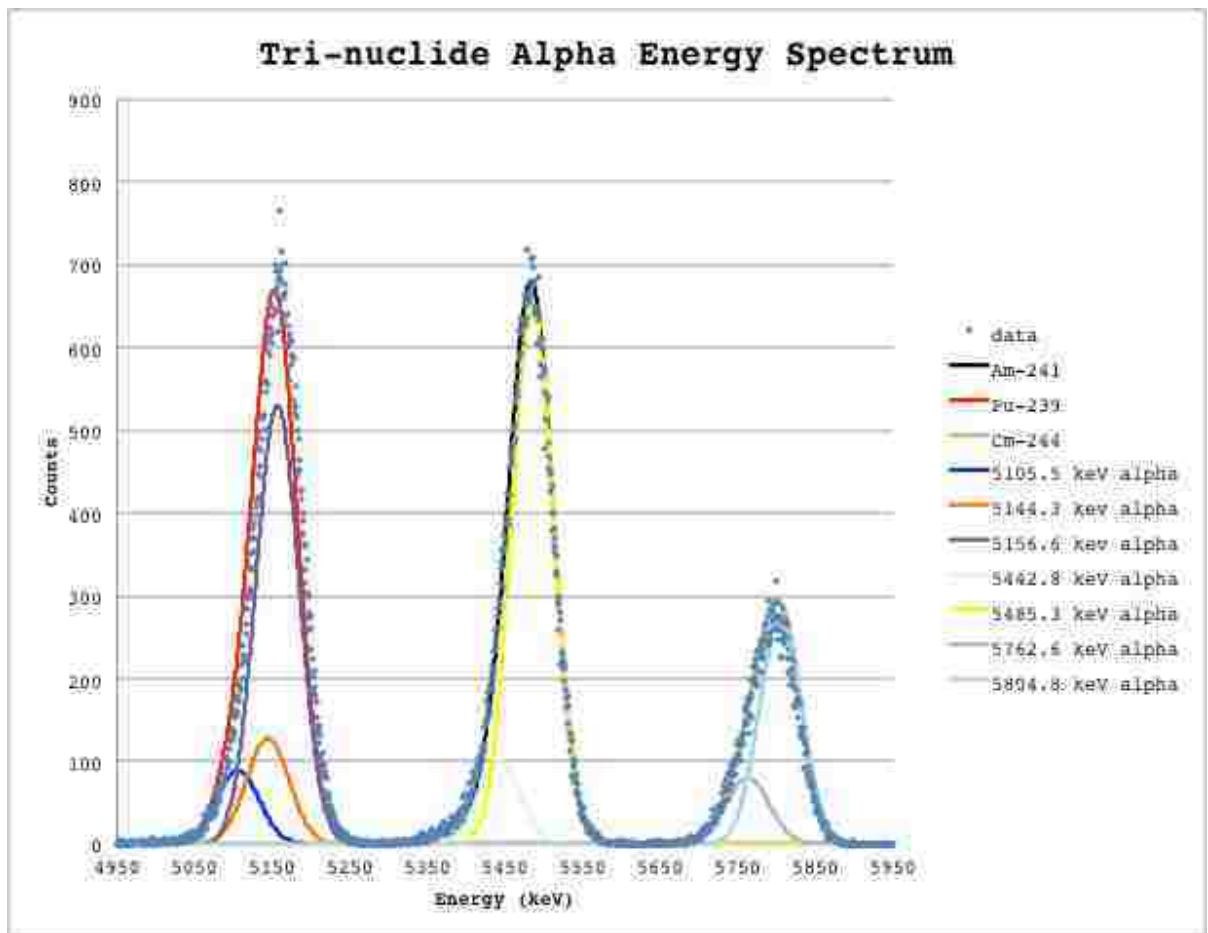
Figure 77: Tri-nuclide alpha energy resolution spectrum for isobutane and SiN window (Cole 2016) FWHM 64.5 keV.

8.3 Fission Fragment Mass Uncertainty

8.3.1 Using Alpha Resolution to Find Fission Fragment Resolution

We are pushing towards a better understanding of fission fragment energy broadening from the IC contributions, and there are several approaches. A calibration beam of nuclides and energies comparable to those found in fission would be perfect, but we do not have access to that. From actual fission, there is no beam of fission fragments, as it is a broad distribution, and resolution for individual nuclides cannot be measured directly. Experimentally we can extrapolate from alpha particle measurements. Other approaches are to use simulations such as SRIM and MCNP. SRIM is not well benchmarked for fission fragment particles and energies. We will explore both simulations and compare with experimental values.

The IC energy resolution was determined directly for alpha particles. The energy resolution for heavy ions can be inferred using statistical theory based on the number of charge carriers liberated in the IC gas, which is dependent on the incoming particle energy. Knoll gives a formulation of energy resolution of detectors based on the incident particle energy, E_{in} (Knoll 2010).

Equation 12

$$ER = \frac{2.35\sqrt{f}}{\sqrt{n_o}} = \frac{2.35\sqrt{fW}}{\sqrt{E_{in}}}$$

where f is the Fano-factor of the fill gas, W is the average energy lost by the incoming particle per ion pair formed, and n_o is the number of charge carriers which is directly proportional to the particle incoming energy, E_{in}.

The IC resolution for 5.5 MeV alpha particles, 1.11%, can be used as the basis of comparison. Substituting for different energies allows us to use ratios of the square root of energies to estimate ratios of the energy resolution. For heavy fragments from ^{252}Cf with an energy of 79.37 MeV, the energy ratio with alpha particles is 14.5 and so the resolution should scale as 1 over the square root of this ratio and be 0.29%. Similarly, for light ^{252}Cf fragments with an energy of 103.77 MeV, the resolution is expected to be 0.26%. To use this approximation based on charge counting statistics in the ionization chamber of course requires no effects based on the amount of charge. We know that there is a pulse height defect in the ionization chamber (we estimated a pulse height of 92% of a perfect pulse height for light and 86% for heavy in chapter 7.3.2.1), with recombination reducing the number of charges that are represented in the detector pulse height, and so the fission fragment resolutions are expected to be slightly poorer than these calculated values, but these resolutions still appear extremely good.

8.3.2   Summary of Uncertainties

We have examined TOF resolution and ionization chamber energy resolution. We have used alpha particles in place of a well-defined calibration beam, and extrapolated to fission fragment resolutions. We have also measured energy loss through carbon foils and SiN windows for alpha particles and for fission fragments, though without clear

experimental broadening information for fission fragments. We continue the analysis to derive mass resolution of the system for fission fragments. We begin by examining energy resolution estimates, then combine these with TOF resolution estimates.

8.3.2.1   Energy Resolution

Extrapolating from alpha resolution experiments and uncertainty analysis, we extracted a resolution of $\frac{\delta E}{E}_{Heavy} = 0.29\%$ and $\frac{\delta E}{E}_{Light} = 0.26\%$ for heavy and light fission fragments from ^{252}Cf, respectively. These values are summarized in Table 16. For comparison with literature,

Oed et al., (Oed, Geltenbort and Gonnenwein, et al. 1983) calculated the energy resolution for ^{235}U light and heavy fission fragments in an ionization chamber and found $\frac{\delta E}{E}_{Heavy} = 0.64\%$ and $\frac{\delta E}{E}_{Light} = 0.37\%$, values are summarized in Table 17. The resolution values for our experiment and Oed et al. are very close, and it becomes difficult to understand what exactly contributes to the differences when working with such small uncertainties.

Simulations were performed with the t2 20 µg/cm^2 carbon foil and the 200 nm SiN window to analyze the energy straggling, which is used as the only contribution to energy broadening as read by the detector as a single energy into a simulated detector would only give a single energy reading for the codes used. For SRIM for ^{252}Cf the average light and heavy fission fragments show a resolution of $\frac{\delta E}{E}_{Light} = 0.44\%$ and $\frac{\delta E}{E}_{Heavy} =$

1.30%, these values are summarized in Table 18. As these values are larger than what either we or Oed measured this suggests that SRIM is not optimized for examining fission fragment energy straggling through thin targets.

8.3.2.2 Time and Mass Resolution

Using the FWHM timing from the thinnest foil as 160 ps (removing source broadening contributions) and the average light and heavy masses a δt/t is calculated for both a 50 cm and a 1 meter TOF path length and is summarized for each different method of calculating δE/E; where $\frac{\sigma_m}{m} = \sqrt{\left(\frac{\sigma_E}{E}\right)^2 + \left(2\frac{\sigma_t}{t}\right)^2}$

After the t1 foil each particle has a single energy and TOF and this is used to determine mass of each particle. There is some randomization through t2 foil and SiN and gas ionization and thus the energy read out.

For a distribution, even a monoenergetic beam going through the t1 foil would be broadened, widening the TOF distribution. Since we are correlating v and E particle by particle we are not concerned with this distribution hence we use the 160 ps FWHM. The relevant IC read broadening is a result of energy broadening from the SiN and the t2 foil, and the charge carrier statistics in the gas. While a single add-back value may exist for a particular nuclide at a particular energy, to correlate the IC reading to the energy in the TOF region, these add randomness to the add-back value and thus the reconstructed energy in the TOF region important for each particle's mass reconstruction.

Tables follow, with the best experimental scenario for our device with a 50 cm and 1 m

TOF path length in Table 16. Table 17 uses our device but with the Oed et al. published

values for δE/E (Oed, Geltenbort and Gonnenwein, et al. 1983), which are slightly larger

than our extrapolated values. Table 18 uses our device, but with larger SRIM calculated

values for δE/E.

Table 16: Summary of uncertainty for ^{235}U and ^{252}Cf for a TOF of 0.5 and 1m using best experimental scenarios for δE/E.

	δE/E % Exp	δt/t % 0.5m	δm/m % 0.5m	δt/t % 1m	δm/m % 1m
^{235}U Light	0.25	0.46	0.95	0.23	0.52
^{235}U Heavy	0.31	0.31	0.70	0.16	0.44
^{252}Cf Light	0.26	0.44	0.92	0.22	0.51
^{252}Cf Heavy	0.29	0.33	0.73	0.17	0.44

Table 17: Summary of uncertainty for ^{235}U and ^{252}Cf for a TOF of 0.5 and 1m using OED published values for δE/E.

	δE/E % OED	δt/t % 0.5m	δm/m % 0.5m	δt/t % 1m	δm/m % 1m
^{235}U Light	0.38	0.46	0.99	0.23	0.60
^{235}U Heavy	0.73	0.31	0.97	0.16	0.80
^{252}Cf Light	0.37	0.44	0.95	0.22	0.58
^{252}Cf Heavy	0.64	0.33	0.93	0.17	0.72

	δE/E % SRIM	δt/t % 0.5m	δm/m % 0.5m	δt/t % 1m	δm/m % 1m
^{235}U Light	0.47	0.46	1.03	0.23	0.66
^{235}U Heavy	1.49	0.31	1.62	0.16	1.52
^{252}Cf Light	0.45	0.44	0.99	0.22	0.63
^{252}Cf Heavy	1.30	0.33	1.46	0.17	1.35

By using the thinnest of carbon foils on both timing modules and assuming the best resolution from the IC, the mass resolution is well below 1% for light and heavy fragments for 50 cm and 1 m TOF. Due to pulse height defect reducing counting statistics we expect the fission fragment energy resolutions to be slightly poorer than the resolution extrapolated directly from the alpha calibration, but this should be still below 1 amu resolution. The only cases where it is above 1% is for heavy fission fragments using the SRIM calculated dE/E values and, again for SRIM, for the case of the light ^{235}U fragments with the 50 cm TOF. These results are extremely promising.

To put this into perspective for the resolution requirements, 1 amu resolution for light fragments requires 1.1 % resolution or better, and for heavy fragments 0.7 % or better. If our numbers are right we have achieved this for light fragments and are extremely close

for heavy fragments using the 50 cm TOF length, and have achieved this for the 1 m TOF length. If we are optimistic with our numbers, especially for energy resolution, we should still be close to our goals of 1 amu resolution. Again, the best way to test the resolution is with a calibration beam but, barring that, we have used uncertainty analysis and reasonable extrapolation.

9   Conclusions and Future Work

9.1   Conclusion

We extracted resolution information from several parts of the system to develop the full mass resolution accounting, and learned approaches to improve the system. The time-of-flight data has better resolution the thinner the foils and when the particles are emitted in the center and strike the t2 foil in the center. With the thinnest foil, 20 $\mu g/cm^2$, a FWHM value of 160 ps has been found. This is despite a portion of the time broadening due to the energy broadening of the source itself. When using the blockers on the second MCP, the center position resulted in a smaller FWHM while the corners resulted in a larger FWHM than when no blocker was used.

Using the FWHM of the 20 and 100 $\mu g/cm^2$ carbon foils for the TOF system, the hypothetical FWHM using a zero-thickness foil is calculated as 118 ps, this is compared to a FWHM of 371 ps previously measured with the 80-100 µg/cm² foils. That broad FWHM found previously was also from the total width of the peak and didn't consider the different alpha energy branches of ^{239}Pu. When considering the total peak to be composed of several different energy peaks, the FWHM of those individual energy peaks was found to be 329 ps.

Using the best-case scenario of very thin (20 µg/cm²) carbon foils and 0.5 m time-of-flight, and the best resolution for an ionization chamber extrapolated from alpha data, we extract a fission fragment resolution near or below 1 amu. 1 amu resolution corresponds

to resolution better than 1.1 % for light fragments and 0.7% for heavy fragments. Looking at the more stringent heavy fragments, for ^{252}Cf a δm/m of 0.73 % was found and for ^{235}U δm/m of 0.70% was found, for a 50 cm flight path. The values are all below 1 amu resolution for the 1 m TOF path.

As fission fragment energy loss is difficult to measure directly with our system and straggling is impossible due to the broad spread in products, calculations were performed. The energy loss of alphas and fission fragments in carbon foils and SiN can be compared well to SRIM and MCNP calculations. The carbon foil experimental energy loss was compared to simulations. SRIM underestimated the energy loss, which is consistent with previous published results on carbon foils. MCNP slightly overestimated energy loss, but this was closer to experimental energy loss values. SRIM and MCNP simulations for silicon nitride both overestimated energy loss compared to experimental data.

The Experiment/SRIM energy loss ratio for ^{252}Cf heavy fragments and light fragments for a 21 µg/cm^2 carbon foil are 1.8 and 1.4, respectively; and for a 200 nm silicon nitride window a ratio of 0.9 and 0.8, respectively.

The Experiment/MCNP energy loss ratio for ^{252}Cf heavy fragments and light fragments for a 21 µg/cm^2 carbon foil are 1 and 0.9, respectively; and for a 200 nm silicon nitride window a ratio of 0.9 and 1, respectively.

9.2 Comprehensive Energy Loss Calculations

To make the energy loss calculations more in depth, a method such as described by Knyazheva et al. (Knyazheva, et al. 2006) should be employed. That work used a thin foil and back to back fission fragment correlations. With the use of an MCP and a silicon detector, time-of-flight calculations can be made and mass information can be extracted. Using this information, the Schmitt calibration constants can be determined more precisely.

For other future work, the pressure in the experiment described in this paper is at 0.22 mbar. In contrast, the fission fragment spectrometer is run at a pressure of $3x10^{-8}$ mbar, more appropriate for fission fragments. That Canberra detector used is optimized for alphas, so a different PIPS detector optimized for fission fragments could be useful in improving future measurements.

10 Works Cited

Benetti, P., A. Broio de Tigliole, E. Calligarich, A. Cesana, R. Dolfini, T. Ioppolo, G. L. Raselli, and M. Terrani. 2002. "Measurement of fission fragments energy loss." *Nuclear Instruments and Methods in Physics Research A* 272-279.

Blakeley, R. 2013. *A Time-of-Flight Spectrometer for Fission.* M.Sc. Thesis, University of New Mexico.

Blakeley, Richard. 2017. "Development of The University of New Mexico Spectrometer for High-Resolution Fission Product Yield Data." *Dissertation Proposal.*

Bohr, Neils, and John Wheeler. 1939. "The Mechanism of Nuclear Fission." *Physical Review* 25.

Boucheneb, N., and P. Geltenbort. 1989. "High Resolution Measurements of Mass, Energy, and Nuclear Charge Correlations for 229Th(nth,f) with the Cosi Fan Tutte Spectrometer." *Nuclear Physics A, Volume 502* 261-270.

Canberra. 2012. "Passivated Implated Planar Silicon (PIPS) Detectors." Mirior Technologies, 4.

Cole, J. 2016. "An Ionization Chamber for High Resolution Fission Product Spectroscopy." Thesis.

Forgue, V., and S. Kahn. 1967. "Determination of Fission Fragment Energies using Solid-State Detectors." *Nuclear Instruments and Methods* 93-102.

Hakim, M., and N. H. Shafrir. 1971. "252Cf Fission Fragment Energy Loss
Measurements in Elementary Gases and Solids as Compared with Theory."
Canadian Journal of Physics 3024-3035.

Hamamatsu. 2001. "MCP Assembly." *Hamamatsu Technical Document.* Hamamatsu
Corporation.

Heffern, L. 2015. "Ionization Chamber Design, Development, and Testing for." Thesis.

Knoll, Glenn F. 2010. *Radiation Detection and Measurement (4th edition).* New York
City: John Wiley and SOns.

Knyazheva, G.N., S.V. Khlebnikov, E.M. Kozulin, T.E. Kuzmina, V.G. Lyapin, M.
Mutterer, J. Perkowski, and W.H. Trzaska. 2006. "Energy losses of 252Cf fission
fragments in thin foils." *Nuclear Instruments and Methods in Physics Research B*
7-15.

Lindhard, J., M . Scharff, and H . E . Schiott. 1963. "Range Concepts and Heavy Ion
Ranges." *Matematisk-fysiske Meddelelser* 4-44.

Magee, Chuck. 2011. *Lounge of the Lab Lemming.* March 19. Accessed 4 3, 2017.
http://lablemminglounge.blogspot.com/2011/03/why-fuel-rods-are-
radioactive.html.

Muller, R., and F. Gonnenwein. 1971. "Slowing Down of Fission Fragments in Various
Absorbers." *Nuclear Instruments and Methods* 357-363.

NNDC; Brookhaven National Laboratory. 2017. *National Nuclear Data Center.* 04 26.
Accessed July 2017. nndc.bnl.gov.

Oed, A., P. Geltenbort, F. Gonnenwein, T. Manning, and D. Souque. 1983. "High
Resolution Axial IOnization Chamber for Fission Products." *Nuclear Instruments and Methods* 455-459.

Oed, A., P. Geltenbort, R. Brissot, F. Gonnenwein, P. Perrin, E. Aker, and D. Engelhardt. 1984. "A Mass Spectrometer For Fission Fragments Based on Time-of-Flight and Energy Measurements." *Nuclear Instruments and Methods in Physics Research* 569-574.

Ozeroff, J. 1949. *Doc. AECD-2973.* US AEC.

2014. *Reltek.* Accessed 07 2017. reltekllc.com.

Schmidt, K. H., H. Wohlfarth, H.-G.Clerc, W. Lang, H. Schrader, and K. E. Pferdekamper. 1976. "Energy Loss , Enery Straggling, and Angular Straggling of Heavy Ions in Carbon Foils." *Nuclear Instruments and Methods 134* 157-166.

Schmitt, H.W., W.E. Kiker, and C.W. Williams. 1965. "Precision Measurements of Correlated Energies and Velocities of 252Cf Fission Fragments." *Physical Review* VOLUM E 137, NUMBER 4B.

Tretkoff, Ernie. 2017. "Discovery of Nuclear Fission." *American Physics Society.* July.

Weissenberger, Erwin, Peter Geltenbort, Anton Oed, and Friedrich Gönnenwein. 1986. "Energy calibration of surface barrier detectors and." *Radiation Effects* 47-51.

Wilkins, B.D., M.J. Fluess, S.B. Kaufman, C.E. Gross, and E.P. Steinberg. 1971. "Pulse-Height Defects for Heavy Ions in a Silicon Surface Barrier Detector." *Nuclear INstruments and Methods* 381-391.
124

Wiza, J. 1979. "Microchannel Plate Detector." *Nuclear Instruments and Methods* 162-587.

Ziegler. 1999. "The Stopping of Energetic Light Ions in Elemental Matter." *J. Appl. Phys / Rev. Appl. Phys* 1249-1272.

Ziegler, James. 2017. *Stopping and Range of Ions in Matter.* July.

Appendix

A.1   SRIM Stopping Power Accuracy Graphs

Only a handful of experiments have been done with the average light and heavy fission

fragment values and compared with SRIM's stopping power accuracy, shown in Figure
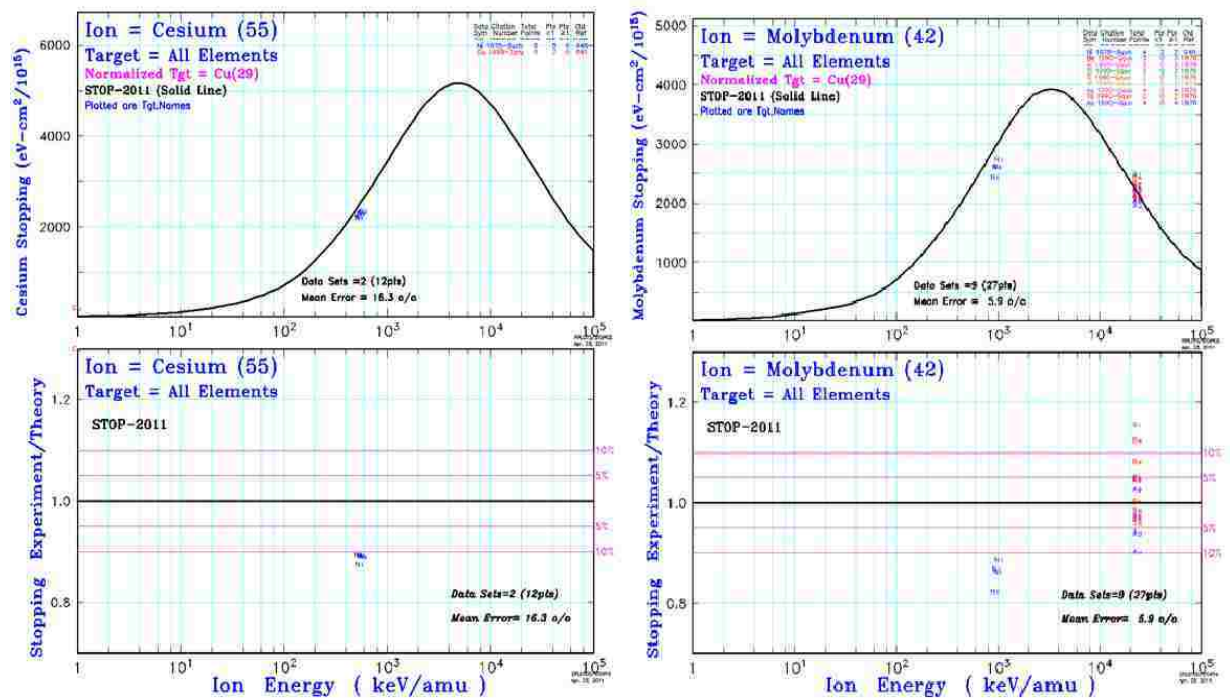
78.

Figure 78: Stopping power accuracy of ^{252}Cf average light and heavy fission fragments.

Alternatively there has been a large amount of experiments conducted with alphas, as
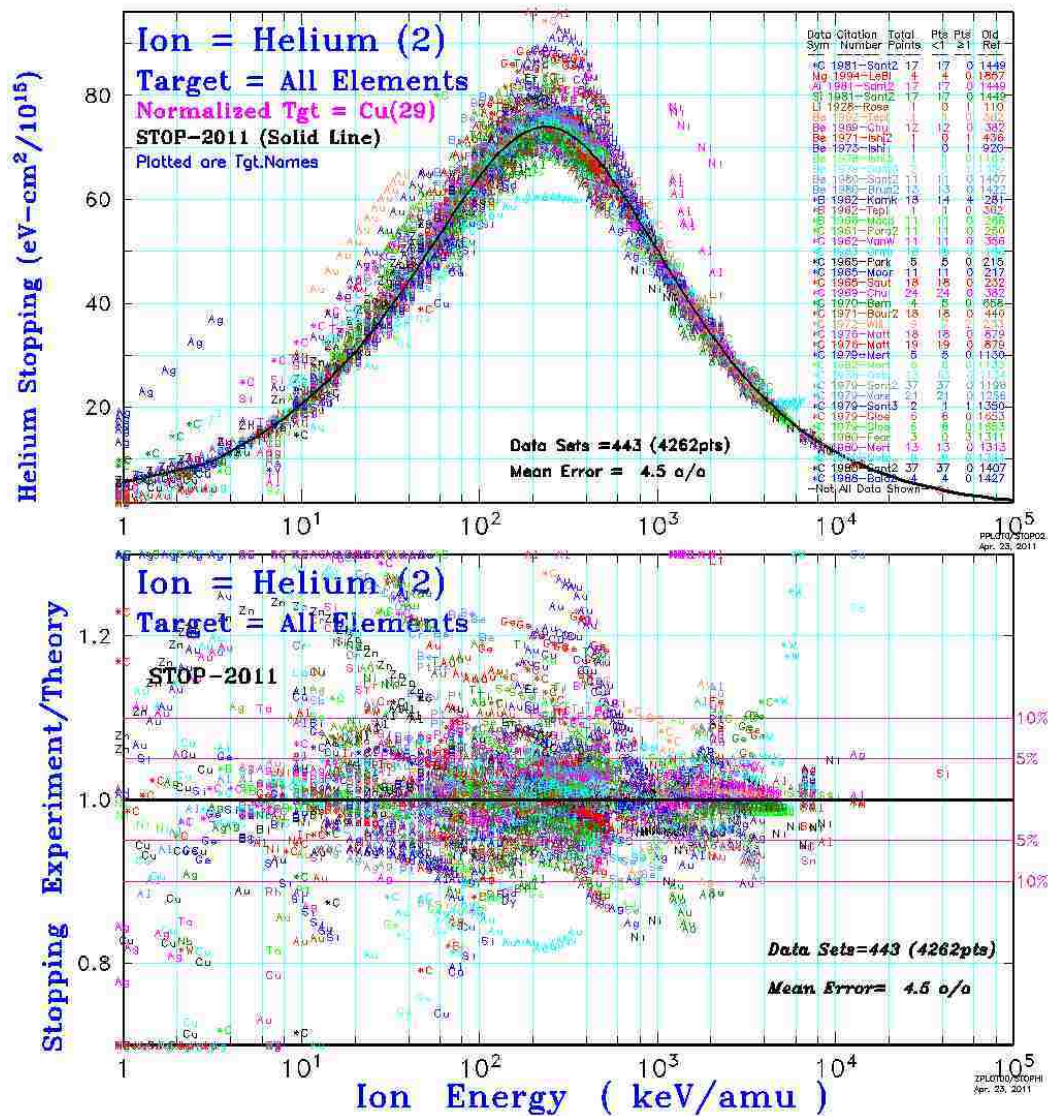
shown in the following Figure 79.

Figure 79: Stopping power accuracy of alpha ions through different targets (Ziegler 1999).

A.2   SolidWorks Drawings
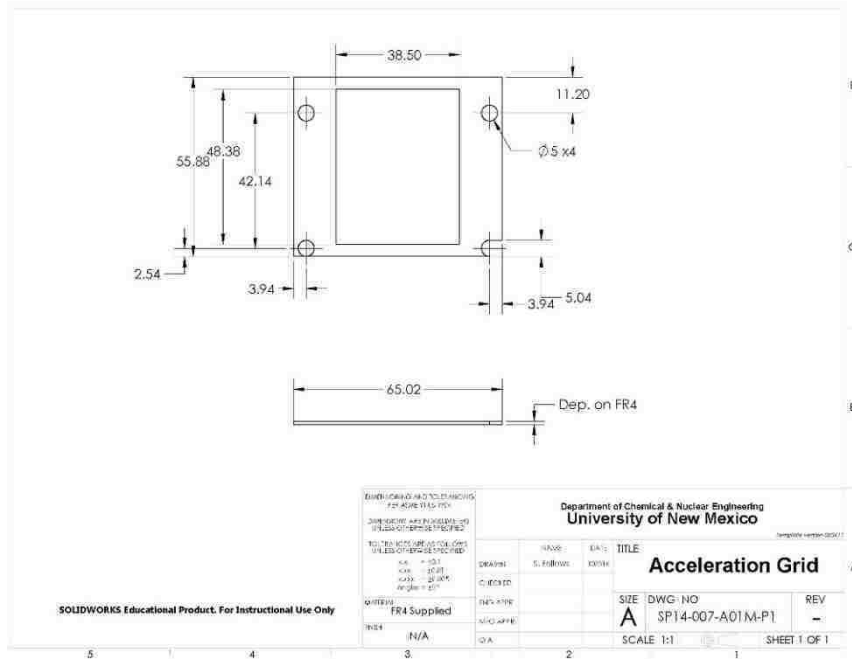

Figure 80: 7 window SiN design.

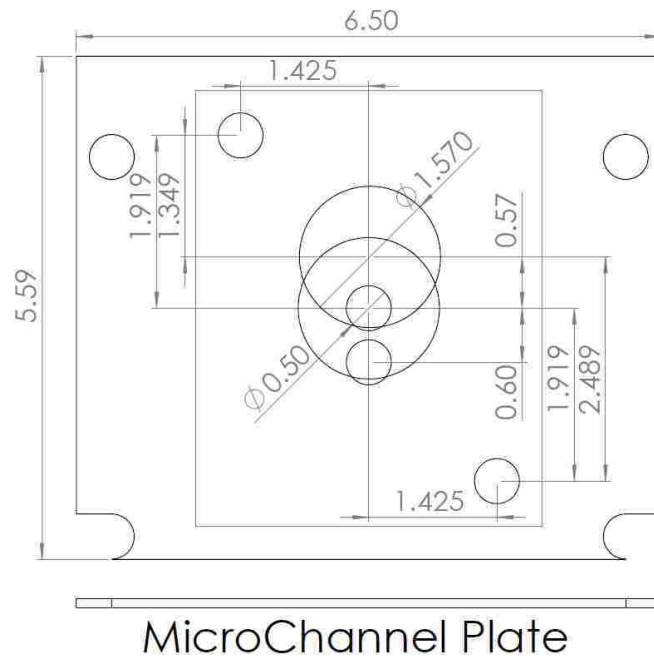**Figure 81: Acceleration grid for timing module.**

Figure 82: Blocker and source position in relation to the center of the blocker.

129